WASHINGTON UNIVERSITY IN ST. LOUIS

Division of Biology and Biomedical Sciences
Neurosciences

Dissertation Examination Committee:
Rajendra Apte, Chair
Aaron DiAntonio
Vladimir Kefalov
Daniel Ory
Rithwick Rajagopal

Understanding the Molecular Pathogenesis of Retinal Neurodegeneration

by
Jonathan Beaux Lin

A dissertation presented to
The Graduate School
of Washington University in
partial fulfillment of the
requirements for the degree
of Doctor of Philosophy

May 2020
St. Louis, Missouri

ProQuest Number: 27836096

ProQuest.

ProQuest 27836096

Table of Contents

List of Figures

List of Tables

Acknowledgments

I am exceedingly grateful for all of the wonderful people who have supported me during my graduate school training. I must first thank my previous mentors, Krish Sathian, Simon Lacey, Saber Hussain, and Amanda Schrand, who were willing to accept me into their labs when I was a young, inexperienced undergraduate student. Without their support and their willingness to write this a million times in letter form, I would not have been able to get to where I am today.

When I first met my thesis advisor, Raj Apte, in the fall of 2011, I did not know at the time that this would be the beginning of a tremendously fulfilling mentor-mentee relationship. Raj: thanks for always being available to answer any and all questions – scientific, professional, or otherwise – even when you are halfway across the world. I could not have found a better graduate school mentor. I would also like to thank the members of my thesis committee and collaborators. Vladimir, Daniel, Aaron, Rithwick, Jay, and Shin: My science is better because of your valuable input, and I cannot thank you enough for your support.

To Apte Lab members, both past and present: thanks for making the Apte Lab the wonderful place that it is. Special thanks to Abdoulaye Sene, Rei Nakamura, and Norimitsu Ban for providing helpful career advice and Andrea Santeford for being the best bay-mate ever.

Mom, Dad, and Joseph: thanks for being the best support system that I could have asked for. I value your strength, guidance, and wisdom more than I could ever express. To my new St. Louis family (Steph, Nia, Alex, Tirth, Dan, Vikram, Owen, Mariah, Kelly, Kathleen, Andrew, Ben): thanks for making the past six years so wonderful. We have shared so many remarkable experiences; the memories we have created will last a lifetime!

ABSTRACT OF THE DISSERTATION

Understanding the Molecular Pathogenesis of Retinal Neurodegeneration

by

Jonathan Beaux Lin

Doctor of Philosophy in Biology and Biomedical Sciences

Neurosciences

Washington University in St. Louis, 2020

Professor Rajendra Apte, Chair

Retinal degenerative diseases are a major cause of morbidity in modern society because visual impairment significantly decreases the quality of life of patients. A significant challenge in treating retinal degenerative diseases is their genetic and phenotypic heterogeneity. Furthermore, limitations in our understanding of disease pathophysiology have led to reliance on therapies that often treat disease endpoints rather than addressing disease etiology and/or pathophysiology. The long-term goal of my thesis research was to provide molecular and cellular insights into the pathophysiology underlying diverse retinal degenerative diseases, which may lead to much-needed, novel therapeutic approaches. During the first part of my thesis research, I discovered that impaired NAD^+ homeostasis is a central feature of diverse retinal degenerative diseases (Chapter 2). For the second part of my thesis research, I found that the central cellular phenotype of aged macrophages, which are known to promote age-related macular degeneration, is impaired cholesterol homeostasis (Chapter 3) and that the transition towards this disease-promoting, aged phenotype is regulated, in part, by microRNA-150 (Chapter 4). Although further research is necessary to translate these findings to the bedside, they have the potential to transform care for patients with retinal degenerative diseases.

Chapter 1:

Introduction

This chapter is adapted, in part, from an invited review article published in *Progress in Retinal and Eye Research*.

Lin JB, Apte RS. (2018). NAD$^+$ and sirtuins in retinal degenerative diseases: A look at future therapies. Prog Retin Eye Res, 67:118-129. doi: 10.1016/j.preteyeres.2018.06.002.

1.1 Introduction

Vision is a central sense that is considered critical in modern society. Numerous studies have demonstrated that visual impairment is associated with significant morbidity and has a huge impact on one's quality of life. For example, visual impairment is associated with clinically significant decreases in mobility and independence (Fenwick et al., 2016). Furthermore, in patients with the blinding disease retinitis pigmentosa (RP), there is a correlation between residual visual field and quality of life (Chaumet-Riffaud et al., 2017), suggesting that there is an association between the degree of vision loss and the extent of impairment in quality of life. These decreases in quality of life can contribute to poor mental health. In support, Heesterbeek and colleagues found that a prospective cohort of 540 older adults with vision impairment exhibited twice the incidence of subthreshold depression and anxiety compared to older adults in general (Heesterbeek et al., 2017). Although these symptoms tended to fluctuate with time, having macular degeneration and problems with adapting to vision loss were two of the risk factors identified for developing depressive symptoms (Heesterbeek et al., 2017). Therefore, vision loss and the associated sequelae have a significant impact on human beings individually and on society in general. As such, despite their challenges, preventing and reversing vision loss caused by diverse retinal diseases are of utmost priority.

Retinal degenerative diseases make up a significant portion of the burden of blindness and are often untreatable. The retina is a complex, light-sensitive, neurovascular tissue with a highly organized structure that is essential to its function **(Figure 1.1)**. Located at the posterior pole of each eye, the retina consists of numerous cell types, all of which must function in a coordinated manner to generate a neural signal to be transmitted to the occipital lobe of the brain via the optic nerve. Light photons entering the anterior surface of the eye first traverse the retina

before being sensed by the photoreceptors on the posterior aspect of the retina. Photoreceptors can be divided into two types: rod photoreceptors mediate dim, peripheral vision, whereas cone photoreceptors mediate central, color vision. The signal from the photoreceptors is then transmitted to secondary neurons known as bipolar cells before being transmitted to the retinal ganglion cells, whose axons coalesce to form the optic nerve. Horizontal and amacrine cells provide lateral modulation. As expected, conditions leading to the death of any of these subpopulations of retinal neurons can lead to visual impairment. In particular, photoreceptor death is a common cause of blindness in retinal degenerative diseases, as these light-sensitive neurons are responsible for the initial transduction of light.

In this chapter, I will first provide a brief clinical description of various examples of retinal degenerative diseases to frame a discussion regarding the limitations of their current treatment options. Chapters 2, 3, and 4 describe three distinct research projects that I have undertaken during my graduate training with the long-term goal of improving our understanding of the pathophysiology underlying retinal degenerative diseases. Although further research is necessary to more fully understand the molecular and cellular pathways involved in these processes and, ultimately, to translate these findings from the bench to the bedside, these therapies have the potential to be highly innovative and may transform the care that clinicians can offer to patients with retinal degenerative diseases.

1.2   Retinal Degenerative Diseases

Retinal degenerative diseases are a heterogeneous family of multiple conditions all involving death or damage to cells of the retina. These diseases have a wide array of etiologies: some are acquired, some are a component of a broader systemic disease, and some are inherited.

3

Although some of these conditions share phenotypic characteristics, most have different underlying pathogeneses. This diversity makes it rather challenging to develop unifying therapeutic strategies. Instead, the prevailing dogma has been to consider each disease as a separate entity with its own avenue of research, discovery, and translational pipeline.

1.3   Age-Related Macular Degeneration

Age-related macular degeneration (AMD) is an acquired retinal degenerative disease that affects the central retina, called the macula. AMD is a leading cause of blindness in adults over the age of 50 years. AMD is projected to become an even larger problem over time and is predicted to affect as many as 288 million people by 2040 (Wong et al., 2014). Clinically, patients with early-stage AMD often complain about reduced light sensitivity, dark adaptation, and contrast sensitivity, which is believed to be related to early parafoveal rod photoreceptor degeneration (Curcio et al., 1996). On examination, these patients often present with the presence of lipid- and protein-rich deposits known as drusen in the sub-retinal space. Drusen themselves do not usually cause vision loss, but they are a significant risk factor for progression to advanced AMD that manifests either as advanced non-neovascular (dry) AMD or neovascular (wet) AMD. Both forms of advanced disease can lead to significant visual impairment related to secondary degeneration and death of macular photoreceptors, causing loss of central vision. In the case of advanced dry AMD, blindness is caused by death of the photoreceptors due to loss of the underlying retinal pigment epithelium (RPE) cells that are critical for photoreceptor survival and function. This stage of disease is called geographic atrophy (GA). In contrast, in wet AMD, pathological angiogenesis manifests as choroidal neovascularization (CNV), which can also cause photoreceptor death, retinal and sub-retinal fibrosis, and, ultimately, blindness. It is often

4

difficult for clinicians to counsel AMD patients regarding when progression to advanced disease may occur and what form it will take. The Age-Related Eye Disease Study (AREDS), sponsored by the National Eye Institute, was a large cohort study that provided key insights into the natural history of AMD. This study also identified risk factors associated with progression from early or intermediate AMD to advanced AMD, such as smoking and greater body mass index (BMI) (Clemons et al., 2005). Nonetheless, further research is necessary to determine the specific molecular and cellular mechanisms that underlie AMD pathogenesis.

Genome-wide association studies have provided some clues into potential pathogenic mechanisms underlying AMD by identifying that polymorphisms in complement factor H, hepatic lipase (LIPC), ATP-binding cassette transporter member 1 (ABCA1), and cholesterol ester transfer protein (CETP), are associated with early or advanced AMD (Hageman et al., 2005; Neale et al., 2010). These findings implicate altered regulation of inflammation and aberrant lipid homeostasis as potential contributors to the pathogenesis of AMD. In support, mouse models designed to mimic perturbations in inflammation or lipid homeostasis pathways in combination with environmental factors, such as a high-fat, Western diet, have been reported to recapitulate some features resembling AMD (Malek et al., 2005; Sene et al., 2013; Toomey et al., 2015). These findings confirm the relevance of these pathways in AMD and highlight the value of using mouse models for furthering our understanding of AMD.

Currently, approved therapies for wet AMD include drugs directed against vascular endothelial growth factor (VEGF). VEGF is a key driver of pathological angiogenesis, the hallmark of wet AMD. Although anti-VEGF therapies have revolutionized treatment for wet AMD, long-term studies have demonstrated that atrophic neurodegeneration with loss of photoreceptors proceeds despite treatment (Bhisitkul et al., 2015; Sene et al., 2015). Perhaps

5

more importantly, some patients do not respond or are under-responsive to this therapy (Inoue et al., 2016; Kim et al., 2016; Sarwar et al., 2016; Sene et al., 2015), suggesting that VEGF-independent pathways may also contribute to AMD pathogenesis. More research is needed to identify alternate therapeutic strategies that may be able to provide clinical benefit for these patients and to prevent photoreceptor neurodegeneration in both forms of advanced AMD. Unfortunately, because the pathophysiology of dry AMD remains incompletely understood, there are currently no approved therapies for dry AMD. High-dose supplementation of vitamins C and E, beta carotene, and zinc has been suggested to modestly slow progression to advanced AMD (Age-Related Eye Disease Study Research, 2001), but the effect size is fairly small, and its mechanism is still unclear. Taken together, it is clear that there is a paucity of current treatment options for AMD patients beyond targeting VEGF in wet AMD.

1.4   Diabetic Retinopathy

Diabetes mellitus is a systemic metabolic disease characterized by deficits in blood glucose control. The pathophysiology of diabetes mellitus is complex and affects numerous organ systems, but one component of this systemic disease is diabetic retinopathy (DR). Clinically, DR consists of early microvascular damage, which is initially characterized by pericyte loss and microaneurysms in small-caliber vessels in the retina, followed by capillary wall damage, leakage, exudation, and retinal edema. In advanced disease, hypoxic pathologic neovascularization can cause vision loss secondary to hemorrhage and detachment of the neurosensory retina. In addition to this vascular phenotype, diabetic patients often exhibit changes detectable with electroretinography (ERG), such as delayed implicit times (Satoh et al., 1994) and decreased oscillatory potential amplitudes (Coupland, 1987), which precede vascular

6

changes. DR could therefore include two components – neuroretinal dysfunction and vascular dysfunction – with both contributing to vision loss.

Studies in mouse models of DR support this possibility. For example, Rajagopal and colleagues identified that mice weaned to high-fat chow exhibit modest electrophysiological dysfunction in the form of increased latencies and decreased oscillatory potential amplitudes at six months that precede the vascular phenotype of microvascular disease that can be observed by 12 months (Rajagopal et al., 2016). These findings may have translational relevance since multifocal ERG implicit times in patients with diabetes but without retinopathy predict future development of DR (Harrison et al., 2011). Other groups have reported even more striking high-fat diet-induced retinal dysfunction in mice at 12 weeks in the form of reduced scotopic and photopic ERG amplitudes (Chang et al., 2015). Mechanistic studies suggest that this neuroretinal dysfunction may be due to the sensitivity of retinal neurons to systemic hyperglycemia. For example, in the streptozotocin-induced mouse model of diabetes, prolonged hyperglycemia leads to retinal oxidative stress (Du et al., 2013), which may contribute to photoreceptor death.

Currently, clinicians can treat only the vascular disease, including permeability-related macular edema and ischemic neovascularization, with anti-VEGF pharmacotherapy and intraocular steroids. Neuroprotective strategies that could mitigate neuroretinal dysfunction or prevent retinal neurodegeneration are highly attractive but are currently investigational. As in AMD, a molecular understanding of the pathophysiology of DR might improve our ability to develop more diverse therapeutic strategies to prevent vision loss in DR.

1.5   Inherited Retinal Degenerations

Inherited retinal degenerations (IRDs) are diverse diseases that are associated with progressive vision loss caused by mutations in over 250 genes. Some examples of IRDs include RP, Leber congenital amaurosis (LCA), and rod-cone or cone-rod dystrophies. IRDs can be isolated or syndromic. For example, RP, one of the most common IRDs, can be caused by mutations in any of more than 100 genes or can be a clinical feature of Usher syndrome or Bardet-Biedl syndrome. Because of this genotypic diversity, RP has a complex and heterogeneous clinical presentation that often depends on the underlying mutation. In general, RP patients present with loss of night vision and decreased peripheral vision due to death of rod photoreceptors. As rod photoreceptor death progresses, cone photoreceptor death may follow as a secondary effect of losing rod photoreceptor-derived survival factors. Exome and targeted gene sequencing have made it possible to examine the genetic etiology of various retinal degenerative diseases, including RP.

Despite remarkable advances in our ability to identify the causative gene mutations associated with IRDs, including RP, our therapeutic strategies are still limited by lack of knowledge of the mechanisms by which these gene mutations cause disease. One therapeutic approach has been gene therapy with the goal of replacing the defective copy or copies of the affected gene with a normal gene delivered by a carrier, usually a viral vector. For example, a Phase III trial recently evaluated the safety and efficacy of voretigene neparvovec (AAV2-hRPE65v2) in patients with retinal dystrophy caused by biallelic mutations in RPE65 (Russell et al., 2017). Using this approach, a wild-type copy of the *RPE65* gene is delivered with an adenoviral vector to the sub-retinal space. In patients with viable retinal cells, normal RPE65 protein can restore the visual cycle and may lead to some vision improvement. Although still in

8

its infancy compared to conventional gene therapy, CRISPR-Cas9 has also now made it possible to perform targeted gene editing to repair disease-causing mutations, which has been shown to be effective in restoring some vision in rodent models of retinal degenerative disease (Bakondi et al., 2016; Wu et al., 2016). However, one major challenge of both gene therapy and gene editing is that they would have to be optimized and targeted for each specific mutation, requiring the causative mutation to be identified in each individual patient. This requirement is a challenging proposition considering the diversity of mutations that have been identified, especially for RP, each affecting a fraction of the total patient population. Perhaps of additional concern, gene therapy is incredibly expensive in the present, making it difficult to use in widespread settings. Issues surrounding the durability of the effect, effect size, and scalability in more prevalent diseases further complicate the therapeutic landscape.

1.6   Limitations of Current Therapeutic Approaches

For many retinal degenerative diseases, our incomplete understanding of disease pathogenesis has led to a current strategy of addressing disease symptoms and endpoints rather than their underlying etiology. For example, in AMD and DR, patients receive anti-VEGF therapies to inhibit pathological angiogenesis. For IRDs, even if we have a sophisticated understanding of the underlying genetics, it is not always easy to deliver therapeutics in a clinical setting due to the challenges highlighted above. Therefore, an attractive option would be to identify a potential therapeutic strategy that could prevent photoreceptor death in multiple forms of retinal degenerative diseases. One example of such an approach is stem cell therapy. Previous mouse studies have shown that photoreceptor neuron transplantation is feasible and improves visual function (MacLaren et al., 2006; Pearson et al., 2012; Santos-Ferreira et al., 2015). These

investigations have been the basis of ongoing human clinical trials using stem-cell based approaches in AMD (Mandai et al., 2017; Schwartz et al., 2015; Schwartz et al., 2016). Although these studies adopt the strategy of RPE transplantation rather than photoreceptor neuron transplantation since RPE dysfunction is known to contribute to photoreceptor degeneration in advanced dry AMD, they demonstrate that transplantation of cells into the eye is feasible, paving the way for future human clinical studies of photoreceptor transplantation.

There remain numerous challenges of using stem cells for photoreceptor transplantation, such as ensuring proper functional connectivity with the host retina, the time required to differentiate cells for transplantation, and potential tumorigenicity of transplanted cells. Recent studies also suggest that material transfer of proteins from transplanted photoreceptors to host cells may itself improve visual function, necessitating a closer look at the mechanism underlying rescue in transplantation studies (Pearson et al., 2016; Waldron et al., 2018).These are important issues that must be investigated thoroughly before stem cell therapy can be widely used in humans. The source of stem cells also poses a significant challenge. Although induced pluripotent stem cells (iPSCs) can be used to overcome the ethical concerns and regulatory challenges surrounding embryonic stem cells since iPSCs are reprogrammed from adult somatic cells, they have one major limitation: specifically, since the source of iPSCs is often the patients themselves, the cells retain disease-causing mutations, requiring gene editing prior to transplantation. Although targeted gene editing can be achieved with CRISPR-Cas9 in mouse models (Burnight et al., 2017), successful application of this technology to treat retinal degenerative diseases in humans is still in its infancy.

1.7   Conclusions

Retinal degenerative diseases are a major cause of morbidity in the modern world. Visual impairment significantly diminishes the quality of life of patients. A significant challenge in preventing blindness caused by retinal diseases is the genetic and phenotypic heterogeneity of the diseases and a variable understanding of disease pathogenesis. This limited understanding has led to either the widespread use of drugs that treat disease manifestations in relatively late phases of the natural history rather than the underlying cause or, in many instances, a complete lack of treatment options altogether. Indeed, more research is necessary to identify novel therapeutics for early and targeted intervention. Some strategies, such as gene therapy and stem cell-based therapeutic approaches, have been proposed, although they have limitations, such as the fact that gene therapy would have to be tailored for the causative mutation of each individual disease. The ability to identify novel therapies for diverse retinal diseases is highly attractive and would address a great clinical need.
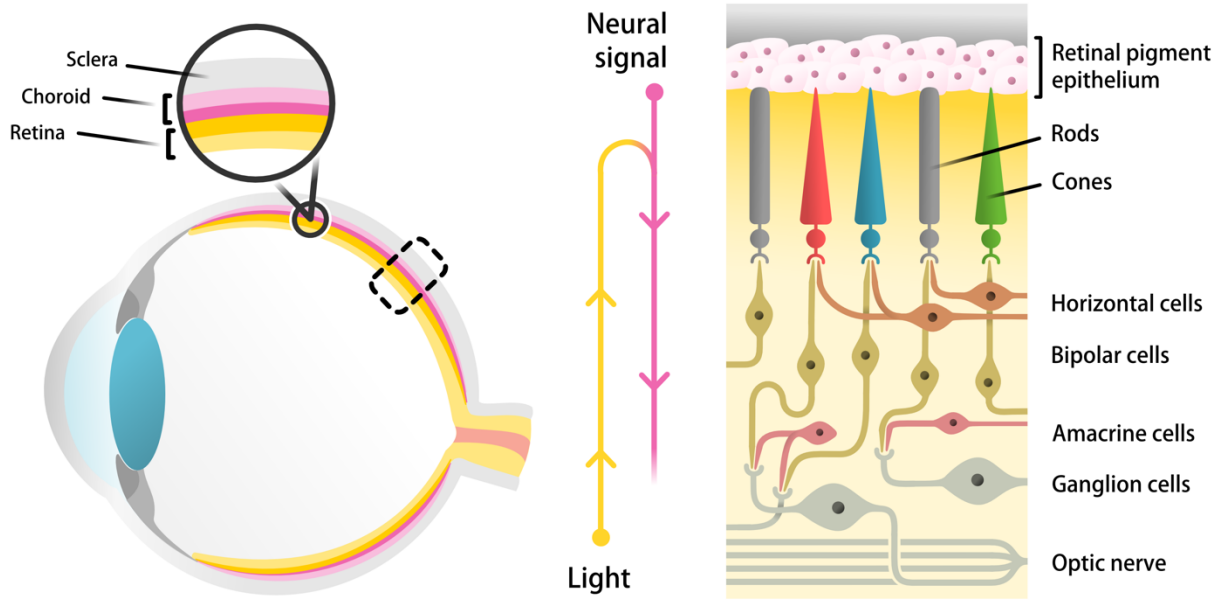
Figure 1.1. Schematic depicting the structural organization of the neurosensory retina and its location in the eye. The retina consists of numerous neuronal cell types, including rod and cone photoreceptors, bipolar cells, retinal ganglion cells, horizontal cells, and amacrine cells.

Chapter 2:

NAMPT-Mediated NAD$^+$ Biosynthesis Is Essential for Vision in Mice

This chapter is adapted from a manuscript published in *Cell Reports*.

J.B.L. & S.K. = co-first authors

2.1   Summary

Photoreceptor death is the endpoint of many blinding diseases. Identifying unifying pathogenic mechanisms in these diseases may offer global approaches for facilitating photoreceptor survival. We found that rod or cone photoreceptor-specific deletion of nicotinamide phosphoribosyltransferase (*Nampt*), the rate-limiting enzyme in the major NAD^+ biosynthetic pathway beginning with nicotinamide, caused retinal degeneration. In both cases, we could rescue vision with nicotinamide mononucleotide (NMN). Significantly, retinal NAD^+ deficiency was an early feature of multiple mouse models of retinal dysfunction, including light-induced degeneration, streptozotocin-induced diabetic retinopathy, and age-associated dysfunction. Mechanistically, NAD^+ deficiency caused metabolic dysfunction and consequent photoreceptor death. We further demonstrate that the NAD^+-dependent mitochondrial deacylases SIRT3 and SIRT5 play important roles in retinal homeostasis and that NAD^+ deficiency causes SIRT3 dysfunction. These findings demonstrate that NAD^+ biosynthesis is essential for vision, provide a foundation for future work to further clarify the mechanisms involved, and identify a unifying therapeutic target for diverse blinding diseases.

2.2   Introduction

Vision is a crucial sense that depends on photoreceptors for light transduction. Photoreceptors are divided into two classes: rods and cones. Rod photoreceptors mediate dim vision, while cone photoreceptors mediate precise central vision in ambient light. Photoreceptors make up a significant portion of the neurosensory retina, one of the most metabolically active tissues in the body (Ames et al., 1992; Kooragayala et al., 2015; Okawa et al., 2008). Although terminally differentiated and non-proliferative, photoreceptors have tremendous metabolic demands throughout their lives and experience significant light-induced oxidative stress due to their function of performing light transduction (Fu and Yau, 2007; Yau and Hardie, 2009).

Because of the critical role that photoreceptors play in light transduction, photoreceptor death leads to blindness. Despite their differing etiologies, many blinding diseases share this final pathway of photoreceptor death, which inevitably causes vision loss. For example, age-related macular degeneration (AMD) is one leading cause of blindness in older adults (Apte, 2010; Klein et al., 2004; van Leeuwen et al., 2003). Although advanced AMD takes on two forms (i.e., dry or wet AMD) (Sene and Apte, 2014), both pathways ultimately lead to photoreceptor death. Similarly, inherited retinal degenerations, including retinitis pigmentosa (RP), rod and cone dystrophies, and Leber congenital amaurosis (LCA), are caused by genetic defects in over 100 different genes that lead to photoreceptor death (Astuti et al., 2015; Hartong et al., 2006; Wright et al., 2010). Developing treatment strategies for this broad spectrum of retinal degenerative diseases is challenging given these diverse pathogenic mechanisms.

Nicotinamide adenine dinucleotide (NAD^+) is both an essential coenzyme, functioning as an electron carrier in glycolysis and the Krebs cycle, and an essential cosubstrate for NAD^+-consuming enzymes, including sirtuins, poly(ADP-ribose) polymerases (PARPs), mono-ADP

15

ribosyltransferases, and cyclic ADP-ribose hydrolase (CD38) (Ying, 2006). Given these numerous functions, NAD^+ has been shown to be important in many biological processes, including metabolism (Garten et al., 2009; Mouchiroud et al., 2013), circadian rhythms (Nakahata et al., 2009; Ramsey et al., 2009), and aging (Imai and Guarente, 2014). Relevant to our studies, NAD^+ has also been shown to be important in neurodegeneration (Alano et al., 2010; Gerdts et al., 2015; Stein et al., 2014; Zhou et al., 2015). However, the role of NAD^+ in retinal degeneration has been relatively unexplored to date.

We hypothesized that NAD^+ biosynthesis plays an important role in photoreceptor function and survival. This hypothesis is supported by past studies demonstrating that LCA, the leading cause of childhood blindness from retinal disease, can be caused by mutations in nicotinamide mononucleotide adenylyltransferase 1 (NMNAT1) (Chiang et al., 2012; Falk et al., 2012; Koenekoop et al., 2012; Perrault et al., 2012), an enzyme involved in NAD^+ biosynthesis. The various mutant forms of NMNAT1 associated with LCA exhibit reduced NAD^+ biosynthetic capacity and/or impaired protein folding (Falk et al., 2012; Koenekoop et al., 2012; Sasaki et al., 2015) with both factors contributing to disease pathogenesis.

NAD^+ can be synthesized in three ways: 1) de novo from tryptophan, 2) salvaged from nicotinamide or nicotinic acid (NAM or NA, respectively), or 3) from nicotinamide riboside (NR). In mammals, the salvage pathway beginning with NAM is the predominant NAD^+ biosynthetic pathway (Imai and Yoshino, 2013; Imai and Guarente, 2014). The first step of this pathway is catalyzed by nicotinamide phosphoribosyltransferase (NAMPT), which combines NAM with 5-phosphoribosyl pyrophosphate (PRPP) to form nicotinamide mononucleotide (NMN). NMN is then adenylated by NMNAT1-3 to synthesize NAD^+.

16

In this study, we focus on the role of NAMPT-mediated NAD$^+$ biosynthesis in photoreceptor survival and vision. Our results suggest that NAD$^+$ biosynthesis may be important not only in LCA but also in a broad spectrum of retinal degenerations and age-associated retinal dysfunction. Thus, it may be possible to use NAD$^+$ intermediates to protect against retinal degeneration. Although these findings provide a strong foundation for future studies, further work is needed to clarify the mechanisms involved. If successful, this therapeutic strategy would be far-reaching since it could be used for diverse retinal degenerations regardless of their etiology.

2.3   Results

Loss of NAMPT-mediated NAD$^+$ biosynthesis impairs photoreceptor survival and vision

Photoreceptors are one of the most metabolically active cells of the body with demanding energy requirements (Ames et al., 1992; Okawa et al., 2008) but limited mitochondrial reserve capacity (Kooragayala et al., 2015). Therefore, we hypothesized that photoreceptors depend on NAMPT-mediated NAD$^+$ biosynthesis to meet their catalytic requirements. To test this hypothesis, we examined the effect of disrupting NAMPT-mediated NAD$^+$ biosynthesis selectively in rod photoreceptors by generating conditional knockout mice lacking *Nampt* (*Nampt*$^{-rod/-rod}$).

As expected, rod-enriched retinal isolates from *Nampt*$^{-rod/-rod}$ mice showed significant reduction in *Nampt* gene expression **(Figure 2.1A)**. This rod photoreceptor-specific deletion of *Nampt* led to a ~26% reduction in retinal NAD$^+$ levels in *Nampt*$^{-rod/-rod}$ mice compared to *Nampt*$^{F/F}$ littermates at 3 weeks **(Figure 2.1B)**. We also measured NAD$^+$ levels in rod-enriched retinal isolates to more specifically characterize the magnitude of NAD$^+$ deficiency in rod

17

photoreceptors. We found that rod-enriched isolates from *Nampt*$^{-rod/-rod}$ mice had a ~43%

reduction in NAD$^+$ levels compared to those from *Nampt*$^{F/F}$ mice **(Figure 2.1C)**, suggesting that

the NAD$^+$ deficiency is predominantly specific to the rod photoreceptors.

On biomicroscopy, we found that *Nampt*$^{-rod/-rod}$ mice had a degenerative phenotype that,

by 6 weeks, was characterized by massive atrophy of the neurosensory retina, vascular

attenuation with pigment mottling, and atrophy of the underlying retinal pigment epithelium

(RPE) cells, which was not observed in *Nampt*$^{F/F}$ littermates **(Figure 2.1D)**. This neurosensory

retinal degeneration was also associated with secondary atrophy and pallor of the optic nerve

(Figure 2.1D). We confirmed this degeneration with histological examination of eyes from

Nampt$^{-rod/-rod}$ mice. Although the histology was relatively normal at 2 weeks (data not shown),

there was progressive loss of the outer nuclear layer with associated retinal degeneration,

significant reduction of retinal thickness, and secondary extension to multiple retinal layers in

Nampt$^{-rod/-rod}$ eyes that was complete by 6 weeks **(Figure 2.1E)**. Of note, the outer nuclear layer

(arrows; **Figure 2.1E**) appeared to be almost completely absent by 6 weeks, indicating

substantial photoreceptor death.

We performed electroretinography (ERG) to confirm the functional deficits associated

with this profound anatomic degeneration. By 6 weeks, *Nampt*$^{-rod/-rod}$ mice demonstrated a

dramatic reduction in the amplitudes of rod-generated scotopic a-waves **(Figure 2.1F)**,

indicating significant impairment of rod function. This impairment in rod photoreceptor function

also led to declines in the amplitudes of the scotopic b-waves **(Figure 2.1G)**. Interestingly,

Nampt$^{-rod/-rod}$ mice also exhibited deficits in cone function, as manifested by a decline in the

amplitudes of the photopic b-waves **(Figure 2.1H)**. Although *Nampt* deletion was specifically in

rods, this cone dysfunction was not surprising; cone photoreceptor degeneration is often

observed as a secondary effect of rod photoreceptor degeneration since rods are required for cone survival (Ait-Ali et al., 2015; Wong and Kwok, 2016). Consistently, by 6 weeks, $Nampt^{\text{-rod/-rod}}$ mice had significantly worse photopic visual acuity compared to age-matched $Nampt^{\text{F/F}}$ controls **(Figure 2.1I)**. As such, our findings replicate the progression of rod degeneration followed by cone degeneration often observed in patients with inherited retinal degenerations such as RP.

We also generated $Nampt^{\text{-rod/wt}}$ mice to determine the effect of partial ablation of NAMPT-mediated NAD^+ biosynthesis. As expected, rod-enriched retinal isolates from $Nampt^{\text{-rod/wt}}$ mice exhibited partial reduction in $Nampt$ expression compared to $Nampt^{\text{F/wt}}$ controls (data not shown), which was roughly half of the reduction in $Nampt^{\text{-rod/-rod}}$ versus $Nampt^{\text{F/F}}$ mice. This monoallelic $Nampt$ deletion did not cause a statistically significant reduction in retinal NAD^+ levels nor did it cause significant retinal degeneration by 6 weeks as measured by ERG (data not shown), suggesting that $Nampt$ is haplosufficient during this short time scale.

To confirm that the effect of $Nampt$ deletion was cell autonomous, we generated mice lacking $Nampt$ specifically from cone photoreceptors ($Nampt^{\text{-cone/-cone}}$). Although cones constitute only ~3% of photoreceptors, they are exclusively responsible for precise color and central vision in humans. As expected, immunohistochemistry revealed reduced intracellular NAMPT staining (red) within cone photoreceptors (green) in retinal sections from $Nampt^{\text{-cone/-cone}}$ mice, while retinal sections from $Nampt^{\text{F/F}}$ mice demonstrated robust cone NAMPT expression **(Figure 2.2A)**.

Biomicroscopic imaging of $Nampt^{\text{-cone/-cone}}$ mice demonstrated changes consistent with cone degeneration, including mottling of the RPE and pallor of the optic nerve **(Figure 2.2B)**. This structural degeneration also manifested in functional deficits by ERG. By 6 weeks, $Nampt^{\text{-cone/-cone}}$ mice exhibited mild declines in their scotopic a- and b-wave amplitudes **(Figures 2.2C**

19

and **2.2D)**. More strikingly, *Nampt*[-cone/-cone] mice exhibited dramatic declines in the amplitudes of their photopic b-waves **(Figure 2.2E)**, indicating predominant cone dysfunction. These structural and functional changes in *Nampt*[-cone/-cone] mice were also associated with a significant decrease in photopic visual acuity **(Figure 2.2F)**. Cumulatively, these findings provide strong support for the essential role of NAMPT-mediated NAD^+ biosynthesis in photoreceptor survival, as cell-specific deletion of this key enzyme led to rapid photoreceptor degeneration and vision loss.

Exogenous NMN prevents photoreceptor degeneration and restores vision

To confirm the importance of NAMPT-mediated biosynthesis in photoreceptor survival, we tested whether exogenous supplementation with NMN could rescue photoreceptor degeneration by bypassing the NAMPT-catalyzed reaction. NAMPT catalyzes the conversion of NAM to NMN and should reduce photoreceptor death by ameliorating the NAD^+ deficiency. We gave *Nampt*[-rod/-rod] mice daily intraperitoneal injections of NMN (150 mg/kg) or vehicle alone beginning at P5 and ending at the time of ERG testing. Strikingly, ERG at 4 weeks in NMN-treated *Nampt*[-rod/-rod] mice revealed significant recovery of scotopic and photopic retinal function compared to vehicle-treated *Nampt*[-rod/-rod] mice **(Figures 2.3A, 2.3B, and 2.3C)**. There was no dramatic effect of NMN on the ERG of *Nampt*[F/F] controls (data not shown). Consistently, retinal sections from NMN-treated *Nampt*[-rod/-rod] mice showed rescue of retinal degeneration compared to vehicle-treated *Nampt*[-rod/-rod] mice, as manifested by relative preservation of the outer nuclear layer **(Figure 2.3D)**.

Correspondingly, daily intraperitoneal NMN injections also significantly improved retinal function by ERG in *Nampt*[-cone/-cone] mice compared to vehicle-treated *Nampt*[-cone/-cone] mice **(Figures 2.3E, 2.3F, and 2.3G)**. These data clearly demonstrate that NAMPT-mediated NAD^+

20

biosynthesis is necessary for the survival and function of both rod and cone photoreceptors, as promoting NAD^+ biosynthesis in the retina with NMN supplementation can compensate for *Nampt* deletion, thereby reducing photoreceptor death and improving vision.

Early NAD^+ deficiency is a feature of multiple mouse models of retinal dysfunction

Next, we sought to determine whether NAD^+ deficiency is an early feature of other mouse models of retinal disease or dysfunction, which would support the possibility that NAD^+ intermediates may have therapeutic potential against a broad spectrum of retinal degenerative diseases. Light-induced degeneration is a well-characterized model that is widely used to study mechanisms of photoreceptor death (Grimm and Reme, 2013) and is known to cause retinal dysfunction, which can be observed by histology and ERG (Schimel et al., 2011). We found that there was a significant reduction in retinal NAD^+ levels as early as 24 hours following light exposure **(Figure 2.3H)**. In addition, we tested whether mice with streptozotocin (STZ)-induced diabetic retinopathy, whose retinal dysfunction has been well characterized (Samuels et al., 2015), exhibit retinal NAD^+ deficiency. At 3 weeks after STZ induction, hyperglycemic mice had a significant reduction in retinal NAD^+ compared to non-hyperglycemic controls **(Figure 2.3I)**. Finally, it is well known that there are defects in retinal structure and function in old mice, such as a decreased number of rod photoreceptors, a decreased level of total opsin in the retina, and diminished rod ERG recordings (Kolesnikov et al., 2010; Lin et al., 2016b). Consistent with these past reports, we found that 18-month-old wild-type mice (C57BL/6J) had worse retinal function on ERG compared to strain-matched 6-month-old mice from the same source (data not shown). As in light-induced degeneration and STZ-induced diabetic retinopathy, this age-associated retinal dysfunction was associated with a significant decline in retinal NAD^+ levels

21

(Figure 2.3J). These findings support the idea that NAD$^+$ deficiency may be a shared feature of retinal dysfunction.

NMN rescues retinal dysfunction in light-induced degeneration

Since we showed that there is NAD$^+$ deficiency associated with the retinal dysfunction that follows light-induced degeneration, we sought to determine whether exogenous NMN supplementation to rescue NAD$^+$ deficiency would rescue retinal dysfunction. We gave wild-type mice (129S1/SvImJ) daily intraperitoneal injections of NMN (300 mg/kg) or vehicle alone beginning 6 days prior to light exposure, on the day of light exposure, and for 3 days following light exposure (total of 10 injections/mouse). Remarkably, NMN-treated wild-type mice were more resilient against light exposure and retained improved retinal function as measured by ERG compared to vehicle-treated mice **(Figures 2.4A, 2.4B, and 2.4C)**. These findings suggest that the NAD$^+$ deficiency associated with retinal disease can indeed be rescued by NAD$^+$ intermediates such as NMN, further supporting the possibility of using NAD$^+$ intermediates to treat retinal degenerative diseases.

Loss of NAMPT-mediated NAD$^+$ biosynthesis leads to metabolic dysfunction

To provide insight into how NAD$^+$ deficiency leads to retinal degeneration, we performed transmission electron microscopy on *Nampt*$^{\text{-rod/-rod}}$ retinas. Although there were no obvious differences in mitochondrial ultrastructure at 3 weeks, we observed profoundly dysmorphic changes in photoreceptor inner segments by 4 weeks along with disruption of the outer segments, which we did not observe in *Nampt*$^{\text{F/F}}$ littermates of the same age (data not shown). Of interest, by 4 weeks, the mitochondria of *Nampt*$^{\text{-rod/-rod}}$ retinas were rounded and

constricted with loss of cristae and a morphology that was distinctly different from that observed in *Nampt*$^{F/F}$ littermates **(Figure 2.4D)**. In addition, at this time point, we observed degenerative vacuoles in the cytoplasm of *Nampt*$^{-rod/-rod}$ retinas, which appeared to contain degenerated organelles including ruptured mitochondria (data not shown). These results suggest that loss of NAMPT-mediated NAD$^+$ biosynthesis in photoreceptors leads to mitochondrial structural irregularities that may lead to or be associated with defects in mitochondrial function.

To characterize these possible mitochondrial defects, we performed non-biased metabolomic analysis with liquid chromatography-mass spectrometry (LC-MS) and gas chromatography-mass spectrometry (GC-MS), comparing retinas isolated from 3-week old *Nampt*$^{-rod/-rod}$ mice to those isolated from gender-matched *Nampt*$^{F/F}$ littermates. We chose this time point since it would allow us to identify signs of mitochondrial dysfunction that precede gross retinal degeneration. The LC-MS results revealed that although there were no statistically significant differences, there was a trend toward accumulation of some acylcarnitine species in *Nampt*$^{-rod/-rod}$ retinas, suggesting a possible defect in Krebs cycle efficiency (data not shown). In addition, the GC-MS results revealed that numerous mitochondrial metabolites were significantly elevated or reduced in *Nampt*$^{-rod/-rod}$ retinas. To determine whether the identities of these dysregulated metabolites were suggestive of defects in certain metabolic pathways, we performed metabolite set enrichment analysis with MetaboAnalyst 3.0 (Xia et al., 2015) using the over representation analysis algorithm. This analysis revealed that there are numerous metabolic pathways that are broadly dysregulated in *Nampt*$^{-rod/-rod}$ retinas, including protein biosynthesis, propanoate metabolism, and the citric acid cycle, among others **(Figure 2.4E)**.

To confirm that these effects on mitochondrial function were indeed related to loss of NAMPT function within photoreceptors, we treated 661W cone photoreceptor-like cells with the

23

pharmacological NAMPT inhibitor FK866 (20 µM) and measured reductive capacity to approximate metabolic activity. NAMPT inhibition caused considerable reduction of photoreceptor cell reductive capacity. By 24 hours, FK866-treated cells had roughly 40% of the reductive capacity of vehicle-treated cells **(Figure 2.5A)**. By 48 hours, there was an even more dramatic effect with reductive capacity reduced down to ~20% **(Figure 2.5B)**. Although there was no cell death at 24 hours **(Figure 2.5C)**, this loss of reductive capacity ultimately led to cell death by 48 hours **(Figure 2.5D)**. This finding highlights that metabolic dysfunction, as represented by a decrease in reductive capacity, precedes cell death.

Since we observed that exogenous NMN supplementation rescued retinal function in $Nampt^{-rod/-rod}$ and $Nampt^{-cone/-cone}$ mice, we tested whether NMN supplementation could rescue the deleterious effects of NAMPT inhibition in photoreceptor cells. Our results demonstrate that providing FK866-treated photoreceptors with NMN (100 µM) could completely restore normal reductive capacities at 24 hours and at 48 hours and prevent subsequent cell death **(Figures 2.5A, 2.5B, and 2.5D)**. These results provide strong evidence for the importance of NAMPT-mediated NAD$^+$ biosynthesis in photoreceptors since we demonstrate that bypassing the NAMPT-catalyzed reaction could restore normal reductive capacity and prevent cell death.

To determine whether these dramatic effects of NAMPT inhibition were unique to photoreceptors, we tested the effects of FK866 (20 µM) on the reductive capacity and cell survival of ARPE-19 RPE cells. Of interest, an identical dose of FK866 had no effect on the reductive capacity of RPE cells at 24 hours and only a modest albeit statistically significant effect on reductive capacity at 48 hours (data not shown). Remarkably, FK866 did not reduce RPE cell survival at either 24 or 48 hours (data not shown), demonstrating that RPE cells are more resilient to metabolic dysfunction and thereby protected from cell death. Ultimately, these

24

results suggest that photoreceptors are uniquely vulnerable to impairment of NAMPT-mediated NAD^+ biosynthesis and implicate this pathway as a master regulator of photoreceptor metabolism and survival.

NAMPT inhibition causes rapid NAD^+ depletion, leading to an ATP crisis

To further characterize the effects of NAMPT inhibition, we measured NAD^+ levels in photoreceptor cells after treatment with FK866 (20 μM). As expected, by 6 hours, FK866-treated photoreceptor cells contained significantly less total NAD^+ compared to vehicle-treated cells plated at the same density **(Figure 2.5E)**. Exogenous NMN supplementation (100 μM) returned NAD^+ back to near-normal levels **(Figure 2.5E)**. After 24 hours, there were undetectable levels of NAD^+ in FK866-treated cells compared to vehicle-treated cells **(Figure 2.5F)**. Similar to the 6-hour time point, exogenous NMN supplementation for 24 hours prevented FK866-associated NAD^+ depletion, bringing NAD^+ back to even higher levels compared to vehicle-treated cells **(Figure 2.5F)**. We interpret these results to indicate that NAMPT inhibition causes rapid NAD^+ deficiency, which likely contributes to the metabolic dysfunction described above.

To further characterize the connection between NAD^+ depletion and cell death, we investigated the time course of NAD^+ depletion and its effect on ATP production by simultaneously measuring NAD^+ and ATP content in photoreceptor cells at various times after treatment with FK866 (20 μM). As above, we found that FK866 caused rapid NAD^+ deficiency. By 6 hours, NAD^+ levels were down to ~50% of their original levels **(Figure 2.5G)**. NAD^+ depletion continued rapidly, dropping to ~15% by 12 hours and to undetectable levels by 24 hours **(Figure 2.5G)**. NAMPT inhibition also caused ATP depletion, but ATP levels did not decline after 6 hours of FK866 treatment and dropped only modestly to ~70% of the original

25

levels by 12 hours **(Figure 2.5G)**. By 24 hours however, ATP levels had dropped down to ~10% of the original levels **(Figure 2.5G)**. The temporal relationship between NAD^+ and ATP depletion suggests that the ATP crisis is a downstream effect of NAD^+ deficiency-associated metabolic dysfunction.

To confirm the connection between NAD^+ availability, ATP content, metabolic function, and cell survival, we also measured NAD^+ and ATP levels in RPE cells after NAMPT inhibition. Consistent with the mild effects on metabolic function and the lack of effect on cell survival, 24 hours of FK866 treatment (20 μM) caused only a ~60% reduction in total NAD^+ levels (data not shown), a smaller effect than that observed after 24 hours of FK866 treatment in photoreceptor cells. This intermediate decrease in total NAD^+ levels was accompanied by a concomitant increase in ATP levels (data not shown), drastically different from the severe ATP depletion exhibited by photoreceptor cells. These findings suggest that photoreceptor cells are more vulnerable to perturbations in NAD^+ biosynthesis compared to other non-photoreceptor eye cells, such as RPE cells.

NAMPT inhibition impairs basal metabolism and the normal response to metabolic stress

The rapid decline of ATP in photoreceptor cells within 24 hours of FK866 treatment suggests that NAMPT inhibition causes significant metabolic dysfunction. To characterize what elements of metabolic function were impaired, we treated photoreceptor cells with FK866 (20 μM) and profiled various aspects of metabolism by measuring oxygen consumption rate (OCR) as a measure of aerobic respiration and extracellular acidification rate (ECAR) as a measure of glycolytic flux. We measured these parameters of metabolic function at baseline and under

various conditions of stress induced by sequential treatments with oligomycin, carbonyl cyanide-4-(trifluoromethoxy)phenylhydrazone (FCCP), and antimycin A/rotenone.

At baseline, FK866-treated photoreceptor cells exhibited reduced OCR and ECAR **(Figures 2.5H and 2.5I)**, indicating that NAMPT inhibition caused reduced basal oxidative respiration and basal glycolytic flux. While vehicle-treated cells responded appropriately to the ATP synthase inhibitor oligomycin by shifting toward glycolytic metabolism (reduced OCR; increased ECAR), FK866-treated photoreceptor cells were unable to shift toward glycolytic metabolism **(Figures 2.5H and 2.5I)**. Moreover, while vehicle-treated cells responded appropriately to the ionophore FCCP by elevating their oxidative respiration (increased OCR), FK866-treated photoreceptor cells were unable to accelerate oxidative respiration in response to metabolic stress **(Figure 2.5H)**. NMN supplementation restored normal baseline metabolism and the appropriate responses to stress **(Figures 2.5H and 2.5I)**, confirming that these phenotypes were specific to NAD^+ deficiency.

To confirm that these effects on metabolic function were specific to NAMPT inhibition, we performed *Nampt* knockdown in photoreceptor cells. Partial reduction of NAMPT-mediated NAD^+ biosynthesis through *Nampt* knockdown in photoreceptor cells caused a reduction in NAD^+ levels (data not shown) within 24 hours after knockdown. Although this intermediate reduction in NAD^+ did not affect reductive capacity or cell survival at the early 48-hour time point, it did impair the ability of photoreceptor cells to maximally accelerate oxidative respiration in response to FCCP (data not shown), further reinforcing the importance of NAMPT-mediated NAD^+ biosynthesis for maintaining mitochondrial homeostasis in photoreceptors.

27

Taken together, these data confirm the importance of NAMPT-mediated NAD$^+$ biosynthesis for maintaining photoreceptor glycolytic and mitochondrial function – both at baseline and in response to metabolic stress – and highlight a NAMPT-specific effect due to the ability of NMN to restore normal metabolic responses. Importantly, we observed these signs of metabolic dysfunction after 24 hours of FK866 treatment prior to when we observed the effects on photoreceptor cell viability. Once again, these results highlight that glycolytic and mitochondrial dysfunction precede and therefore likely cause photoreceptor cell death.

NAD$^+$ deficiency causes NAD-IDH dysfunction

Our in vitro and in vivo results suggest that there are defects in oxidative metabolism in photoreceptors under conditions of NAD$^+$ deficiency. To more specifically characterize these defects in oxidative metabolism, we tested the activity of three enzymes of the Krebs cycle that require NAD$^+$ as a coenzyme: NAD$^+$-dependent isocitrate dehydrogenase (NAD-IDH/IDH3), alpha-ketoglutarate dehydrogenase (AGDH), and malate dehydrogenase (MDH). The fact that these enzymes require NAD$^+$ as a coenzyme provides the opportunity to determine whether their enzymatic dysfunction is caused solely by loss of NAD$^+$ as a coenzyme. If loss of NAD$^+$ as a coenzyme were solely responsible for enzymatic dysfunction, we would expect to be able to restore enzymatic function simply by providing sufficient NAD$^+$ to the reaction mixture.

We found that NAD-IDH activity was significantly lower in rods isolated from $Nampt^{rod/-rod}$ retinas compared to those isolated from $Nampt^{F/F}$ retinas, even when sufficient NAD$^+$ was supplied in the reaction **(Figure 2.5J)** despite similar NAD-IDH expression levels **(Figure 2.5K)**. These findings suggest that NAD-IDH dysfunction cannot be explained by loss of NAD$^+$ as a coenzyme alone. Of significant interest, the rod AGDH and MDH activities were completely

28

rescued by NAD$^+$ **(Figures 2.5L and 2.5M)**, indicating selective enzymatic dysfunction. These findings not only characterize one specific aspect of mitochondrial dysfunction but also suggest that NAD$^+$ plays important roles on regulating metabolism in addition to its role as a coenzyme.

SIRT3 and SIRT5 play important roles in photoreceptor survival

In addition to serving as a coenzyme for crucial steps of glycolysis and the Krebs cycle, NAD$^+$ also serves as a cosubstrate for NAD$^+$-consuming enzymes, including the sirtuins. Of the seven sirtuin family members, three of them, SIRT3, SIRT4, and SIRT5, are known to regulate mitochondrial function (Laurent et al., 2013; Yang et al., 2007; Zhang et al., 2015). Because other sirtuin family members have been shown to play crucial roles in regulating the survival of retinal cells (Jaliffa et al., 2009; Silberman et al., 2014) and because sirtuins depend on NAD$^+$ availability for optimal function (Satoh and Imai, 2014), we hypothesized that NAD$^+$ deficiency may also impair mitochondrial sirtuin activity, contributing to mitochondrial dysfunction.

To determine whether the mitochondrial sirtuins are essential for photoreceptor survival, we performed individual and combined knockdown of SIRT3, SIRT4, and SIRT5 in photoreceptor cells. Individual knockdown of SIRT3 and SIRT5 caused significant reduction in reductive capacity compared to knockdown by negative control **(Figure 2.6A)**. Interestingly, individual knockdown of SIRT4 did not diminish reductive capacity, highlighting the specificity of the effect of SIRT3 and SIRT5 **(Figure 2.6A)**. Combined SIRT3 and SIRT5 knockdown had a synergistic effect, leading to significantly lower reductive capacity compared to either single knockdown alone **(Figure 2.6A)**. Of note, NMN was not able to rescue the effect on reductive capacity in the SIRT3/SIRT5 double knockdown **(Figure 2.6A)**, suggesting that exogenous NMN cannot protect against SIRT3/SIRT5 deletion.

29

This decline in reductive capacity secondary to SIRT3/SIRT5 knockdown was also accompanied by progressive cell death. Individual knockdown of SIRT3 and SIRT5 caused significant reduction in cell survival compared to knockdown by negative control **(Figure 2.6B)**. Again, individual knockdown of SIRT4 had no effect on cell viability **(Figure 2.6B)**, highlighting the specificity of the SIRT3/SIRT5 effect. Once again, combined SIRT3 and SIRT5 knockdown had a more profound effect on cell death compared to either individual knockdown alone **(Figure 2.6B)**. Consistently, NMN supplementation did not rescue the cell death caused by combined SIRT3/SIRT5 double knockdown **(Figure 2.6B)**.

To test whether loss of SIRT3 and SIRT5 causes mitochondrial dysfunction similar to that caused by NAD^+ deficiency, we performed individual and combined SIRT3 and SIRT5 knockdowns in photoreceptors and measured the NAD-IDH activity 24 hours after transfection. We found that knocking down SIRT3, SIRT5, or both SIRT3/SIRT5 in photoreceptor cells recapitulated NAD-IDH dysfunction **(Figure 2.6C)**. The fact that SIRT3 and SIRT5 knockdowns phenocopy the NAD-IDH dysfunction observed in rods isolated from *Nampt*[-rod/-rod] retinas suggests that SIRT3 and SIRT5 may play a role in governing the metabolic dysfunction associated with NAD^+ deficiency.

To test the role of SIRT3 and SIRT5 in retinal function in vivo, we tested mice lacking SIRT3 and SIRT5. Both SIRT3[KO] and SIRT5[KO] mice have normal-appearing fundi on biomicroscopy and normal retinal function on ERG compared to strain-matched controls (data not shown). However, since many studies report that SIRT3 and SIRT5 regulate many of the same protein targets and even the same lysine residues within the same protein (Hebert et al., 2013; Park et al., 2013; Rardin et al., 2013a; Rardin et al., 2013b; Schwer et al., 2009; Sol et al.,

30

2012; Still et al., 2013), it is possible that SIRT3 and SIRT5 can compensate for one another. To test this possibility, we also tested mice lacking multiple mitochondrial sirtuins.

Although SIRT3^{KO}SIRT5^{KO} mice had normal retinal function at baseline (data not shown), we could not yet conclude that SIRT3 and SIRT5 are inessential for retinal function since previous studies have reported that mice lacking mitochondrial sirtuins rarely show striking phenotypes (Lombard et al., 2007; Yu et al., 2013) until they are challenged by specific stimuli such as fasting or a high-fat diet (Hirschey et al., 2011). To this end, we tested whether SIRT3^{KO}SIRT5^{KO} mice are more vulnerable to retinal degeneration after exposure to light. We found that SIRT3^{KO}SIRT5^{KO} mice were strikingly more vulnerable to retinal degeneration upon light stress compared to SIRT3^{het}SIRT5^{het} controls as manifested by retinal dysfunction measured by ERG **(Figures 2.6D, 2.6E, and 2.6F)** four days after light treatment. Interestingly, SIRT3^{het}SIRT5^{KO} and SIRT3^{KO}SIRT5^{het} mice demonstrated an intermediate degenerative phenotype **(Figures 2.6D, 2.6E, and 2.6F)**, supporting the notion that SIRT3 and SIRT5 synergistically regulate mitochondrial function in photoreceptors. Together, these results provide strong evidence that SIRT3 and SIRT5 not only are important for maintaining photoreceptor survival but also have distinct, non-redundant roles in regulating retinal homeostasis.

NAMPT inhibition causes SIRT3 dysfunction

Since we found that SIRT3 and SIRT5 are essential for photoreceptor survival, we sought to determine whether NAD$^+$ deficiency caused by NAMPT inhibition impairs SIRT3 and SIRT5 function in photoreceptor cells. Since SIRT3 regulates predominantly protein acetylation (Parihar et al., 2015) and SIRT5 regulates predominantly protein succinylation, malonylation, and glutarylation (Du et al., 2011; Nishida et al., 2015; Papanicolaou et al., 2014; Tan et al.,

2014), we tested whether NAMPT inhibition modulates the acylation of mitochondrial proteins in photoreceptor cells. We found that mitochondrial lysates generated from photoreceptor cells treated with FK866 (20 μM) for 24 hours showed obvious hyperacetylation **(Figures 2.7A and 2.7B)**, indicating SIRT3 dysfunction. Normal acetylation patterns were restored with NMN **(Figures 2.7A and 2.7B)**, confirming that this hyperacetylation was specific to NAMPT inhibition. Although there were clear acetylation changes, these mitochondrial lysates demonstrated only modest changes in succinylation **(Figures 2.7C and 2.7D)** and no obvious differences in malonylation or glutarylation (data not shown), suggesting that NAD$^+$ deficiency primarily impairs SIRT3 function.

To confirm that these effects were caused by NAMPT inhibition rather than being secondary to metabolic dysfunction, we measured the activity of SIRT3 and SIRT5 in the mitochondrial lysates generated from FK866-treated photoreceptor cells. Consistent with our Western Blots, mitochondrial lysates generated from FK866-treated photoreceptor cells had a significant reduction in SIRT3 activity compared to mitochondrial lysates generated from vehicle-treated cells **(Figure 2.7E)**. There was, however, no difference in SIRT5 activity **(Figure 2.7F)**. Taken together, these results demonstrate that NAD$^+$ deficiency leads to dysregulation of the mitochondrial acylome primarily through impairment of SIRT3 function. Since we show that SIRT3 is important for photoreceptor survival, this NAD$^+$ deficiency-associated impairment of SIRT3 activity likely contributes to the mitochondrial dysfunction observed in photoreceptors lacking *Nampt,* providing additional mechanistic evidence for why NAMPT-mediated NAD$^+$ biosynthesis is essential for mitochondrial homeostasis, photoreceptor survival, and vision.

32

2.4 Discussion

NAD$^+$ has numerous functions in diverse biological processes including metabolism, circadian rhythms, aging, and neurodegeneration (Alano et al., 2010; Garten et al., 2009; Gerdts et al., 2015; Imai and Yoshino, 2013; Mouchiroud et al., 2013; Nakahata et al., 2009; Ramsey et al., 2009; Stein et al., 2014; Zhou et al., 2015). In the current study, we demonstrate that NAMPT-mediated NAD$^+$ biosynthesis is indispensable for photoreceptor survival and vision. Using loss-of-function approaches, we show that disrupting NAMPT-mediated NAD$^+$ biosynthesis in rod and cone photoreceptors leads to photoreceptor death, retinal degeneration, and blindness. By testing the effects of NAMPT inhibition on non-photoreceptor cells, we confirm that photoreceptors are uniquely susceptible to perturbations in NAD$^+$ biosynthesis.

Moreover, we demonstrate that, in photoreceptors, loss of NAMPT-mediated NAD$^+$ biosynthesis leads to NAD$^+$ deficiency, significant glycolytic and mitochondrial dysfunction under basal conditions, and the inability to respond appropriately to metabolic stress, which ultimately lead to photoreceptor death and retinal degeneration. Corresponding with this energetic failure, metabolic profiling of retinas from *Nampt*$^{-rod/-rod}$ mice revealed dysregulation of numerous metabolic pathways. Of interest, there was a trend ($P = 0.0704$) toward dysregulation of the citric acid cycle, a key pathway in oxidative metabolism. The trends toward accumulation of various acylcarnitine species also support a failure of Krebs cycle efficiency. These hallmarks of metabolic dysfunction could be identified prior to cell death and vision loss, supporting the possibility of probing mitochondrial function to predict subsequent photoreceptor death (Perron et al., 2013). These findings are interesting, especially considering recent studies that show that photoreceptors have limited mitochondrial reserve capacity, which may make them susceptible to defects in energy homeostasis (Kooragayala et al., 2015). We speculate that defects in the

33

Krebs cycle cause broad energetic failure and contribute to downstream defects in numerous metabolic pathways, such as protein biosynthesis and propanoate metabolism. Further studies are necessary to explore the precise connection between these phenomena.

Our results also identify that NAD^+ deficiency leads to selective enzymatic dysfunction and that cell death is unlikely to be caused by loss of NAD^+ as a coenzyme alone. When we tested the activity of the three NAD^+-dependent enzymes of the Krebs cycle in rods isolated from $Nampt^{-rod/-rod}$ retinas, only NAD-IDH activity could not be rescued by providing sufficient NAD^+ as a coenzyme, while the activity of AGDH and MDH were restored by providing exogenous NAD^+. This result stresses the importance of NAD-IDH in maintaining metabolic homeostasis in photoreceptors. In support, the retina has been shown to be highly dependent on NAD-IDH and exquisitely sensitive to defects in NAD-IDH function, such that mutations in NAD-IDH that impair its catalytic activity cause RP (Hartong et al., 2008). Of significant interest, these RP patients have normal $NADP^+$-dependent IDH (i.e., NADP-IDH or IDH1/IDH2) activity and no other manifestations of disease despite the fact that they carry this mutation in all cells of their body (Hartong et al., 2008). This finding suggests that in contrast with most organ systems, the retina uniquely relies on the NAD^+-dependent form of IDH (Hartong et al., 2008).

We further demonstrate that SIRT3 and SIRT5 both play important roles in photoreceptor survival and that NAD^+ deficiency leads predominately to SIRT3 dysfunction. Our results agree with past studies reporting that other sirtuin family members, including SIRT1 (Jaliffa et al., 2009) and SIRT6 (Silberman et al., 2014), play roles in survival of photoreceptors and other retinal cells. Interestingly, we demonstrate that the deleterious effects of SIRT3 and SIRT5 deletion are synergistic. These findings strongly suggest that SIRT3 and SIRT5 are not redundant even though they may regulate the acylation status of the same mitochondrial proteins and even

34

the same lysine residues within the same proteins (Hebert et al., 2013; Park et al., 2013; Rardin et al., 2013a; Rardin et al., 2013b; Schwer et al., 2009; Sol et al., 2012; Still et al., 2013).

Based on our results, we hypothesize that SIRT3 dysfunction caused by NAD^+ deficiency may contribute to mitochondrial dysfunction by causing aberrant hyperacetylation of key mitochondrial proteins, such as NAD-IDH. The possibility that SIRT3 dysfunction is linked to decreased NAD-IDH activity is supported not only by our ability to recapitulate NAD-IDH dysfunction with SIRT3 knockdown but also by the fact that NAD-IDH has been identified as a target of SIRT3 (Hebert et al., 2013; Rardin et al., 2013b; Schwer et al., 2009; Sol et al., 2012; Still et al., 2013). Further studies are needed to explore this possibility and to confirm these observations in vivo, perhaps using new technologies such as CRISPR/Cas9 to delete *Nampt* selectively from photoreceptors.

Cumulatively, these findings provide unique insights that point to the dominant mammalian NAD^+ biosynthesis pathway as a master regulator of photoreceptor metabolism. Human retinal degenerations encompass a broad spectrum of diseases that include seemingly unrelated disorders such as LCA and RP, which have been associated with mutations in enzymes involved in NAD^+ biosynthesis (Chiang et al., 2012; Falk et al., 2012; Koenekoop et al., 2012; Perrault et al., 2012) and the Krebs cycle (Hartong et al., 2008). Despite these genetic insights, the mechanisms underlying these conditions and what ultimately causes photoreceptor degeneration in these genotypically diverse disorders are poorly understood. We propose a model linking NAD^+ biosynthesis, SIRT3/SIRT5, and metabolism in photoreceptors, which may connect these diverse retinal neurodegenerations at the molecular level.

Remarkably, our studies also demonstrate that bypassing the NAMPT-catalyzed reaction with exogenous NMN supplementation can restore normal NAD^+ levels in photoreceptor cells

despite NAMPT inhibition and reduce photoreceptor death in *Nampt*^{-rod/-rod} mice. In photoreceptor cells subjected to NAMPT inhibition, NMN supplementation prevented metabolic dysfunction and cell death by restoring normal basal glycolytic and mitochondrial function and the ability to respond appropriately to metabolic stress. This therapeutic effect is likely explained by the importance of NAD^+ not only to perform its coenzyme role in various steps of the Krebs cycle and glycolysis but also to maintain optimal SIRT3 activity. We show that multiple mouse models of retinal dysfunction, including light-induced degeneration, STZ-induced diabetic retinopathy, and age-associated retinal dysfunction all exhibit early retinal NAD^+ deficiency. Moreover, the retinal dysfunction associated with light-induced degeneration can be partially rescued with NMN. These findings offer powerful therapeutic avenues for degenerative diseases of the eye and are supported by past studies exploring the therapeutic applications of NAD^+ supplementation in light-induced degeneration (Bai and Sheline, 2013), noise-induced hearing loss (Brown et al., 2014), and high-fat diet- and age-induced metabolic complications (Canto et al., 2012; Ramsey et al., 2008; Stein and Imai, 2014; Yoshino et al., 2011).

Once successfully implemented, this treatment strategy would be far-reaching since it could be implemented for multiple diseases with diverse pathogenic mechanisms, including not only inherited forms of retinal degenerations but also other blinding diseases characterized by a final pathway of photoreceptor death such as age-related macular degeneration and diabetic retinopathy. Given the global importance of NAD^+ biosynthesis and mitochondrial dysfunction in neurons, our findings may also be broadly relevant to other systemic neurodegenerative diseases such as Alzheimer's disease where NAD^+ intermediate supplementation may be neuroprotective.

2.5   Methods

Mice. All animal experiments were approved by the Animal Studies Committee and performed in accordance with the Washington University School of Medicine Animal Care and Use guidelines. *Nampt*^{flox/flox} (*Nampt*^{F/F}) mice were previously characterized (Rongvaux et al., 2008) and were provided by Dr. Shin-ichiro Imai. To generate mice lacking *Nampt* specifically from rod photoreceptors, we crossed *Nampt*^{F/F} mice with mice carrying one copy of the Rhodopsin-iCre75 transgene, which were provided by Dr. Ching-Kang Jason Chen and have been previously characterized (Li et al., 2005). To generate mice lacking *Nampt* specifically from cone photoreceptors, we crossed *Nampt*^{F/F} mice with mice carrying one copy of the human red/green pigment-Cre (HRGP-Cre) transgene, which were provided by Dr. Yun Le and have been previously characterized (Le et al., 2004). We received 6-month-old and 18-month-old wild-type C57BL/6J mice from the National Institutes on Aging (Bethesda MD) and purchased streptozotocin (STZ)-induced hyperglycemic mice (C57BL/6J) from Jackson Laboratories (Bar Harbor ME). We also purchased SIRT3^{-/-}, SIRT5^{-/-}, and the appropriate strain-matched wild-type mice (129S1/SvImJ for SIRT3^{-/-} and B6129SF2/J for SIRT5^{-/-}) from Jackson Laboratories.

Cells and reagents. We routinely cultured 661W cone photoreceptor-like cells, provided by Dr. Muayyad Al Ubaidi (Tan et al., 2004), in Dulbecco's Modified Eagle Medium with 1 g/L glucose and 110 mg/L sodium pyruvate (DMEM; Thermo Fisher, Carlsbad CA) supplemented with 10% Fetal Bovine Serum (FBS; Sigma, St. Louis MO) and 1% penicillin-streptomycin (Thermo Fisher, Carlsbad CA). We prepared stock solutions of FK866 (Santa Cruz Biotechnology, Dallas TX) at 200 mM in DMSO. We purchased nicotinamide mononucleotide

(NMN) from Sigma (St. Louis MO) and dissolved it directly in cell culture media, prepared as described above.

Real-time PCR in rod-enriched samples. We generated rod-enriched samples by vortexing dissected whole retinas for 60 seconds at medium speed and centrifuging the resulting supernatant at 12,800 g for 10 minutes. We extracted total RNA from the resulting pellet with the RNeasy Mini Kit (Qiagen, Valencia CA), prepared cDNA with the High Capacity cDNA Reverse Transcription Kit (Life Technologies, Grand Island NY), and performed PCR amplification of cDNA using Taqman probe-based gene expression assays (Life Technologies, Grand Island NY) as described previously (Kelly et al., 2007). We used probes for *Nampt* (Mm01293560_m1) and *Idh3a* (Mm00499674_m1) normalized to *ActB* (Mm00607939_s1) or *Rho* (Mm01184405_m1) with the ΔΔCT method.

Retinal imaging. We performed digital color fundus photography using the Micron III™ animal fundus camera (Phoenix Research Laboratories, Pleasanton CA). Prior to fundus imaging, we anesthetized mice with an intraperitoneal injection of 86.9 mg/kg ketamine and 13.4 mg/kg xylazine and administered 1.0% tropicamide eye drops (Bausch & Lomb, Tampa FL) to dilate the pupils.

Histology and immunohistochemistry. After euthanizing the mice, we enucleated the eyes and fixed them overnight in 10% formalin. Next, we embedded the eyes in methacrylate and prepared eight to ten sections of 6-8 μm thickness cut at different planes for each eye. We stained slides with hematoxylin and eosin, rabbit anti-NAMPT(161-173) (B5812-200UL; Sigma,

38

St. Louis MO), and rabbit anti-cone arrestin (AB15282; Millipore, Billerica MA). We acquired images with an Olympus FV1000[TM] upright confocal microscope with UV-sensitive (405), multi-Argon (458, 488 & 513) & Helium-Neon (543 & 633) lasers, and a Plan Apo N 60x oil objective (N.A.=1.42).

Electroretinography. We performed electroretinography (ERG) as previously described (Hennig et al., 2013) by using the UTAS-E3000 Visual Electrodiagnostic System running EM for Windows (LKC Technologies, Gaithersburg MD). We extracted quantitative measurements from the ERG waveforms using an existing Microsoft Excel macro that defines the a-wave amplitude as the difference between the average pre-trial baseline and the most negative point of the average trace and defines the b-wave amplitude as the difference between this most negative point to the highest positive point, without subtracting oscillatory potentials.

Photopic visual acuity. We measured mouse photopic visual acuity under standard photopic conditions (1.85 log cd m^{-2}) by testing the optokinetic reflex with the OptoMotry[TM] System (CerebralMechanics) as described previously (Kolesnikov et al., 2011; Umino et al., 2008).

Transmission electron microscopy. To perform transmission electron microscopy, we dissected enucleated eyes to remove the cornea and lens, and fixed eye cups for 4 hours at room temperature in 2% paraformaldehyde/2.5% glutaraldehyde (Polysciences, Warrington PA) diluted in 100 mM sodium cacodylate (pH 7.2). We then washed the fixed eye cups in cacodylate buffer and post-fixed them in 1% osmium tetroxide (Polysciences) for 1 hour. We then rinsed the postfixed eye cups extensively in deionized H$_2$O prior to en-bloc staining with 1% aqueous

39

uranyl acetate (Ted Pella, Redding CA) for 1 hour. Following several rinses, we dehydrated the stained eye cups with a graded series of ethanol solutions and embedded them in Eponate 12 resin (Ted Pella). We cut 95 nm sections with a Leica Ultracut UCT ultramicrotome (Leica Microsystems, Bannockburn IL), stained the sections with uranyl acetate and lead citrate, and imaged them on a JEOL 1200 EX transmission electron microscope (JEOL USA, Peabody MA) equipped with an AMT 8 megapixel digital camera (Advanced Microscopy Techniques, Woburn MA).

Metabolomic analysis. We isolated retinas at the same time of day after restricting oral nutrient intake for 4 hours. We pooled 6 retinas per group and snap-froze them in liquid nitrogen. We then added ammonium bicarbonate-buffered solution to the tissue pellets and transferred these tissue suspensions to tubes for subsequent metabolite extraction. We extracted intracellular metabolites and culture media samples into cold methanol:acetonitrile (ACN):water (H_2O), dried them, derivatized them to their tert-butyldimethylsilyl esters (tBDMS), and then analyzed them on an Agilent 7200 GC-quadrupole-time of flight (QTOF)-MS operating in electron impact ionization mode. We dried an aliquot of each extract and dissolved it in ACN:H_2O for subsequent LC-QTOF-MS analysis. We performed metabolite set enrichment analysis with MetaboAnalyst 3.0 (Xia et al., 2015) by inputting the list of dysregulated metabolites with a statistically significant difference (corrected P-value < 0.05) and a fold change > 1.10. These data were processed with the over representation algorithm and the metabolic pathway-associated metabolite set library.

40

Reductive capacity assay. To quantify reductive capacity, we used the Cell Proliferation Reagent WST-1 (Roche Applied Science, Indianapolis IN) according to manufacturer's instructions. In short, we washed cells once with PBS after the desired treatment and replaced the media with fresh media containing the WST-1 assay solution at a 1:10 dilution. After 2 hours of incubation at 37°C, we measured absorbance at 450 nm with the SpectraMax 190 Absorbance Microplate Reader (Molecular Devices, Sunnyvale CA).

Cell survival assay. To determine cell survival, we used the cell-permeant dye calcein AM (Thermo Fisher, Carlsbad CA) according to manufacturer's instructions. In short, we washed cells once with PBS after the desired treatment and replaced the media with calcein AM diluted in PBS (working concentration of 2 μM). After 30 minutes at 37°C, we measured fluorescence at 485 nm excitation/520 nm emission with the Infinite 200 PRO (Tecan, Männedorf Switzerland).

Quantification of NAD$^+$ & ATP levels with HPLC. To quantify the NAD$^+$ and ATP levels of mouse retina, pooled rod-enriched isolates, or 661W cells, we performed reverse-phase high-performance liquid chromatography (HPLC) as described previously (Yoshino and Imai, 2013). We quantified NAD$^+$ and ATP levels based on the peak area on the HPLC spectrogram relative to a standard curve, and normalized these values to tissue weights for retinas, number of retinas for rod-enriched isolates, or based on cell number.

OCR and ECAR measurements. We performed detailed metabolic characterization of 661W cells after NAMPT inhibition using an XF96 Extracellular Flux Analyzer (Seahorse Bioscience, Billerica MA). After the desired treatment, we washed the cells three times and left them in 180

µL of prewarmed bicarbonate-free DMEM (pH 7.4). After 30-60 minutes in a non-CO_2 incubator, we simultaneously measured oxygen consumption rate (OCR) and extracellular acidification rate (ECAR) to quantify oxidative respiration and glycolytic flux, respectively, both at baseline and after sequential treatments of 1.5 µM oligomycin, 1.0 µM carbonyl cyanide 4-(trifluoromethoxy) phenylhydrazone (FCCP), and a combination of 1.0 µM antimycin A and 1.0 µM rotenone. Each 5-minute measurement period was preceded by 2 minutes of mixing and a 1-minute pause; we made 3 sequential measurements per treatment condition.

SIRT3-5 and *Nampt* **knockdown in 661W cells.** We transfected 661W cells with custom LNA longRNA GapmeRs reagents (Exiqon, Woburn MA) targeting *SIRT3*, *SIRT4*, or *SIRT5* at a final concentration of 100 nM, and commercially available siRNA targeting *Nampt* (Mm_Pbef1_5; Qiagen, Valencia CA) at a final concentration of 50 nM. In short, we seeded 661W cells and allowed them to adhere for 30 minutes. We prepared the transfection complexes by incubating the appropriate GapmeR/siRNA with Lipofectamine RNAiMAX transfection reagent (Invitrogen, Grand Island NY) for 5 minutes at room temperature (1.0 µl or 2.4 µl of RNAiMAX per well for the 96-well and 24-well plate formats, respectively). We confirmed knockdown efficiency with real-time PCR.

Light-induced degeneration (LID). We performed light-induced degeneration as described previously (Grimm and Reme, 2013). In short, we dilated pupils with two sequential drops of 1.0% atropine sulfate and 1.0% tropicamide (Bausch & Lomb, Tampa FL), and then exposed the mice to 13,000 lux from fluorescent lights suspended directly over the mice. We placed the mice in clear plastic cages that were surrounded on all sides with reflective aluminum foil and re-

dilated pupils with two additional drops every 2 hours. We assessed retinal function 4 days

following light-induced degeneration by ERG as described above. All the mice we tested carried

the RPE65$^{Leu/Leu}$ variant, making them equally vulnerable to light-induced degeneration (Wenzel

et al., 2001).

Krebs cycle enzymatic activity assays. We performed retinal dissociation by incubating

dissected retinas in 12 U/ml papain (Sigma, St. Louis MO) and 5 mM L-cysteine in DMEM for

30 minutes on a small vibrating aquarium pump at room temperature. After washing away

residual papain with 5 exchanges to fresh DMEM, we triturated the samples with fire-polished

Pasteur pipets. We then separated rod photoreceptors with the EasySEP Mouse PE Positive

Selection Kit (Stem Cell Technologies, Vancouver Canada) and PE-conjugated anti-CD73

antibodies (Miltenyi Biotec, Bergisch Gladback Germany). We measured the enzymatic activity

of NAD$^+$-dependent isocitrate dehydrogenase (NAD-IDH/IDH3), alpha-ketoglutarate

dehydrogenase (AGDH), and malate dehydrogenase (MDH) in these rods with assay kits from

Sigma (St. Louis MO) according to the manufacturer's instructions. We normalized enzymatic

activity to total protein and/or viable rod cell number.

Western Blotting for mitochondrial protein acylation. We isolated mitochondria from 661W

cells as described previously (Frezza et al., 2007). We denatured mitochondrial lysates in

NuPAGE LDS Sample Buffer and NuPAGE Sample Reducing Agent (Thermo Fisher, Carlsbad

CA) for 10 minutes at 70°C, loaded them into 4-12% Novex Bis-Tris Protein Gels, and then ran

them at 50 V for 15 minutes followed by 150 V for 60 minutes. We transferred the gel to a 0.2

μm nitrocellulose membrane (Bio-Rad, Hercules CA) in transfer buffer (192 mM glycine, 25 nM

43

Tris-base, 10% methanol) for 60 minutes at a constant current of 400 mA. We blocked the membranes for 60 minutes at room temperature with 5% (w/v) bovine serum albumin (BSA; Sigma) in TBS with 0.05% Tween-20 (0.05% TBST). We then stained the membranes overnight at 4°C with 1:1,000 anti-acetyllysine (#9441; Cell Signaling Technology, Danvers MA), 1:1,000 anti-succinyllysine (PTM-401; PTM BioLabs, Chicago IL), 1:1,000 anti-malonyllysine (PTM-901; PTM BioLabs), or 1:1,000 anti-glutaryllysine (PTM-1151; PTM BioLabs) diluted in blocking buffer. We then washed the membranes and incubated them for 60 minutes at room temperature with the appropriate secondary antibody conjugated to either IRDye 800CW or IRDye 680LT (LI-COR, Lincoln NE) diluted 1:5,000 in blocking buffer. We detected proteins and analyzed the band densities with the Odyssey Infrared Imaging System (LI-COR). We normalized protein loading per lane with the Pierce BCA Protein Assay Kit (Thermo Fisher, Carlsbad CA) and used anti-COX IV (4D11-B3-E8) antibody (#11967; Cell Signaling Technology) as the loading control.

SIRT3 and SIRT5 activity assays. We measured the SIRT3 activity and SIRT5 activity of mitochondrial isolates from 661W cells with commercially available kits (Abcam, Milton Cambridge; Enzo Life Sciences, Farmingdale NY; respectively) according to manufacturer's instructions. We did not add exogenous SIRT3/5 or NAD$^+$ to the reaction mixture to allow us to accurately quantify native deacylase activity.

Statistics. We performed statistical testing with GraphPad Prism (Version 6.0), using the appropriate test for each data set. Prior to all data analysis, we assessed the normality of the data

44

graphically and with the Kolmogorov-Smirnov test and, when necessary, used appropriate non-parametric alternatives. We defined statistical significance as a P-value < 0.05.

2.6   Acknowledgements

analyzing retinal samples, and Dr. Raul Mostoslavsky for providing resources. R.S.A. is a co-founder of Metro Midwest Biotech, which is developing NMN-based therapeutics.
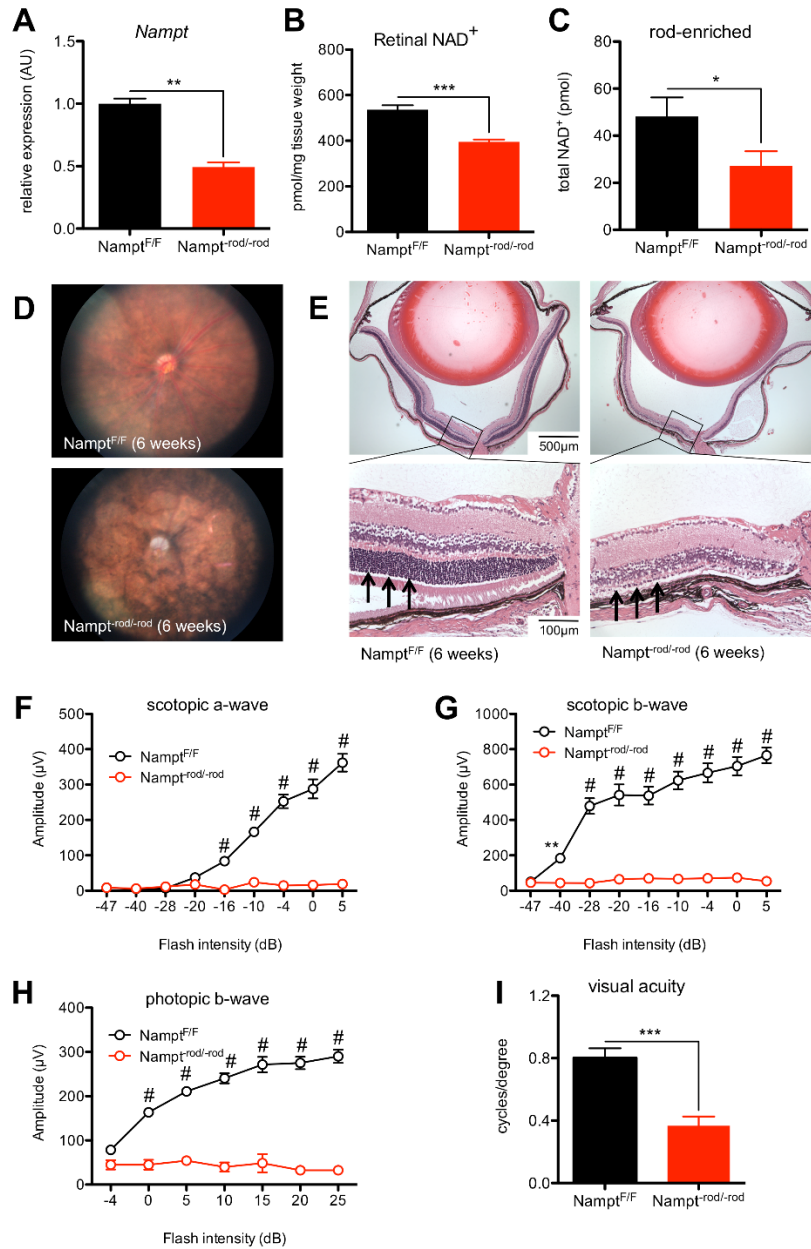
Figure 2.1. *Nampt*[-rod/-rod] mice exhibit severe retinal degeneration. (A) Rod-specific deletion of *Nampt* caused significant reduction in *Nampt* mRNA expression from rod-enriched retinal isolates (N=7 isolates/group; Mann-Whitney U test). (B) *Nampt*[-rod/-rod] retinas had lower NAD$^+$ levels than *Nampt*[F/F] retinas (N=5-8 retinas/group; 2-tailed, unpaired t-test). (C) Rod-enriched retinal isolates from *Nampt*[-rod/-rod] mice had lower NAD$^+$ levels than those from *Nampt*[F/F] mice (N=9-10 pooled samples/group; 1-tailed, unpaired t-test). (D) Representative fundus images from *Nampt*[-rod/-rod] mice demonstrated severe signs of retinal degeneration including vascular attenuation and optic nerve atrophy. (E) Representative retinal sections from *Nampt*[-rod/-rod] mice at 6 weeks stained with hematoxylin & eosin showed significantly reduced outer nuclear layer thickness (see arrows) with secondary retinal degeneration. (F-H) *Nampt*[-rod/-rod] mice exhibited impaired retinal function on ERG (N=5 *Nampt*[F/F] mice/10 *Nampt*[-rod/-rod] mice; 2-way mixed ANOVA with Bonferroni post-hoc test), and reduced photopic visual acuity (I; N=5-6 mice/group; 2-tailed, unpaired t-test). Graphs depict mean + S.E.M. (A-C, I) or mean ± S.E.M. (F-H) (* $P < 0.05$; ** $P < 0.01$; *** $P < 0.001$; # $P < 0.0001$).
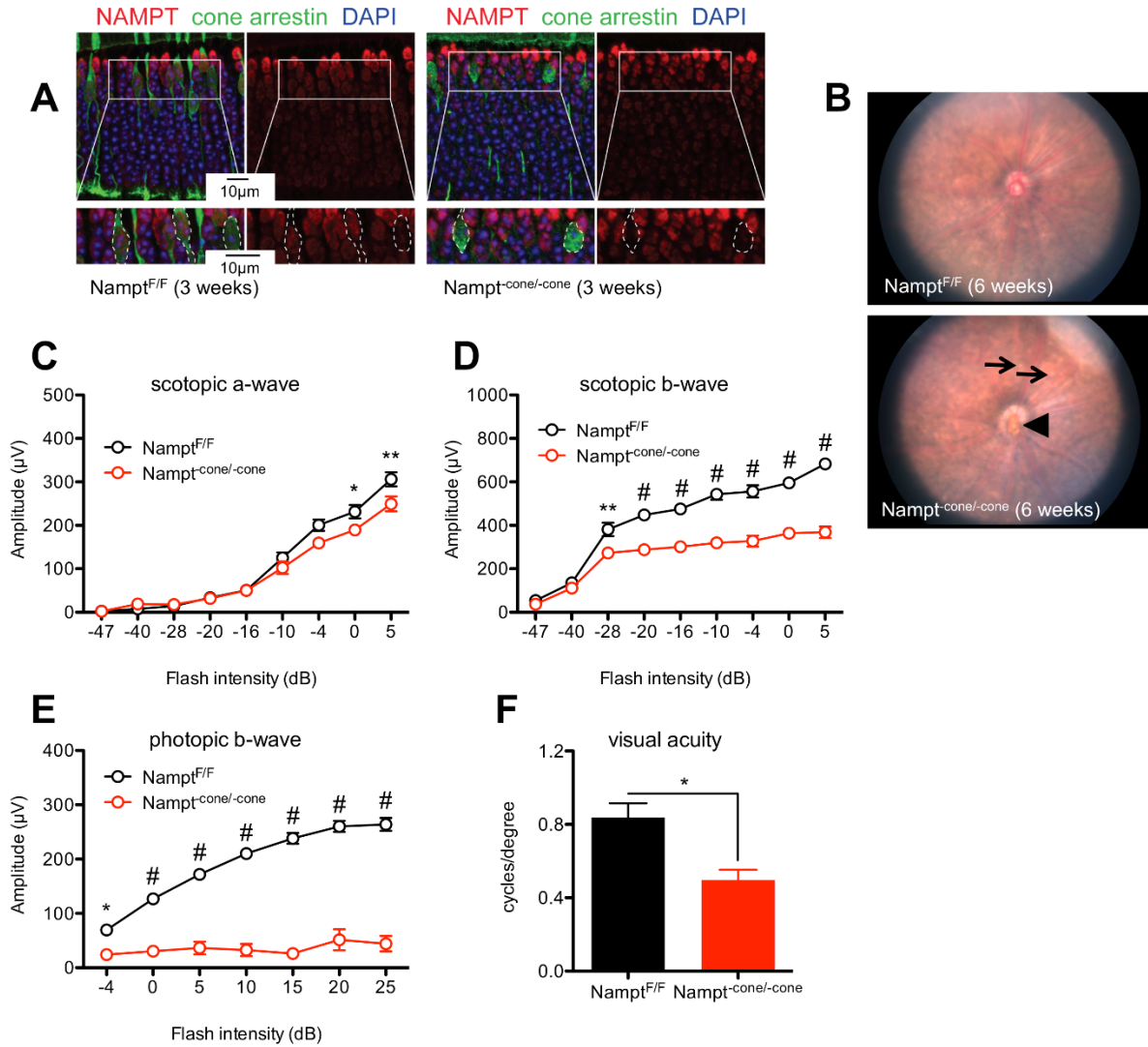
Figure 2.2. *Nampt*[-cone/-cone] mice exhibit cone-specific degeneration. (A) Cone-specific deletion of *Nampt* caused reduced intracellular NAMPT staining (red) in cone photoreceptors stained with cone-arrestin (green) and the nuclear DAPI stain (blue). (B) Representative fundus images from Nampt[-cone/-cone] mice demonstrated retinal pigment epithelial cell mottling (arrows) and optic nerve atrophy (arrowhead) consistent with mild retinal degeneration. (C-E) *Nampt*[-cone/-cone] mice also exhibited impaired retinal function on ERG (N=8-10 mice/group; 2-way mixed ANOVA with Bonferroni post-hoc test) and reduced photopic visual acuity (F; N=4 mice/group; Mann-Whitney U test). Graphs depict mean + S.E.M. (F) or mean ± S.E.M. (C-E) (* $P < 0.05$; ** $P < 0.01$; # $P < 0.0001$).
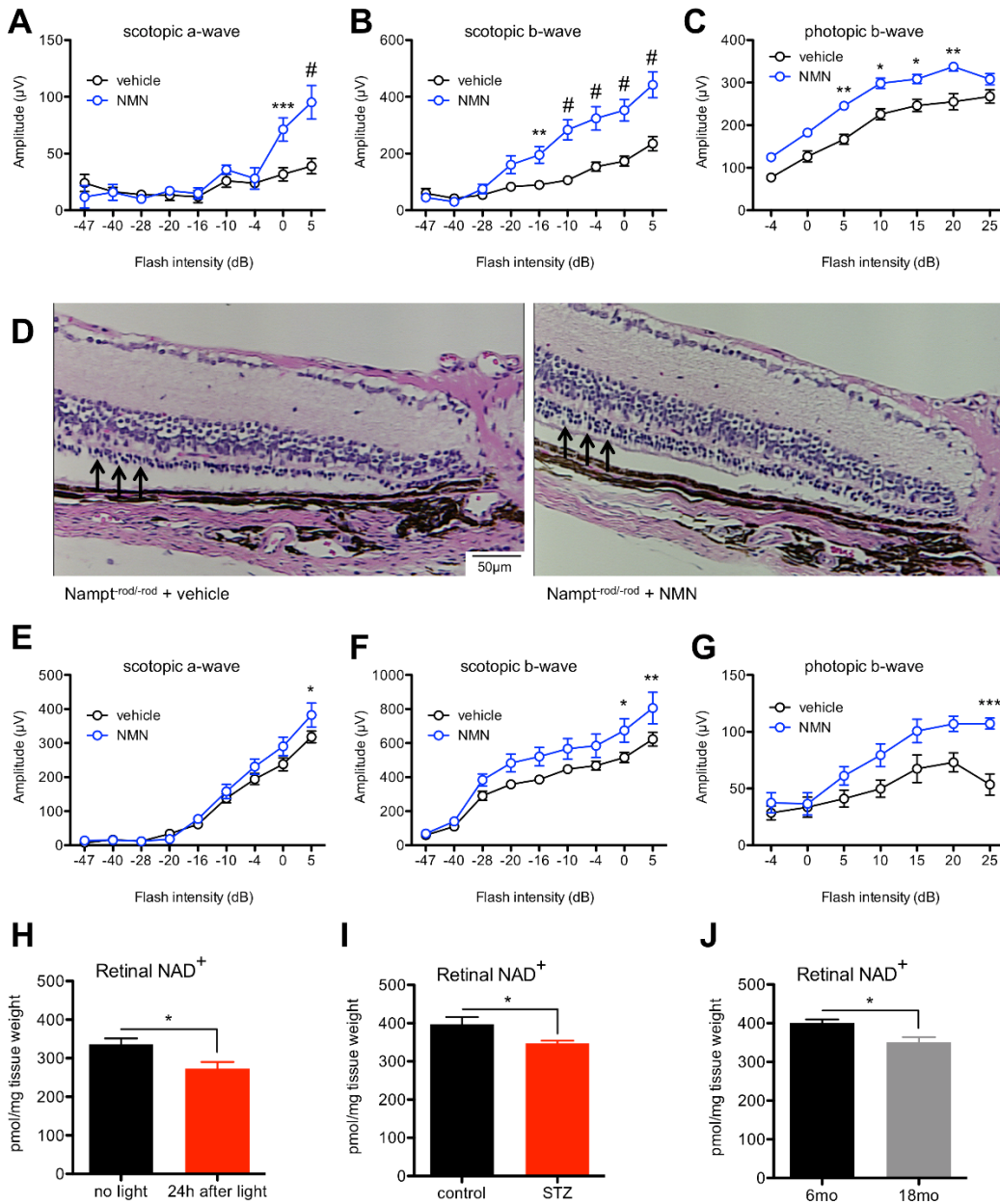
Figure 2.3. Exogenous NMN protects against retinal degeneration in mice lacking *Nampt* and may have efficacy against diverse retinal degenerative diseases. (A-C) *Nampt*[-rod/-rod] mice receiving daily intraperitoneal injections of 150 mg/kg NMN beginning at P5 had improved retinal function on ERG (N=12 vehicle/5 NMN; 2-way mixed ANOVA with Bonferroni post-hoc test) compared to vehicle-treated mice, consistent with relative preservation of the outer nuclear layer on histology (D; see arrows). (E-G) *Nampt*[-cone/-cone] mice receiving daily intraperitoneal injections of 150 mg/kg NMN beginning at P5 also had improved retinal function on ERG (N=9 vehicle/5 NMN; 2-way mixed ANOVA with Bonferroni post-hoc test). Retinal NAD$^+$ deficiency is a feature of multiple mouse models of retinal dysfunction, including light-induced degeneration (H; N=10-12/group; 2-tailed, unpaired t-test), streptozotocin-induced diabetic retinopathy (I; N=5/group; 2-tailed, unpaired t-test), and age-associated retinal dysfunction (J; N=5/group; 2-tailed, unpaired t-test). Graphs depict mean + S.E.M. (H-J) or mean ± S.E.M. (A-C, E-G) (* P < 0.05; ** P < 0.01; *** P < 0.001; # P < 0.0001).

49
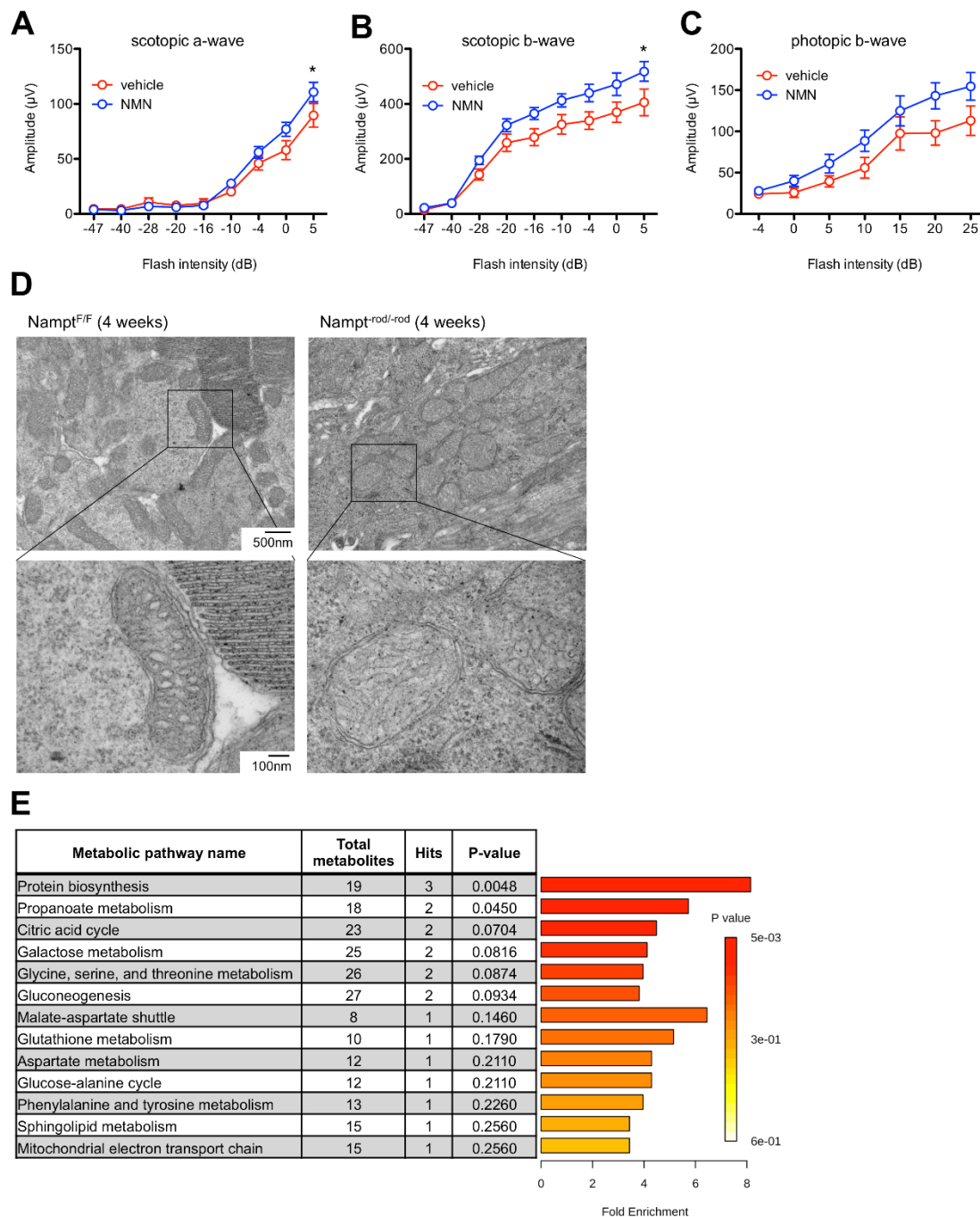
Figure 2.4. NAD$^+$ deficiency disrupts retinal energy homeostasis and can be rescued with exogenous NMN. (A-C) Wild-type mice (129S1/SvImJ) receiving intraperitoneal injections of 300 mg/kg NMN were more resilient against light exposure (N=8/group; 2-way mixed ANOVA with Bonferroni post-hoc test) compared to vehicle-treated mice. (D) Representative electron microscopy images of retinas from 4-week old *Nampt*$^{-rod/-rod}$ mice revealed mitochondria that are rounded, disorganized, and with loss of cristae compared to those from *Nampt*$^{F/F}$ mice. (E) *Nampt*$^{-rod/-rod}$ retinas also exhibited significant disruption of numerous metabolic pathways on metabolite set enrichment analysis. Graphs depict mean ± S.E.M. (A-C) (* $P < 0.05$).

Panel E table:

Metabolic pathway name	Total metabolites	Hits	P-value
Protein biosynthesis	19	3	0.0048
Propanoate metabolism	18	2	0.0450
Citric acid cycle	23	2	0.0704
Galactose metabolism	25	2	0.0816
Glycine, serine, and threonine metabolism	26	2	0.0874
Gluconeogenesis	27	2	0.0934
Malate-aspartate shuttle	8	1	0.1460
Glutathione metabolism	10	1	0.1790
Aspartate metabolism	12	1	0.2110
Glucose-alanine cycle	12	1	0.2110
Phenylalanine and tyrosine metabolism	13	1	0.2260
Sphingolipid metabolism	15	1	0.2560
Mitochondrial electron transport chain	15	1	0.2560

www.manaraa.com

Figure 2.5. NAMPT inhibition causes metabolic dysfunction and photoreceptor death. (A-B) NAMPT inhibition with 20 μM FK866 caused loss of reductive capacity in 661W cone photoreceptor-like cells by 24 hours and 48 hours (N=15/group from three independent experiments; 1-way ANOVA with Tukey post-hoc test). (C-D) This metabolic dysfunction caused cell death by 48 hours (N=14/group from three independent experiments; 1-way ANOVA with Tukey post-hoc test). The effects of NAMPT inhibition were rescued with 100 μM NMN (A-B, D). (E) NAMPT inhibition with 20 μM FK866 led to a significant reduction in total NAD^+ in photoreceptor cells by 6 hours, which was restored to near-normal levels with 100 μM NMN (N=3/group; 1-way ANOVA with Tukey post-hoc test). (F) 24 hours of 20 μM FK866 treatment led to undetectable levels of NAD^+ (N.D. = not detected), which once again was restored with 100 μM NMN (N=5-7/group). (G) NAMPT inhibition also caused ATP depletion but in a delayed time frame relative to NAD^+ depletion (N=4/group). (H-I) FK866-treated photoreceptor cells had reduced oxygen consumption rate (OCR) and extracellular acidification rate (ECAR) at baseline, impaired ECAR acceleration after oligomycin treatment, and impaired OCR acceleration after FCCP treatment (N=15-16/group from representative experiment; 2-way mixed ANOVA with Bonferroni post-hoc test). 100 μM NMN restored normal metabolic responses (H-I). (J) NAD^+-dependent isocitrate dehydrogenase (NAD-IDH/IDH3) activity was reduced in rods isolated from $Nampt^{-rod/-rod}$ mice compared to those isolated from $Nampt^{F/F}$ mice, even when sufficient NAD^+ was added to the reaction mixture (N=6/group from three independent experiments; 2-tailed, unpaired t-test) and despite similar *Idh3a* expression levels (K; N=11-13/group from three independent experiments; 2-tailed, unpaired t-test). (L-M) The activities of other NAD^+-dependent enzymes alpha-ketoglutarate dehydrogenase (AGDH; N=5/group from three independent experiments; Mann-Whitney U test) and malate dehydrogenase (MDH; N=7/group from three independent experiments; 2-tailed, unpaired t-test) in rods from $Nampt^{-rod/-rod}$ mice were restored with exogenous NAD^+. Graphs depict mean + S.E.M. (A-F, J-M) or mean ± S.E.M. (G-I) (* $P < 0.05$; ** $P < 0.01$; *** $P < 0.001$; # $P < 0.0001$; red: vehicle versus FK; blue: FK versus FK+NMN).

51
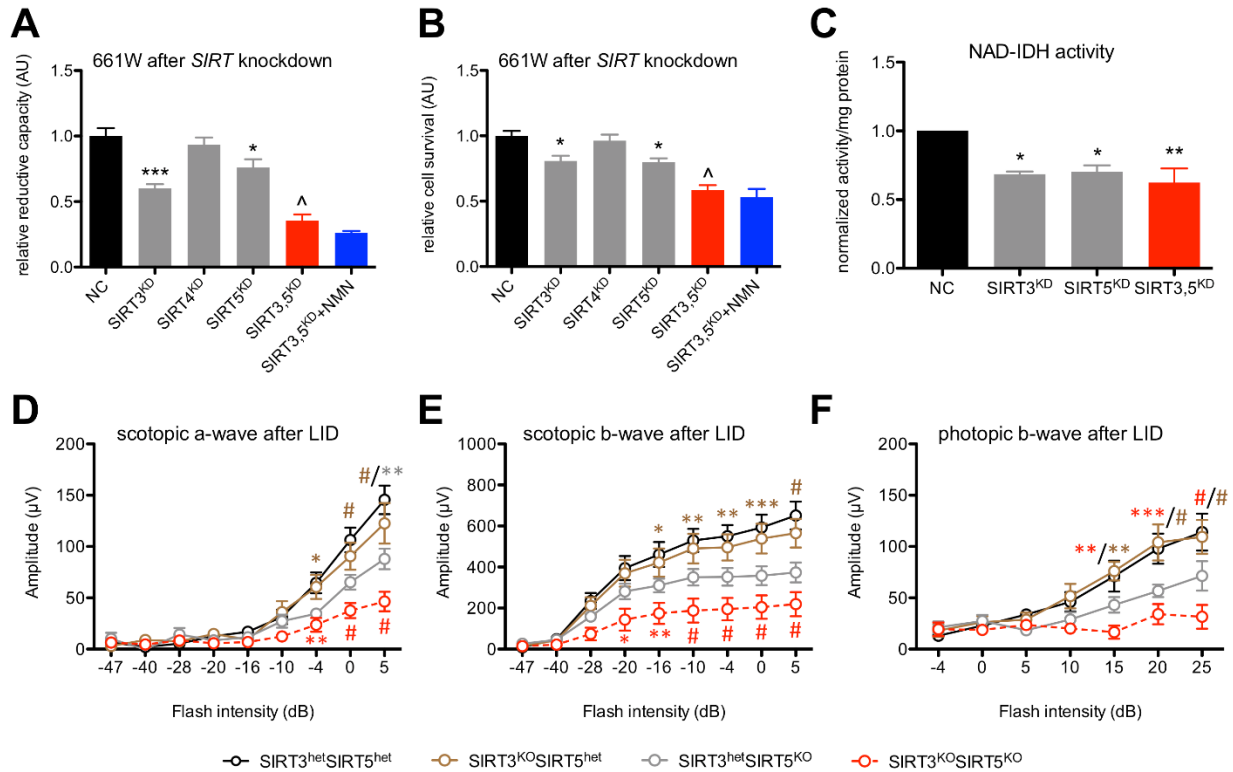
Figure 2.6. SIRT3 and SIRT5 are essential for photoreceptor survival. (A) Individual SIRT3 and SIRT5 knockdown but not SIRT4 knockdown caused significant loss of reductive capacity relative to negative control (NC); combined SIRT3/SIRT5 knockdown caused significantly more loss of reductive capacity than individual knockdowns, which could not be rescued with NMN (N=6/group from representative experiment; 1-way ANOVA with Tukey post-hoc test). (B) Individual SIRT3 and SIRT5 knockdown but not SIRT4 knockdown caused significant cell death relative to negative control (NC); combined SIRT3/SIRT5 knockdown caused significantly more cell death than individual knockdowns, which could not be rescued with NMN (N=18/group from three independent experiments; 1-way ANOVA with Tukey post-hoc test). (C) Individual and combined SIRT3/SIRT5 knockdowns recapitulated NAD-IDH dysfunction compared to negative control (NC; N=3/group from three independent experiments; 1-way ANOVA with Tukey post-hoc test). (D-F) Mice lacking SIRT3 and SIRT5 (SIRT3^{KO}SIRT5^{KO}) were significantly more vulnerable to light-induced degeneration (LID) compared to SIRT3^{het}SIRT5^{het} mice, while SIRT3^{KO}SIRT5^{het} and SIRT3^{het}SIRT5^{KO} mice exhibited intermediate vulnerability to LID (N=5-7 mice/group; 2-way mixed ANOVA with Bonferroni post-hoc test). Graphs depict mean + S.E.M. (A-C) or mean ± S.E.M. (D-F) (* $P < 0.05$; ** $P < 0.01$; *** $P < 0.001$; # $P < 0.0001$; ^ $P < 0.05$ relative to both SIRT3^{KD} and SIRT5^{KD}; red: SIRT3^{het}SIRT5^{het} versus SIRT3^{KO}SIRT5^{KO}; brown: SIRT3^{KO}SIRT5^{het} versus SIRT3^{KO}SIRT5^{KO}; grey: SIRT3^{het}SIRT5^{KO} versus SIRT3^{KO}SIRT5^{KO}).
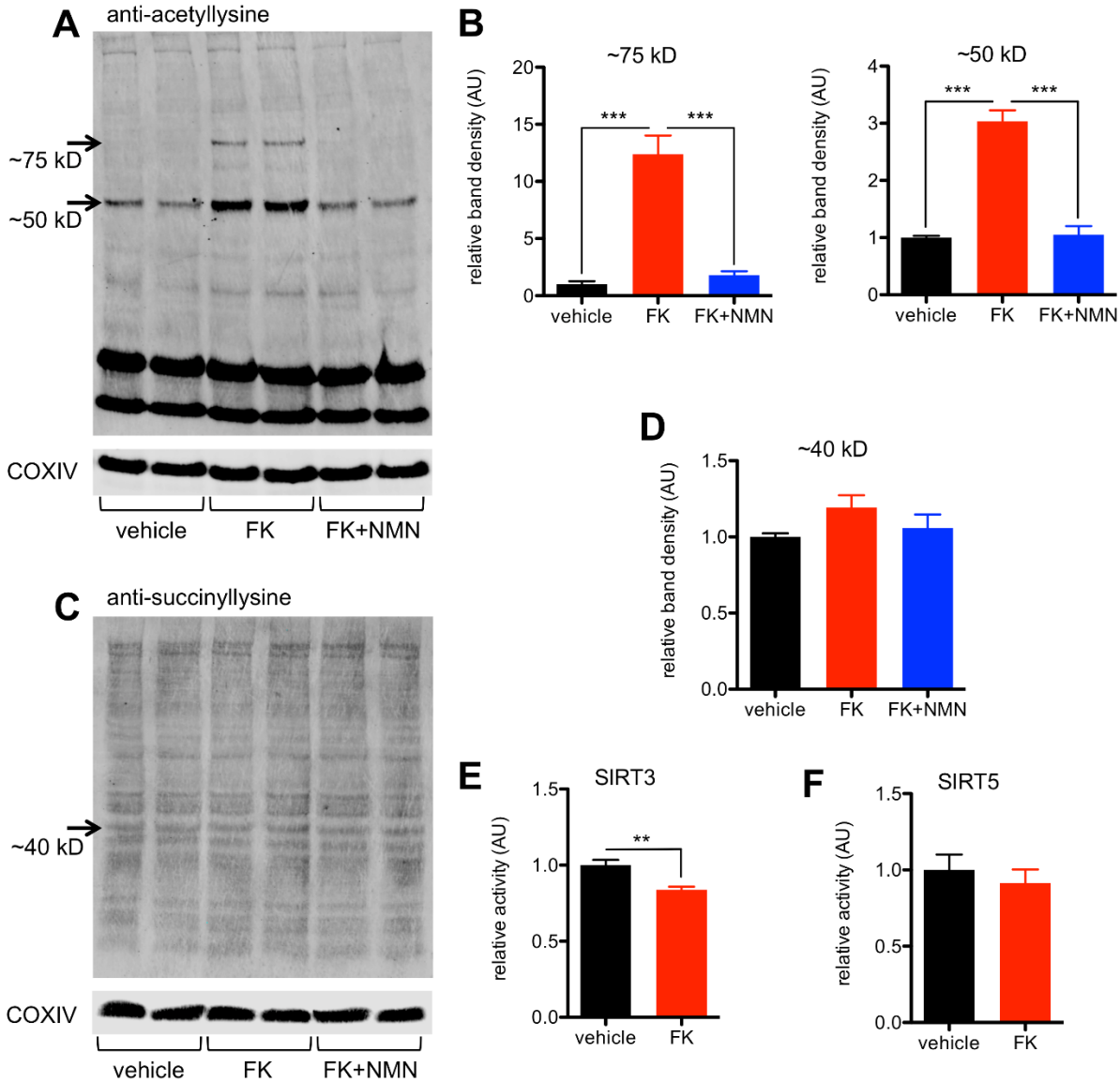
Figure 2.7. NAD$^+$ deficiency impairs mitochondrial sirtuin function. (A-B) NAMPT inhibition caused selective mitochondrial protein hyperacetylation (N=4 biological replicates from two independent blots; 1-way ANOVA with Tukey post-hoc test). (C-D) NAMPT inhibition caused only modest changes in mitochondrial protein succinylation (N=6 biological replicates from three independent blots; 1-way ANOVA with Tukey post-hoc test). (E) NAD$^+$ deficiency impaired SIRT3 activity (N=6/group; 2-tailed, unpaired t-test) but not SIRT5 activity (F; N=15-16/group; 2-tailed, unpaired t-test). Graphs depict mean + S.E.M. (B, D-F) (** $P < 0.01$; *** $P < 0.001$).

Chapter 3:

Oxysterol Signatures Distinguish Age-Related Macular Degeneration from Physiologic Aging

This chapter is adapted from a manuscript that is published in *EBioMedicine*.

J.B.L. & A. Sene = co-first authors

Conceptualization: R.S.A., A. Sene, J.B.L.
Investigation: J.B.L., A. Sene, A. Santeford, H.F., R.S., M.M.L., V.A.S., N.B.
Writing – Original Draft: J.B.L., A. Sene
Writing – Review & Editing: J.B.L., A. Sene, R.S.A., D.S.O., N.B., M.M.L., H.F., V.A.S.
Supervision: R.S.A., D.S.O., I.U.M.
Funding Acquisition: R.S.A., D.S.O., I.U.M.

3.1   Summary

Macrophage aging is pathogenic in numerous diseases, including age-related macular degeneration (AMD), a leading cause of blindness in older adults. Although prior studies have explored the functional consequences of macrophage aging, less is known about its cellular basis or what defines the transition from physiologic aging to disease. Here, we show that despite their frequent self-renewal, macrophages from old mice exhibited numerous signs of aging, such as impaired oxidative respiration. Transcriptomic profiling of aged murine macrophages revealed dysregulation of diverse cellular pathways, especially in cholesterol homeostasis, that manifested in altered oxysterol signatures. Although the levels of numerous oxysterols in human peripheral blood mononuclear cells and plasma exhibited age-associated changes, plasma 24-hydroxycholesterol levels were specifically associated with AMD. These novel findings demonstrate that oxysterol levels can discriminate disease from physiologic aging. Furthermore, modulation of cholesterol homeostasis may be a novel strategy for treating age-associated diseases in which macrophage aging is pathogenic.

3.2 Introduction

Age-related macular degeneration (AMD) is a leading cause of blindness in adults over 50 years of age in industrialized nations (van Leeuwen et al., 2003). Early AMD is characterized by the presence of lipoproteinaceous deposits or drusen under the retinal pigment epithelium (RPE) and/or thickening of Bruch's membrane. Although early AMD is not always associated with vision loss, it is a major risk factor for progression to one of two forms of advanced AMD: a dry form, characterized by death of RPE cells called geographic atrophy (GA) that eventually leads to death of overlying photoreceptors, or wet (neovascular) AMD, characterized by abnormal vascular proliferation underneath the retina called choroidal neovascularization (CNV). While both advanced dry and wet AMD can cause vision loss, wet AMD accounts for a significant fraction of the vision loss associated with AMD (Ferris et al., 1984) and can often be acute and catastrophic.

The current mainstay therapies for wet AMD focus on combating abnormal angiogenesis by blocking vascular endothelial growth factor (VEGF) with targeted anti-VEGF agents. These treatments stabilize disease in a majority of patients and significantly improve visual outcomes in 30-40% of wet AMD patients (Inoue et al., 2016; Kim et al., 2016; Sarwar et al., 2016). However, these therapies often require frequent visits for repeated intraocular injections, which place a significant burden on patients and caregivers (Haller, 2013). Moreover, repeated intravitreal injections are also associated with risks of their own, such as infection, scleral thinning, and long-term visual acuity loss due to continued atrophy of the RPE and photoreceptors (Sarwar et al., 2016; Zinkernagel et al., 2015). Perhaps more importantly, anti-VEGF agents do not address the pathophysiology that causes wet AMD (Sene et al., 2015). Therefore, there is need for further research to clarify the molecular and cellular mechanisms

56

involved in the transition from physiologic aging to AMD and to understand the pathogenesis underlying the progression from early to wet AMD, which may lead to novel strategies for targeted intervention.

In the past few decades, we and others have demonstrated that macrophages, key cells of the innate immune system, play important roles in the pathogenesis of wet AMD (Apte et al., 2006; Espinosa-Heidmann et al., 2003; Sakurai et al., 2003). Moreover, it has become increasingly clear that the ability of macrophages to polarize to different activation states is an important factor affecting whether macrophages promote health or disease (Mosser and Edwards, 2008). Depending on dynamic tissue signals and the surrounding micro-environment, macrophages can polarize to a classical pro-inflammatory (M1-like) phenotype, an alternative anti-inflammatory (M2-like) phenotype, or some intermediate between these two extremes (Sica and Mantovani, 2012). To further complicate matters, the identity of the specific activators that cause macrophage polarization may also affect the macrophage phenotype (Murray et al., 2014).

Previously, we reported that aged macrophages tend to skew to the anti-inflammatory M2-like phenotype and are less able to inhibit abnormal angiogenesis (Kelly et al., 2007). Furthermore, aged macrophages exhibit both impairments in cholesterol efflux (Sene et al., 2013) and abnormalities in IL-10 and downstream STAT3 signaling pathways that contribute to this age-associated drift towards M2-like polarization (Nakamura et al., 2015). These age-associated impairments in cholesterol efflux and other lipid-related pathways may have mechanistic consequences in disease pathogenesis (Sene and Apte, 2014). This possibility is supported by the fact that polymorphisms in lipid-related genes, such as hepatic lipase (LIPC), ATP-binding cassette transporter member 1 (ABCA1), and cholesterol ester transfer protein (CETP), are associated with advanced AMD (Neale et al., 2010). Moreover, drusen, a clinical

feature of early AMD, are lipid-rich, further supporting our hypothesis that dysregulated lipid homeostasis contributes to AMD. Despite these advances, the global programmatic changes that occur during macrophage aging need further elucidation. It is also unclear what subset of these changes are associated with physiologic aging or are pathologic and contribute to age-associated disease.

In this study, we sought to delineate the cellular pathways involved in macrophage aging and identify potential markers that may distinguish age-associated changes that are physiologic versus those that promote age-associated disease. Our results suggest that impaired cholesterol homeostasis in macrophages is a central process perturbed during aging and that these changes lead to changes in oxysterol signatures that can distinguish AMD from physiologic aging. These findings may allow physicians to monitor progression of disease with quantifiable serum markers and may potentially lead to novel therapeutic strategies not only for AMD but also for other age-associated diseases in which alternatively-activated macrophages are pathogenic.

3.3   Results

Peritoneal macrophages from old mice exhibit features of aging

Under steady-state conditions, tissue-resident macrophages are maintained through constant replacement or self-renewal. In many tissues, including the peritoneal cavity, there is extensive replacement of macrophages as quickly as every 3 weeks (Hashimoto et al., 2013). Therefore, we sought to determine whether macrophages isolated from old (i.e., 18-month-old) wild-type mice exhibited features of cellular aging when compared to macrophages isolated from young (i.e., 3-month-old) wild-type mice despite this short replenishment cycle.

58

Mitochondrial dysfunction is a well-established hallmark of aging, and in many tissues, there is an age-dependent decrease in mitochondrial oxygen consumption (Lopez-Otin et al., 2013). To determine whether peritoneal macrophages from old mice exhibit mitochondrial dysfunction, we measured the oxygen consumption rate (OCR) of peritoneal macrophages isolated from 3-month-old and 18-month-old mice. The baseline OCR of peritoneal macrophages from old mice was significantly lower than that of peritoneal macrophages from young mice **(Figure 3.1A)**, indicating reduced basal oxidative respiration. Although both young and aged peritoneal macrophages appropriately exhibited a reduction in OCR after treatment with the ATP synthase inhibitor oligomycin, young peritoneal macrophages maintained a somewhat higher residual OCR **(Figure 3.1A)**. In contrast, both young and aged peritoneal macrophages demonstrated similar maximal oxidative respiration in response to the uncoupling agent FCCP **(Figure 3.1A)**. The difference between the baseline OCR and the OCR after oligomycin treatment represents ATP-linked respiration. Aged peritoneal macrophages exhibited significantly reduced ATP-linked respiration **(Figure 3.1B)**, indicating mitochondrial dysfunction.

Moreover, previous studies report that exposing macrophages to lipopolysaccharide (LPS) considerably alters their bioenergetic profile (Tavakoli et al., 2013). Furthermore, such a metabolic switch is required for macrophage activation and affects its subsequent inflammatory status (Huang et al., 2014; Tavakoli et al., 2013; Vats et al., 2006). We observed distinct mitochondrial respiratory profiles when comparing young and aged, LPS-treated peritoneal macrophages: aged peritoneal macrophages exhibited a reduced OCR at baseline, despite maintaining similar responses to oligomycin and FCCP **(Figure 3.1C)**. Again, aged peritoneal macrophages exhibited significantly reduced ATP-linked respiration **(Figure 3.1D)**.

Cumulatively, these data demonstrate that mitochondrial oxidative metabolism is considerably impaired in peritoneal macrophages isolated from old mice both at baseline and in response to LPS.

Furthermore, we evaluated the expression of the aging marker $p16^{INK4a}$, which is a known senescence marker in bone marrow-derived macrophages (Randle et al., 2001) and has been shown to accumulate in rodent and human tissues during aging (Krishnamurthy et al., 2004; Nielsen et al., 1999; Zindy et al., 1997). We found that $p16^{INK4a}$ mRNA expression was significantly elevated in aged peritoneal macrophages compared to young peritoneal macrophages **(Figure 3.1E)**. Collectively, these results confirm that despite their constant renewal, peritoneal macrophages from old mice exhibit multiple quantifiable signs of aging, including mitochondrial dysfunction and increased expression of the senescence marker, $p16^{INK4a}$.

Aged macrophages exhibit impaired cholesterol homeostasis

To determine the specific cellular processes that are perturbed in aged macrophages, we profiled the transcriptomes of young and aged macrophages with the GeneChip Mouse Gene 1.0 ST Array (Affymetrix, Santa Clara, CA). We found that 1,080 probe sets were significantly differentially expressed in aged versus young macrophages **(Figure 3.2A**; P < 0.05, FDR < 0.20). The twenty protein-coding genes that were up- or downregulated with the highest fold change in aged versus young macrophages are presented in **Table 3.1**. To determine whether the identities of the dysregulated genes were associated with defects in particular pathways or cellular processes, we filtered for genes with a 1.50-fold-change cutoff (22.1%, N = 239) and then performed gene ontology (GO) and pathway map analysis with MetaCore^TM (Clarivate

Analytics, Philadelphia, PA). Of interest, the first, second, and tenth most significant GO processes implicated were sterol biosynthesis, cholesterol biosynthesis, and cholesterol metabolism, respectively **(Figure 3.2B)**. Consistently, cholesterol biosynthesis was the most significant pathway implicated by the altered transcriptomic profile of aged macrophages **(Figure 3.2C)**. As expected, the transcriptomic profile of aged macrophages also suggested disruptions in numerous other immune response pathways **(Figure 3.2C)**. Overall, these results clearly indicate that cholesterol homeostasis is significantly perturbed during macrophage aging.

Given that numerous genes were dysregulated in aged peritoneal macrophages, we sought to identify candidate transcription factors (TFs) that may regulate the aging process. Therefore, we performed interactome analysis to identify over-connected TFs, which may regulate the observed transcriptomic changes in aged macrophages. Of interest, two of the top five most significantly overconnected TFs were sterol regulatory element-binding protein 1 and 2 (SREBP1/SREBP2; **Figure 3.2D)**, which are known master regulators of cholesterol and lipid homeostasis. These two TFs had connectivity ratios of 14.73 and 15.15, respectively, indicating ~15-fold overrepresentation of their known targets. These findings support our assertion that global lipid homeostatic mechanisms are impaired in aged macrophages.

To determine the specific aspects of cholesterol homeostasis that are impaired in aged macrophages, we analyzed the expression profile of 113 lipid-related genes in young and aged macrophages with a custom quantitative PCR array (Applied Biosystems). We were able to detect expression of 86.7% (N = 98) of the genes we tested and found that 30 of these 98 cholesterol-related genes (30.6%) had significantly different expression in aged versus young macrophages **(Table 3.2)**. When we subdivided these lipid-related genes broadly by their cellular function, we observed that they encompassed diverse biological processes, including

61

cholesterol/lipid biosynthesis, elimination, transport, and uptake, among other processes. These findings once again confirmed that aged peritoneal macrophages exhibit global impairments in their ability to maintain cholesterol and lipid homeostasis.

Aged macrophages have altered intracellular oxysterol content

We previously reported that aged macrophages have higher levels of intracellular cholesterol related to impaired efflux (Sene et al., 2013), suggestive of the global changes in cholesterol homeostatic mechanisms described above. The oxidation of cholesterol to generate oxidized derivatives of cholesterol, or oxysterols, serves a crucial purpose to facilitate elimination of excess cholesterol. However, oxysterols themselves also play important signaling roles in regulating cholesterol homeostasis (Spann and Glass, 2013) and inflammation (Poli et al., 2013) and may therefore promote disease. In addition, aberrant oxysterol production can be a sign of increased oxidative stress, which is known to be pathogenic in AMD (Datta et al., 2017). Since our transcriptomic profiling demonstrated that impaired cholesterol homeostasis is a hallmark feature of aged macrophages, we sought to explore whether these changes were associated with altered oxysterol signatures, which would not only provide mechanistic insight into why there is impaired cholesterol homeostasis but also identify a potential approach for detecting defective cholesterol homeostasis.

Using liquid chromatography tandem mass spectrometry (LC-MS/MS), we measured the most abundant oxysterols, including 4β-hydroxycholesterol (4β-HC), 7-ketocholesterol (7-KC), and cholestane-3β,5α,6β-triol (C-triol) in young and aged peritoneal macrophages. We found that aged peritoneal macrophages contained more 4β-HC and 7-KC compared to young peritoneal macrophages, both at baseline and after treatment with 25 or 50 µg/ml oxidized LDL (oxLDL)

62

(Figures 3.3A and 3.3B). Aged peritoneal macrophages also had increased C-triol content at baseline and after treatment with oxLDL, but the difference was statistically significant only after treatment with 50 μg/ml oxLDL **(Figure 3.3C)**. To account for the possibility that these increases in intracellular oxysterols may have been influenced by environmental factors, we also tested a separate cohort of young and aged mice that were housed at the same animal facility. Consistent with our original findings, these aged peritoneal macrophages also had increased levels of 4β-HC, 7-KC, and C-triol after treatment with 50 μg/ml oxLDL (data not shown). These findings demonstrate that aged peritoneal macrophages have increased intracellular oxysterols upon challenge with oxLDL and that this difference is likely an effect of age rather than environmental factors.

We also measured the oxysterol content in the supernatant of peritoneal macrophages to determine whether increased intracellular oxysterol content was associated with increased oxysterol secretion. Although some comparisons were statistically significant due to low within-group variance, the levels of 4β-HC, 7-KC, and C-triol were qualitatively similar in the supernatant of both young and aged peritoneal macrophages both at baseline and after treatment with oxLDL **(Figures 3.3D, 3.3E, and 3.3F)**. Of note, the levels of 4β-HC and 7-KC detected in equivalent dilutions of oxLDL were similar to those detected in the supernatants of both young and aged peritoneal macrophages **(Figures 3.3D and 3.3E)**, suggesting that any differences in the secretion of these two oxysterols were likely masked by the oxysterols present in the oxLDL itself.

Our finding of increased intracellular oxysterols in the absence of changes in extracellular levels suggested that there is increased oxysterol synthesis associated with aging rather than changes in uptake. In support of this hypothesis, we previously reported that young and aged

63

macrophages have similar capacity to influx Dil-labeled oxLDL (Sene et al., 2013). Furthermore, using flow cytometry, we found that surface expression of CD36, a receptor for oxLDL uptake, was similar in young and aged peritoneal macrophages **(Figures 3.3G, 3.3H, and 3.3I)**, supporting that differences in intracellular oxysterols were not likely due to differences in uptake.

To determine whether these aging-associated changes in oxysterol signatures were specific to elicited peritoneal macrophages, we also measured intracellular oxysterol content and secretion in young and aged splenic macrophages as an example of a tissue-resident macrophage. We found that aged splenic macrophages had similar patterns of increased intracellular oxysterols **(Figures 3.4A, 3.4B, and 3.4C)** with minimal changes in extracellular oxysterols **(Figures 3.4D, 3.4E, and 3.4F)**. These findings indicate that impaired cholesterol homeostasis is associated with detectable alterations in the oxysterol signatures in aged macrophages of multiple origins.

PBMC and plasma oxysterol signatures are altered with age in humans

We have previously demonstrated that aged murine macrophages exhibit functional shifts that are associated with their tendency to promote AMD (Apte et al., 2006; Nakamura et al., 2015; Sene et al., 2013). However, it remains unclear which subset of the age-associated changes described above promotes disease rather than being a part of physiologic aging. To discriminate between these physiologic versus pathologic changes, we assessed whether PBMCs and plasma samples from healthy human subjects also exhibited changes in oxysterol signatures with age and whether these changes were different in AMD patients. We chose to process the human

64

samples minimally without cell sorting or cultures to explore how these oxysterol signatures could be used clinically. Demographic information of the human subjects is shown in **Table 3.3**.

In addition to measuring the same oxysterols we measured in murine peritoneal macrophages (i.e., 4β-HC, 7-KC, and C-triol), we were also able to quantify levels of two additional enzymatically generated oxysterols, 24-hydroxycholesterol (24-HC) and 27-hydroxycholesterol (27-HC), which were below the limit of detection in the murine samples. Of interest, we observed a statistically significant negative correlation between age and PBMC 7-KC levels **(Figure 3.5A**; Spearman R = -0.2964, P = 0.0204), PBMC C-triol levels **(Figure 3.5A**; Pearson R = -0.3068, P = 0.0171), and PBMC 24-HC levels **(Figure 3.5B**; Pearson R = -0.3058, P = 0.0165). There was no association between age and PBMC 4β-HC levels **(Figure 3.5A**; Spearman R = -0.0356, P = 0.7853) or PBMC 27-HC levels **(Figure 3.5B**; Pearson R = -0.0012, P = 0.9930). Additionally, we observed a significant positive correlation between age and plasma C-triol levels **(Figure 3.5C**; Pearson R = 0.2818, P = 0.0278). Although not statistically significant, there was a trend (0.05 < P < 0.10) toward a positive correlation between age and plasma 4β-HC levels **(Figure 3.5C**; Spearman R = 0.2170, P = 0.0930). There was no statistically significant correlation between age and plasma 7-KC levels **(Figure 3.5C**; Spearman R = 0.1172, P = 0.3683), plasma 24-HC levels **(Figure 3.5D**; Spearman R = 0.0394, P = 0.7631), or plasma 27-HC levels **(Figure 3.5D**; Pearson R = 0.1601, P = 0.2177). Overall, these findings suggest that healthy humans also exhibit age-associated alterations in oxysterol signatures, likely reflecting changes in cholesterol homeostasis.

Plasma 24-hydroxycholesterol distinguishes AMD from physiologic aging

To further characterize the relationship between age-associated oxysterol signatures and age-related disease, we recruited human patients with early or advanced neovascular (wet) AMD and measured their PBMC and plasma oxysterol levels **(Figures 3.6A, 3.6B, 3.6C, 3.6D, 3.6E, 3.6F, 3.6G, 3.6H, 3.6I, and 3.6J)**. While AMD patients were significantly older than non-AMD control subjects, there was no difference between the groups on the basis of gender **(Table 3.3)**. On average, AMD patients had decreased PBMC 7-KC levels compared to non-AMD controls **(Figure 3.6B)** but no differences in the other PBMC oxysterol levels **(Figures 3.6A, 3.6C, 3.6D, and 3.6E)**. Moreover, AMD patients had elevated plasma 4β-HC levels **(Figure 3.6F)**, elevated plasma C-triol levels **(Figure 3.6H)**, elevated plasma 24-HC levels **(Figure 3.6I)**, and a trend $(0.05 < P < 0.10)$ towards elevated plasma 27-HC levels **(Figure 3.6J)** compared to non-AMD controls. There was no difference in plasma 7-KC levels **(Figure 3.6G)**.

Given the known association between AMD and age and the significant age difference between our two groups, we performed binary logistic regression to precisely model the relationship between PBMC or plasma oxysterol levels and AMD after controlling for age and gender **(Table 3.4)**. We selected PBMC 7-KC, plasma 4β-HC, plasma C-triol, and plasma 24-HC levels as candidates for further analysis since these were the oxysterols that were significantly different between AMD patients and controls. The binary logistic regression model for a PBMC oxysterol AMD signature included age, gender, and untransformed PBMC 7-KC. The overall model was statistically significant (LR $X^2 = 34.0$, df = 3, P < 0.001) and had good fit $(X^2 = 9.6$, df = 8, P = 0.294)$. As expected, age was significantly associated with AMD (P < 0.001) with a beta coefficient of 0.098, indicating that each additional year of age was associated

with increased odds of having AMD (aOR = 1.10; 95% CI = 1.05 to 1.16). However, after controlling for age and gender, PBMC 7-KC levels were not associated with AMD (P = 0.140).

The binary logistic regression model for a plasma oxysterol AMD signature included forced entry of age and gender and selection of any combination of the candidate plasma oxysterol species through automated forward selection **(Table 3.5)**. The final model was statistically significant (LR X^2 = 44.9, df = 3, P < 0.001), had good fit (X^2 = 14.2, df = 8, P = 0.078), and included age, gender, and plasma 24-HC levels. As expected, age was significantly associated with AMD (P < 0.001) with a beta coefficient of 0.107, indicating that each additional year of age was associated with increased odds of having AMD (aOR = 1.113; 95% CI = 1.06 to 1.17). Of significant interest, even after controlling for age and gender, 24-HC levels were highly associated with AMD (P < 0.001) with a beta coefficient of 11.327, indicating that each additional 0.1-unit increase in relative plasma 24-HC levels was associated with a 3.10-fold increase in odds of having AMD (95% CI = 1.66 to 5.79). To determine the efficacy of plasma 24-HC levels as a potential marker for AMD, we generated a receiver operating characteristic (ROC) curve and found that the area under the ROC curve (AUC) was 0.866 (95% CI = 0.793 to 0.939), indicating good discrimination.

Furthermore, we performed conjunctive analysis to evaluate the clinical utility of using plasma 24-HC to discriminate between AMD patients and non-AMD subjects across varying ages. We divided patients into tertiles by plasma 24-HC levels and by age (i.e., above versus below median), tabulating the AMD prevalence in each conjoined cell **(Table 3.6)**. This analysis demonstrated a clear stepwise increase in prevalence of AMD in subjects above the median age going from the lowest to the highest tertile of plasma 24-HC (i.e., from 47.1% to 66.7% to 76.2%; **Figure 3.7A)**. We observed a similar increase in AMD prevalence in subjects below the

median age based on plasma 24-HC tertile (i.e., from 10.5% to 19.0% to 38.5%). These findings support the notion that plasma 24-HC levels can distinguish between the changes in oxysterols expected during physiologic aging versus those that suggest risk of AMD.

To determine the clinical utility of plasma 24-HC levels compared to existing clinical measures of lipid homeostasis, we next analyzed whether plasma 24-HC levels were correlated with total plasma cholesterol levels in the subjects for whom this information was available. In these subjects (N = 37), plasma 24-HC was indeed correlated with total plasma cholesterol (r = .659, P < 0.001). We therefore performed a subanalysis by generating a binary logistic regression for the outcome of AMD with forced entry of plasma 24-HC levels, total plasma cholesterol, age, and gender. This model was statistically significant (LR X^2 = 27.2, df = 4, P < 0.001) and had good fit (X^2 = 2.6, df = 7, P = 0.921). Of interest, total plasma cholesterol levels were not associated with AMD (aOR = 1.014; 95% CI = 0.97 to 1.06; P = 0.547). Remarkably, even after controlling for total plasma cholesterol, age, and gender, plasma 24-HC remained highly associated with AMD (P = 0.044) with a beta coefficient of 19.308, indicating that each additional 0.1-unit increase in relative plasma 24-HC levels was associated with a 6.90-fold increase in odds of having AMD (95% CI = 1.05 to 45.09). Despite the limited sample size available for this subanalysis, these findings suggest that human plasma 24-HC has strong diagnostic value compared to the existing measure of total plasma cholesterol.

Given the heterogeneity of the clinical progression of AMD and our interest in identifying factors that may predict transition to advanced disease, we also examined whether plasma 24-HC levels differed significantly when subdividing AMD patients into early AMD and advanced neovascular AMD patients. We did not detect a statistically significant difference in plasma 24-HC levels in early AMD versus advanced neovascular AMD patients **(Figure 3.7B)**.

Therefore, although 24-HC may be associated with AMD, it does not appear to have utility for predicting disease progression.

3.4   Discussion

In this study, we identified that despite their self-renewal, macrophages from old mice exhibit signs of aging, such as defects in mitochondrial oxidative respiration, that are not observed in macrophages from young mice. Consistent with these functional changes, aged macrophages exhibit an altered transcriptomic profile, especially in genes involved in cholesterol homeostasis. These findings build on our previous study reporting that *Abca1* expression is significantly reduced in aged macrophages, leading to impaired cholesterol efflux (Sene et al., 2013). We further demonstrate that impairments in cholesterol homeostatic mechanisms are not restricted solely to efflux but globally affect numerous pathways, including biosynthesis, elimination, transport, and regulation. Interestingly, aged macrophages exhibited simultaneous downregulation and upregulation of different genes with similar functions in cholesterol-related pathways **(Table 3.2)**, indicating broad and complex dysregulation of cholesterol homeostasis.

Our hypothesis that impaired cholesterol metabolism in aged macrophages contributes to AMD pathogenesis is consistent with numerous epidemiological studies that have established that parameters related to lipid status, such as baseline high-density lipoprotein-cholesterol (HDL-C) and total serum cholesterol, affect risk of AMD development and progression (Burgess and Davey Smith, 2017; Tomany et al., 2004; Yip et al., 2015). Moreover, one past genome-wide association study reported that polymorphisms in lipid-related genes such as LIPC, ABCA1, and CETP are associated with advanced AMD (Neale et al., 2010). These findings have led to the hypothesis that statins, cholesterol-lowering drugs used for cardiovascular disease, may affect

69

the development or progression of AMD (Hall et al., 2001). The findings of one non-randomized study suggest that high-dose statins may indeed reduce some high-risk features of AMD (Vavvas et al., 2016), although large randomized studies are necessary to confirm these findings (Apte, 2016) given that numerous other studies report conflicting results (Gehlbach et al., 2016). Cumulatively, these conflicting findings highlight that the relationship between aging, impaired cholesterol homeostasis, and AMD is complex and warrants further investigation.

In this study, we found that in aged murine macrophages, a transcriptomic profile suggesting impaired cholesterol homeostasis was associated with aberrant intracellular oxysterol levels, especially when the macrophages were treated with oxLDL. In many immune cells, oxysterols can directly regulate liver X receptor (LXR) transcriptional activity, which can modulate cellular lipid metabolism and the immune response, especially in inflammation-associated diseases (Spann and Glass, 2013). For example, 27-HC, the most prevalent oxysterol in atherosclerotic lesions, has been shown to promote atherosclerosis by inducing inflammation (Umetani et al., 2014). Therefore, in addition to being a surrogate marker for impaired cholesterol homeostasis, altered oxysterol production may itself play a pathogenic role in promoting cholesterol dysregulation. We found that, similar to murine macrophages, human PBMC and plasma samples also demonstrated age-dependent changes in oxysterols. Although the directionality of these age- and disease-associated changes did not correspond perfectly, our data suggest that broad dysregulation of cholesterol homeostasis in both aging and disease is associated with altered oxysterol signatures.

These findings build on recent reports that monocytes isolated from patients with neovascular AMD exhibit an altered immune-related transcriptomic signature (Grunin et al., 2016) and that these cells, when activated into macrophages, demonstrate proangiogenic

characteristics that may contribute to disease pathogenesis (Hagbi-Levi et al., 2017). Past studies have also shown that in the outer retina, accumulation of cholesterol oxidation products such as 7-KC can disrupt the immune environment and transform resident macrophages into disease-promoting cells (Indaram et al., 2015). Specifically, uptake of 7-KC in microglial cells results in decreased production of neurotrophic growth factors and increased expression of angiogenic mediators that promote pathologic CNV (Indaram et al., 2015).

How to distinguish whether changes in oxysterol signatures define aging, disease, or both is of great interest, as defects in lipid metabolism are a shared feature of multiple diseases. As an example, certain oxysterols and their metabolites have been shown to be specific biomarkers for Niemann-Pick type C (NPC) disease, an inherited lysosomal storage disease (Jiang et al., 2016; Porter et al., 2010). In this study, we found that after controlling for age and gender, plasma 24-HC was significantly associated with AMD. Despite our modest sample size (N = 107), these findings suggest that 24-HC is a strong candidate for an oxysterol that distinguishes AMD from physiologic aging. Our subanalysis revealed that plasma 24-HC remained highly associated with AMD even after controlling for total plasma cholesterol, highlighting its diagnostic value. Larger prospective studies are necessary to validate these findings and identify additional markers of risk.

Cumulatively, our findings highlight that impaired cholesterol homeostasis is a key pathway perturbed in aged macrophages and that oxysterol signatures in patient samples can distinguish AMD from physiologic aging. Ultimately, these findings may not only improve our ability to diagnose disease but also identify novel targets in cholesterol homeostasis that may be targeted in novel therapeutic approaches.

71

3.5   Methods

Animals. All animal experiments were approved by the Institutional Animal Care and Use Committee (IACUC) and performed in accordance with the Washington University School of Medicine Animal Care and Use guidelines. We obtained old (i.e., ~18-month-old), female wild-type C57BL/6J mice from the National Institute on Aging (Bethesda, MD) and compared them to strain-matched young (i.e., ~3-month-old), female wild-type C57BL/6J controls. We harvested peritoneal macrophages five days after elicitation with a 2-ml intraperitoneal injection of 4% thioglycollate broth (Sigma-Aldrich, St. Louis, MO). We harvested splenic macrophages by performing positive magnetic cell separation with the PE selection kit (Stem Cell Technologies) and PE anti-F4/80 monoclonal antibody (clone: BM8; eBioscience, Waltham, MA), following manufacturer's instructions. We cultured peritoneal and splenic macrophages in Gibco^{TM} RPMI 1640 medium (Thermo Fisher Scientific, Waltham, MA) supplemented with 10% fetal bovine serum (FBS; Atlanta Biologicals, Flowery Branch, GA) and 1% penicillin-streptomycin (Thermo Fisher Scientific). When indicated, we treated macrophages with 25 or 50 µg/ml of oxidized LDL (oxLDL; Alfa Aesar, Haverhill, MA) for 24 hours prior to further analysis.

OCR measurements. To perform metabolic characterization, we measured the oxygen consumption rate (OCR) of peritoneal macrophages as a surrogate marker for oxidative respiration with the XF96 Extracellular Flux Analyzer (Seahorse Bioscience, North Billerica, MA). In short, we plated peritoneal macrophages in Seahorse XF96 cell culture microplates

(Seahorse Bioscience) at 100,000 cells per well. On the morning of the experiment, we washed the cells and replaced the media with Seahorse assay media (Seahorse Bioscience) supplemented with 25 mM glucose (Sigma-Aldrich, St. Louis, MO) and 1 mM sodium pyruvate (Thermo Fisher Scientific) and adjusted the pH to 7.4. After incubation in a non-CO_2 incubator at 37°C for 1 hour, we measured OCR at baseline and after sequential treatment with the following chemicals from the Mito Stress Test Kit (Seahorse Bioscience): 3 μM oligomycin, 5 μM carbonyl cyanide 4-(trifluoromethoxy) phenylhydrazone (FCCP), and 1 μM rotenone/antimycin A (rot/AA). Each cycle consisted of 2 minutes of mixing and a 1-minute pause, followed by a 5-minute measurement period; we repeated each cycle 3-4 times. We normalized the background for all measurements by subtracting the average OCR of each sample after treatment with rot/AA.

Gene expression analysis. We extracted total RNA from peritoneal macrophages with the RNeasy Mini Kit (Qiagen) and prepared cDNA with the High-Capacity Reverse Transcription Kit (Applied Biosystems), following manufacturer's instructions. We performed quantitative PCR amplification of cDNA using either the TaqMan® probe-based gene expression assay for *p16INK4a* (Mm00494449_m1; Applied Biosystems) or custom TaqMan® Array Plates (Applied Biosystems) for lipid-related genes. In all cases, we used the ΔΔCT method, normalizing to *Actb*, *18sRNA*, *Gapdh*, or the geometric mean of a combination of these endogenous controls.

Transcriptome expression profiling. We isolated total RNA from peritoneal macrophages with the mirVana Kit (Ambion), performed cDNA amplification with the Ovation® Pico Kit

73

(NuGEN, San Carlos, CA), and performed target labeling with the Encore® Biotin Kit (NuGEN), according to manufacturer's instructions. We then performed whole transcriptome profiling of young and aged peritoneal macrophages using Mouse Gene (MoGene) 1.0 ST arrays processed with Affymetrix Expression Console (v1.3.1.187) at standard settings (RMA background correction, median polish summarization, and quantile normalization) to generate intensity values. We assigned each probeset of the MoGene 1.0 array a detection call of 'mean + 2×SD' of the negative controls. We performed data quality control to identify potential outliers by principal component analysis (PCA) plot and hierarchical clustering, as well as by quality control (QC) metrics (all probeset RLE means > 0.25) in Expression Console. From this QC, we omitted one sample in the young peritoneal group. We then filtered data by probeset type ("main" in MoGene 1.0) and by detection call (any probesets without a 'detected' call in any of the samples were removed). Any probeset without a gene symbol in the MoGene 1.0 data was also removed. 18,066 MoGene 1.0 probesets (from the total of 35,556) were kept for further analysis. We analyzed the data using the R package "limma" and generated gene lists based on P-values and false detection rate (FDR) q-values. We performed gene ontology (GO), pathway map, and interactome analyses with MetaCore[TM] (Clarivate Analytics, Philadelphia, PA).

Flow cytometry. We plated peritoneal macrophages on untreated Petri dishes and allowed them to adhere overnight. The next morning, we lifted cells by incubating for 5 minutes in ice-cold Dulbecco's phosphate-buffered saline (DPBS; Thermo Fisher Scientific) without calcium or magnesium and scraping gently. We next filtered cells through a 40 μm cell strainer, washed them with DPBS, and resuspended them in DPBS containing 5% FBS, 10 mM HEPES, 1 mM EDTA, and TruStain fcX[TM] antibody (BioLegend, San Diego, CA). We stained 10^5 to 10^6 cells

74

with APC anti-mouse CD36 (clone: HM36; BioLegend), PE/Cy7 anti-mouse CD64 (clone: X54-5/7.1; BioLegend), and PE anti-mouse F4/80 (clone: BM8; eBioscience) antibodies for 20 minutes on ice. We then washed and resuspended cells in DPBS and acquired data on a BD X-20 or BD LSR II flow cytometer (BD Biosciences, San Jose, CA). We analyzed and visualized data with FlowJo v10.

Human subjects. This study was approved by the Human Research Protection Office of Washington University School of Medicine and adhered to the Declaration of Helsinki. We obtained informed consent from all subjects prior to blood collection. To purify peripheral blood mononuclear cells (PBMCs) and plasma, we performed density gradient centrifugation with BD Vacutainer CPT^{TM} Cell Preparation Tubes (Franklin Lakes, NJ), following manufacturer's instructions. We classified patients as no AMD, early AMD, or wet AMD based on established clinical criteria (Ferris et al., 2005). Early AMD patients had either moderate drusen (>63 μm) or pigment changes in at least one eye but no CNV or GA in either eye at the time of sample collection. Wet AMD patients had CNV in at least one eye at the time of sample collection. We stored all samples at -80°C until further analysis. To determine the appropriate sample size, we performed an a priori power analysis with G*Power 3.1 (Faul et al., 2007). Estimating an effect size d of 0.6 based on pilot experiments, we calculated that we needed 94 subjects with an allocation ratio of 1.5:1 to detect a significant difference between the groups at the two-sided α = 0.05 level with 80% power. For the subanalysis, we performed chart review to identify the closest total plasma cholesterol measurement obtained within 3.5 years of the date of sample collection.

Oxysterol profiling by LC-MS/MS. We extracted and quantified oxysterol levels from murine peritoneal macrophage pellets, the supernatant of murine peritoneal macrophages, human PBMC cell pellets, and human plasma samples as previously described (Jiang et al., 2011). Briefly, we added deuterated oxysterols to the samples as internal standards and then extracted oxysterols with methanol. We derivatized the extracted oxysterols and their internal standards with N,N-dimethylglycinate (DMG) to increase MS sensitivity. We performed oxysterol analysis with a Shimadzu 20AD HPLC system (Kyoto, Japan) and a LeapPAL autosampler coupled to a tandem mass spectrometer (API 4000; Applied Biosystems) operated in MRM mode. We used positive ion ESI mode for detection of the derivatized oxysterols, injecting study samples in duplicate for data averaging. We conducted data processing with Analyst 1.5.1 (Applied Biosystems) and determined relative levels of each oxysterol by comparing its measurement with that of its corresponding deuterated internal standard. We normalized the murine macrophage oxysterol levels to cell number, murine supernatant levels to volume, human PBMC oxysterol levels to protein content, and human plasma oxysterol levels to volume. To normalize human samples processed on different days, we used one of the patient samples as an internal control.

Statistics. We performed statistical analysis as indicated in the figure legends with Prism 5 (GraphPad Software) or SPSS Statistics Version 23 (IBM, Armonk, NY). We assessed the normality of our data graphically and with the Kolmogorov-Smirnov test and used appropriate non-parametric alternatives when necessary. We considered $P < 0.05$ to be statistically significant. To model the relationship between PBMC and plasma oxysterol signatures and AMD, we generated binary logistic regression models. Our model included the following predictor variables: age at the time of sample collection, gender, and PBMC/plasma oxysterol

levels. For the subanalysis, we generated an additional binary logistic regression model, which included the following predictor variables: age at time of sample collection, gender, plasma 24-HC levels, and total plasma cholesterol. For all regression models, we assessed fit with the Hosmer-Lemeshow lack-of-fit test and performed diagnostics by examining Cook's distances, leverages, and residual deviances. The final reported models had six omitted cases based on sensitivity analysis. We checked for problems with collinearity by examining variance inflation factors (VIF). We used an unadjusted α of 0.05 for the binary logistic regression.

3.6   Acknowledgements

Medicine for help with genomic analysis (NIH Grants P30 CA91842 and UL1 TR000448). We also thank David Scherrer for technical assistance and Stephanie Schultz for helpful discussions.
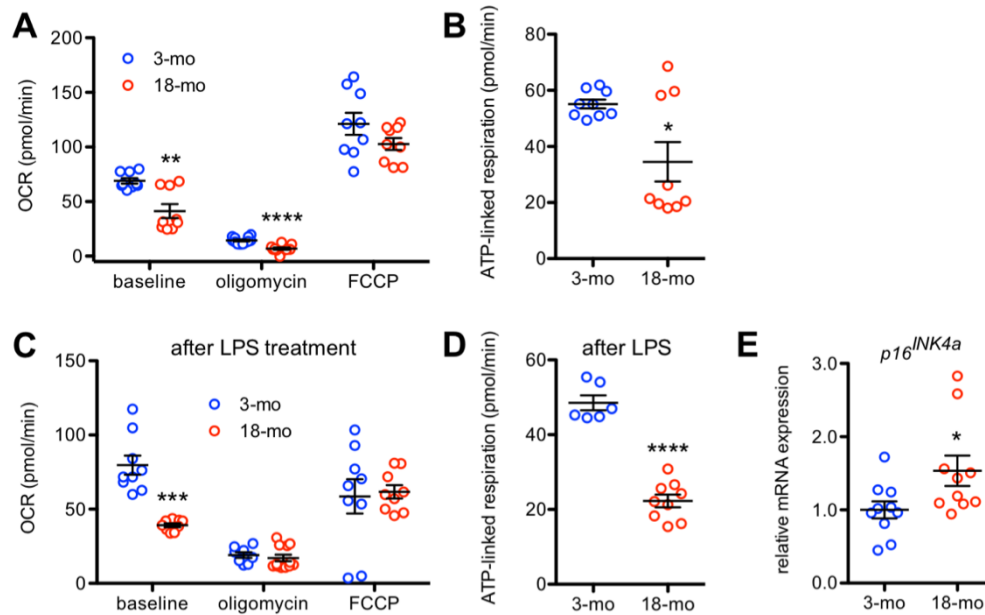
Figure 3.1. Peritoneal macrophages from old mice exhibit quantifiable signs of aging. (A) Aged peritoneal macrophages had reduced oxygen consumption rate (OCR) both at baseline (N = 9/group; 2-tailed, unpaired Welch's t-test) and in response to oligomycin (N = 11-12/group; 2-tailed, unpaired t-test) and significantly reduced ATP-linked respiration (B; N = 9/group; 2-tailed, unpaired Welch's t-test). (C) Lipopolysaccharide (LPS)-treated aged peritoneal macrophages also had impaired mitochondrial bioenergetics at baseline (N = 8-12/group; 2-tailed, unpaired Welch's t-test) and significantly reduced ATP-linked respiration (D; N = 6-9/group; 2-tailed, unpaired t-test) compared to LPS-treated young peritoneal macrophages. (E) Aged peritoneal macrophages had increased mRNA expression of the senescence marker $p16^{INK4a}$ (N = 10/group; 2-tailed, unpaired t-test). Open circles depict individual data points; horizontal lines depict mean ± SEM (A-E) (* $P < 0.05$; ** $P < 0.01$; *** $P < 0.001$; **** $P < 0.0001$).
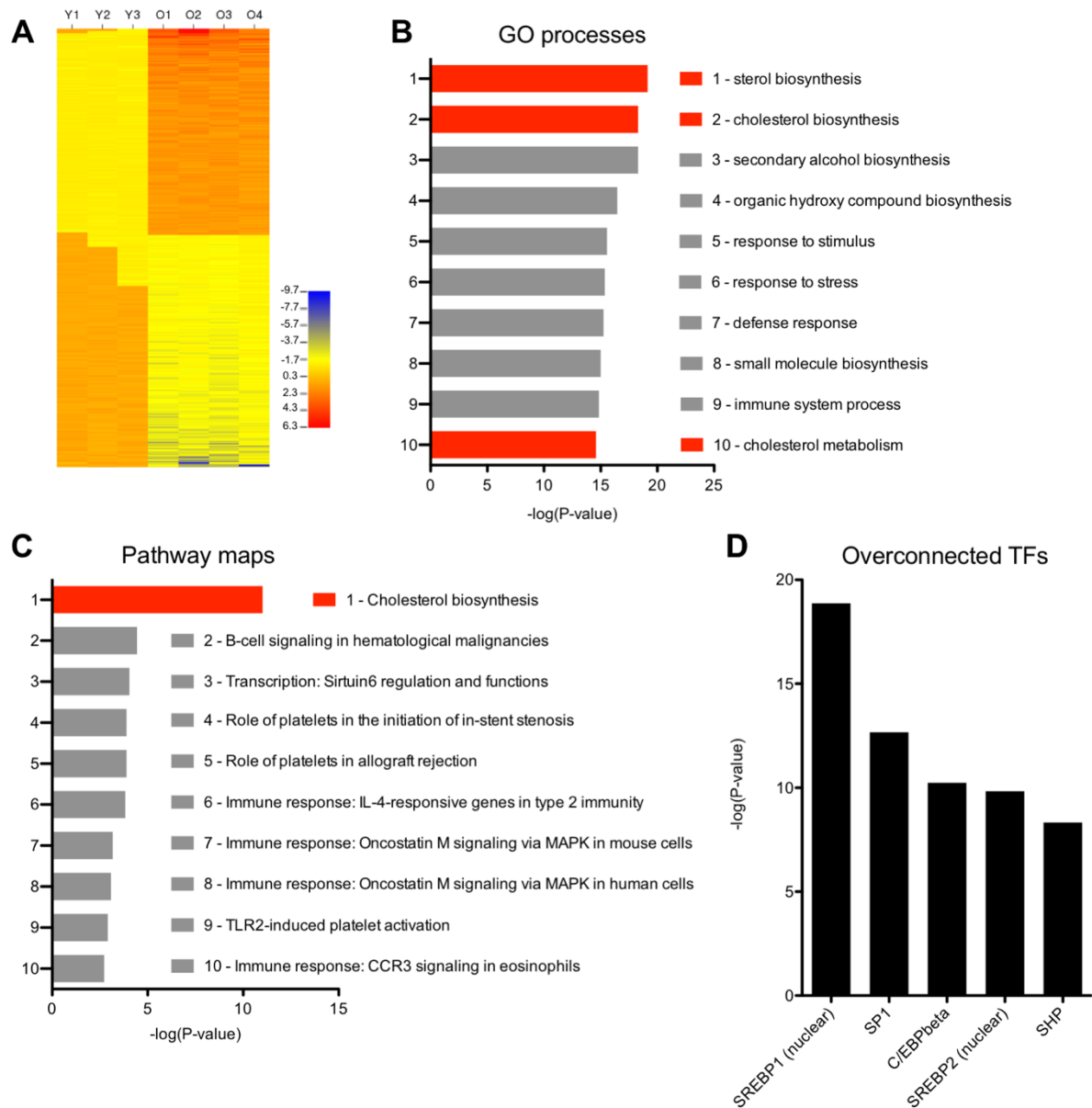
Figure 3.2. Transcriptomic profiling of aged peritoneal macrophages. (A) Aged peritoneal macrophages display numerous transcriptomic changes, which suggest perturbations in various gene ontology (GO) processes (B) and pathway maps (C). (D) Interactome analysis revealed numerous overconnected transcription factors (TFs) whose known gene targets were overrepresented in the genes we identified as dysregulated in aged versus young macrophages.

80
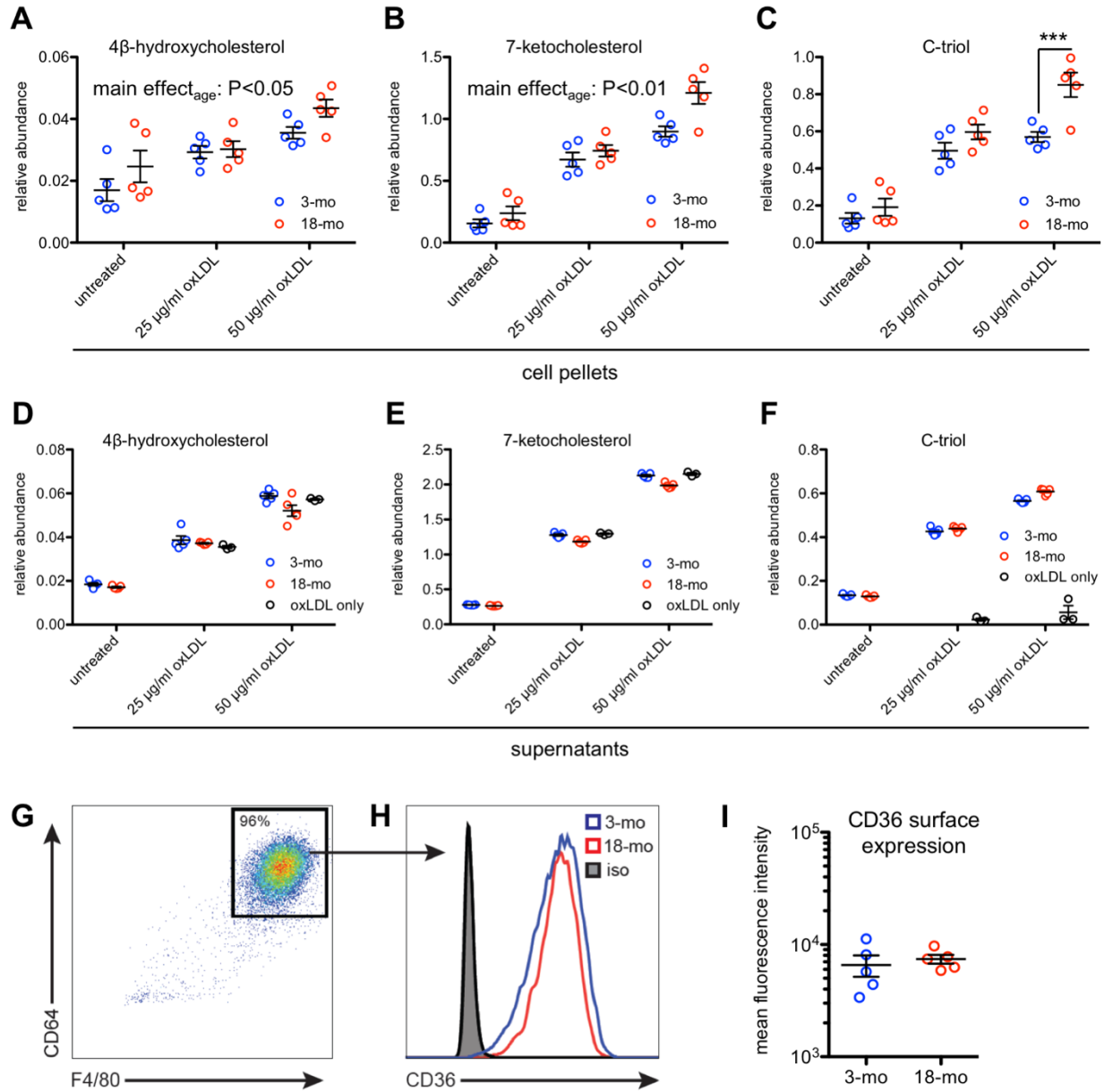
Figure 3.3. Aged peritoneal macrophages have abnormal oxysterol content. (A-C) Aged peritoneal macrophages contained significantly more intracellular 4β-hydroxycholesterol (4β-HC) and 7-ketocholesterol (7-KC) than their young counterparts at baseline and after treatment with 25 or 50 μg/ml oxidized LDL (oxLDL) (N = 5/group; 2-way ANOVA) and significantly more intracellular cholestane-3β,5α,6β-triol (C-triol) after treatment with 50 μg/ml oxLDL (N = 5/group; 2-way ANOVA with Bonferroni post-hoc test). (D-F) Although some comparisons were statistically significant due to low within-group variance, the supernatant of young and aged peritoneal macrophages contained qualitatively similar levels of 4β-HC, 7-KC, and C-triol both at baseline and after treatment with oxLDL (N = 5/group; 2-way ANOVA with Bonferroni post-hoc test). (G) Representative flow cytometry plot from young and aged peritoneal macrophages showing gating on macrophage markers CD64 and F4/80. (H-I) Young and aged peritoneal macrophages exhibited similar CD36 surface expression. Isotype staining (iso) was identical between groups (N = 5/group; 2-tailed, unpaired t-test). Open circles depict individual data points; horizontal lines depict mean ± SEM (A-F, I) (*** $P < 0.001$).
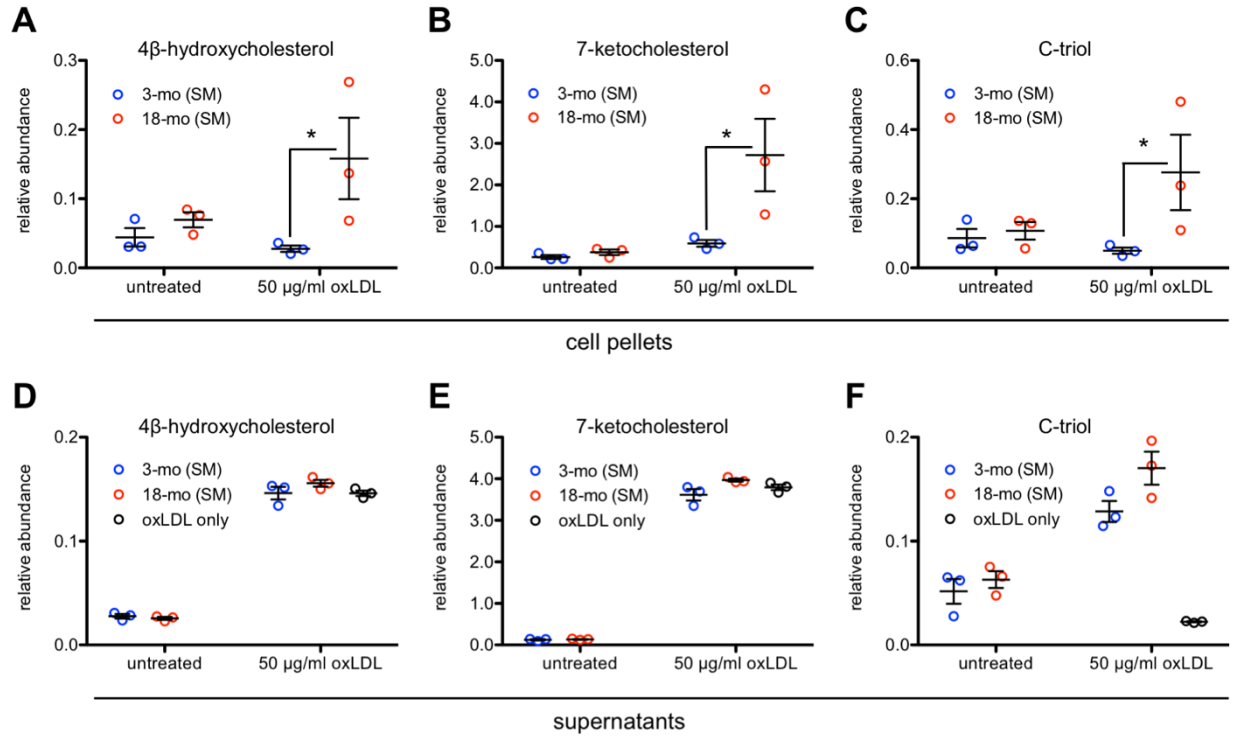
Figure 3.4. Aged splenic macrophages (SM) have abnormal oxysterol content. (A-C) Aged SM contained significantly more intracellular 4β-hydroxycholesterol (4β-HC), 7-ketocholesterol (7-KC), and cholestane-3β,5α,6β-triol (C-triol) compared to their young counterparts after treatment with 50 μg/ml oxidized LDL (oxLDL) (N = 3/group; 1-tailed Mann-Whitney U test). (D-F) The supernatant of young and aged SM contained similar levels of 4β-HC, 7-KC, and C-triol both at baseline and after treatment with oxLDL (N = 3/group; 2-tailed Mann-Whitney U test). Open circles depict individual data points; horizontal lines depict mean ± S.E.M. (A-F) (* P < 0.05).
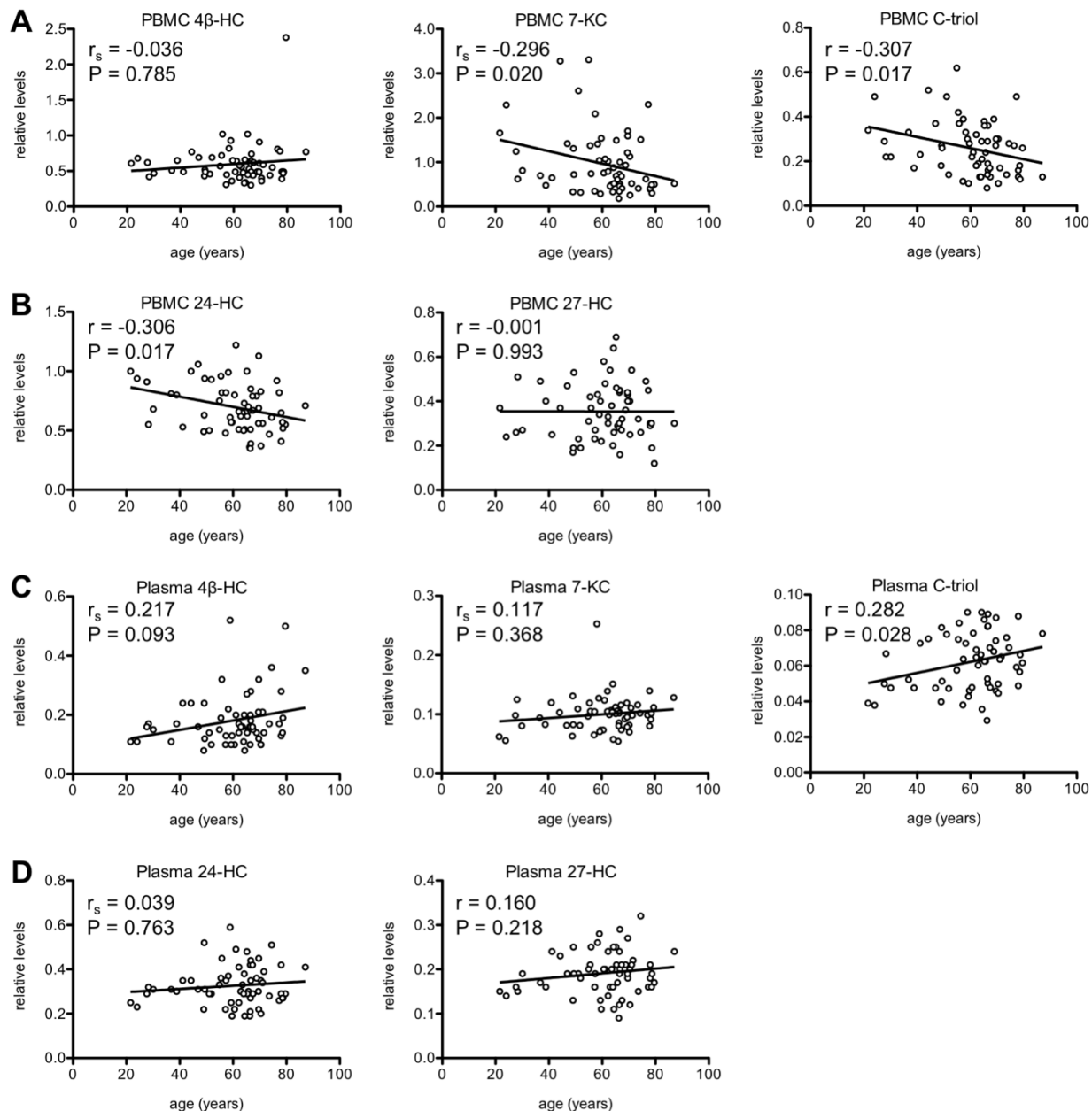
Figure 3.5. Age affects human peripheral blood mononuclear cell (PBMC) and plasma oxysterol signatures. (A-B) There was a significant negative correlation between age and PBMC 7-KC levels, PBMC C-triol levels, and PBMC 24-HC levels in healthy human subjects. (C-D) There was a significant positive correlation between age and plasma C-triol levels and a trend towards a positive correlation between age and plasma 4β-HC levels. Open circles depict individual data points; lines depict the best-fitting linear regression line (A-D; r = Pearson product-moment correlation coefficient; r_s = Spearman rank-order correlation coefficient).
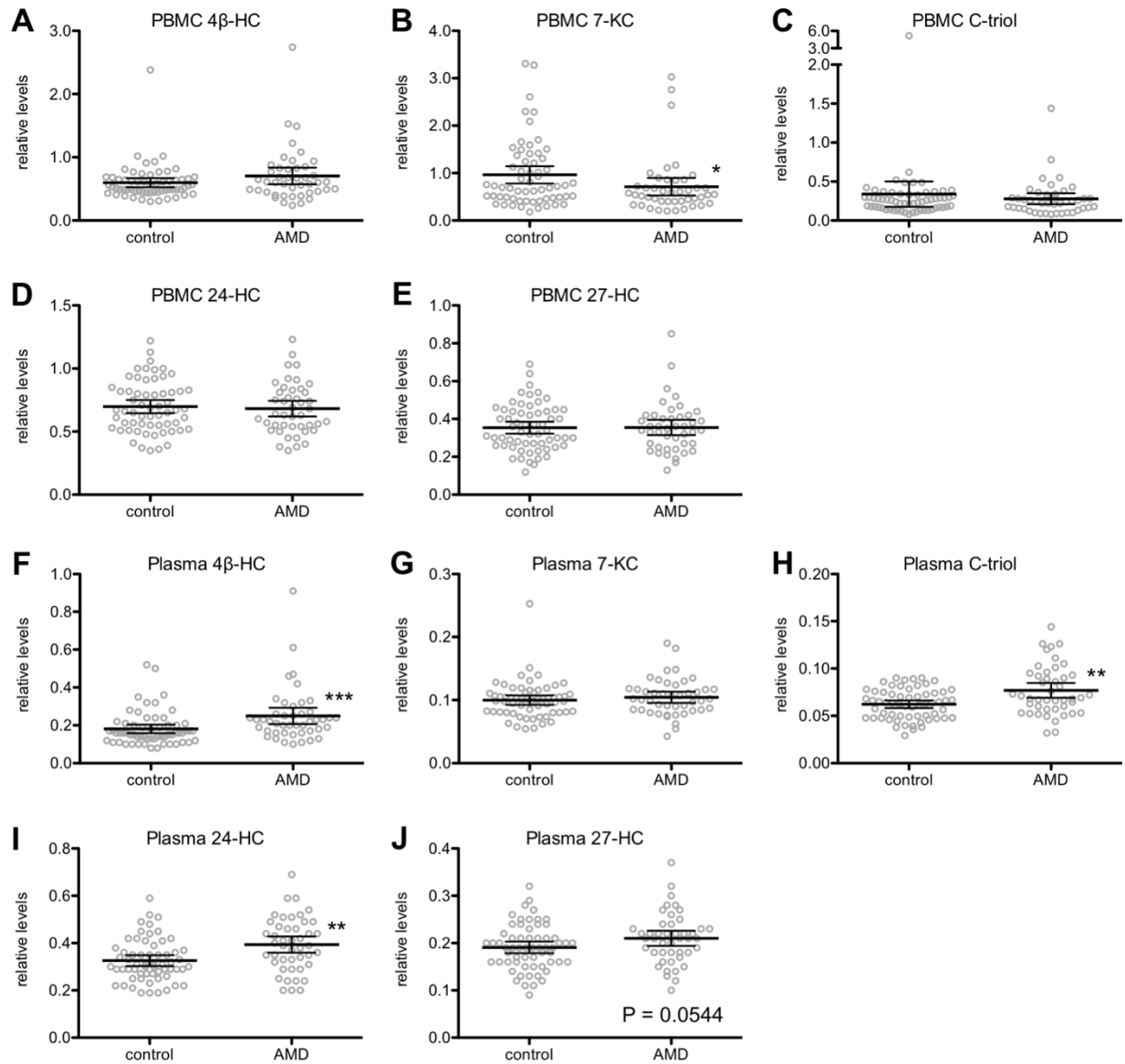
Figure 3.6. Age-related macular degeneration (AMD) patients have altered peripheral blood mononuclear cell (PBMC) and plasma oxysterol signatures. (A-J) We measured PBMC and plasma levels of 4β-HC, 7-KC, C-triol, 24-HC, and 27-HC. AMD patients (N = 44-45) had decreased PBMC 7-KC levels (B; 2-tailed Mann-Whitney U test), elevated plasma 4β-HC levels (F; 2-tailed Mann-Whitney U test), elevated plasma C-triol levels (H; 2-tailed Mann-Whitney U test), elevated plasma 24-HC levels (I; 2-tailed Mann-Whitney U test), and a trend towards elevated plasma 27-HC levels (J; 2-tailed, unpaired t-test) compared to non-AMD controls (N = 61). Open circles depict individual data points; horizontal lines depict mean ± 95% confidence intervals (A-J) (* P < 0.05; ** P < 0.01; *** P < 0.001).
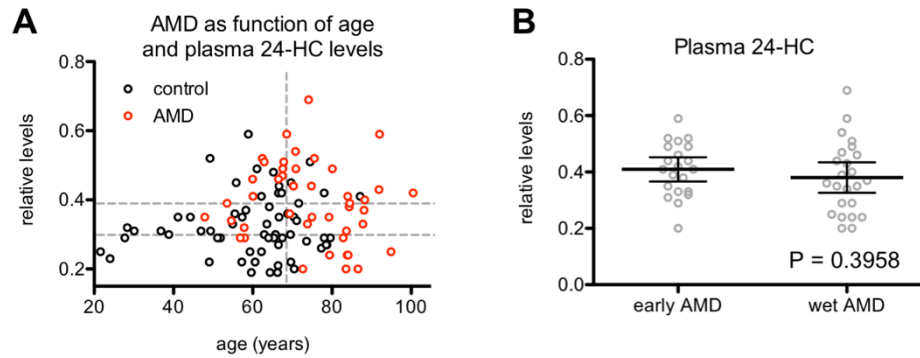
Figure 3.7. Plasma 24-HC levels discriminate age-related macular degeneration (AMD) from physiologic aging. (A) We divided patients into tertiles by plasma 24-HC and by age (i.e., above versus below median age) and found that individuals in the highest tertile of plasma 24-HC who were also above median age (top right) had the highest AMD prevalence. Horizontal dashed grey lines demarcate plasma 24-HC tertiles; the vertical dashed grey line indicates the median age. (B) We did not observe a statistically significant difference in plasma 24-HC levels in early AMD patients versus advanced neovascular (wet) AMD patients (N = 21 early AMD; 24 wet AMD; 2-tailed, unpaired t-test). Open circles depict individual data points (A-B); horizontal lines depict mean ± 95% confidence intervals (B).

Table 3.1. Top ten up- and down-regulated genes in aged versus young peritoneal macrophages.

Probeset ID	Gene symbol	Fold change[a]	P-value	FDR
10463355	*Scd2*	-3.645	.0007	.0667
10506571	*Dhcr24*	-2.522	.0001	.0361
10347748	*Acsl3*	-2.406	.0003	.0497
10560702	*Ceacam19*	-2.266	<.0001	.0307
10403413	*Idi1*	-2.070	.0018	.0952
10544273	*Clec5a*	-1.996	.0006	.0634
10482762	*Idi1*	-1.977	.0021	.1006
10420668	*Mir15a*	-1.969	.0016	.0924
10424349	*Sqle*	-1.969	<.0001	.0115
10527920	*Cyp51*	-1.967	.0012	.0851
10582879	*Csprs*	3.771	<.0001	.0258
10538126	*Gimap4*	4.368	.0052	.1382
10551025	*Cd79a*	6.435	.0018	.0957
10429520	*Ly6d*	6.483	.0028	.1104
10466172	*Ms4a1*	7.480	.0025	.1050
10392142	*Cd79b*	7.764	.0004	.0552
10458278	*Mzb1*	9.573	.0002	.0469
10523359	*Cxcl13*	11.166	.0015	.0918
10531724	*Plac8*	11.549	.0006	.0634
10429564	*Ly6a*	12.571	<.0001	.0306

[a]Aged versus young peritoneal macrophages (negative fold-change reflects decreased expression in aged macrophages relative to young macrophages.

Table 3.2. Expression profiling of lipid-related genes in aged and young macrophages.

Cellular function	Gene symbol	Fold change[a]	P-value[b]
Biosynthesis	*Fads2*	-1.545	.050
	Fads3	1.299	.050
	Fdft1	-3.831	.050
	Fdps	-1.885	.050
	Hmgcs2	3.122	.050
	Prkaa2	2.773	.046
	Scd1	-1.895	.050
Elimination	*Cyp11a1*	-9.342	.050
	Cyp7b1	2.515	.046
	Cyp27a1	-1.473	.050
	Hadhb	-1.984	.050
	Lpl	1.496	.050
	Tbxas1	1.249	.050
Leukotriene signaling	*Lta4h*	-1.314	.050
	Alox5ap	-1.919	.050
Transport	*Apoa1*	-6.985	.046
	Apof	-6.089	.050
	Slc16a6	-1.459	.050
	Slc27a1	-1.659	.050
	Slc27a3	-4.402	.050
	Stard4	-1.306	.050
Uptake	*Cxcl16*	-1.927	.050
	Olr1	-2.340	.050
	Pcsk9	-1.903	.050
	Stab2	-3.008	.046
Other or multiple functions	*Adfp*	2.102	.050
	Alox15	5.797	.050
	Fabp4	1.338	.050
	Nr0b2	-3.911	.037
	Nr1h3	-1.561	.050

[a]Aged versus young peritoneal macrophages (negative fold-change reflects decreased expression in aged macrophages relative to young macrophages);
[b]Significant by 2-tailed Mann-Whitney U test.

87

Table 3.3. Demographic and clinical characteristics of human subjects.

Demographic parameter	Control	AMD	P-value
Age, median (range)	64.09 (21.59-87.07)	74.11 (47.87-100.50)	<.0001[a]
Sex, N			
Male	37	23	.3781[b]
Female	25	22	
AMD status, N			
No AMD	62	0	N/A
Early AMD	0	21	
Advanced neovascular AMD	0	24	

[a]Significant by 2-tailed Mann-Whitney U test; [b]Non-significant by X^2 test.

88

Table 3.4. Beta coefficients from PBMC binary logistic regression model.

Predictor variable	aOR (e^β)	95% CI of e^β	P-value
Age	1.103	1.049 to 1.161	<.001
Female gender	.893	.335 to 2.381	.821
PBMC 7-KC levels, 1-unit	.351	.087 to 1.412	.140

89

Table 3.5. Beta coefficients from plasma binary logistic regression model.

Predictor variable	aOR (e^β)	95% CI of e^β	P-value
Age	1.113	1.055 to 1.174	<.001
Female gender	.390	.119 to 1.282	.121
Plasma 24-HC levels, .1-unit	3.104	1.66 to 5.79	<.001

Table 3.6. AMD as a function of age and plasma 24-HC levels.

		Age		
		Below median	**Above median**	**Total**
Plasma 24-HC	**Lowest tertile**	2/19 (10.5%)	8/17 (47.1%)	10/36 (27.8%)
	Middle tertile	4/21 (19.0%)	10/15 (66.7%)	14/36 (38.9%)
	Highest tertile	5/13 (38.5%)	16/21 (76.2%)	21/34 (61.8%)
	Total	11/53 (20.8%)	34/53 (64.2%)	45/106 (42.5%)

91

Chapter 4:

Macrophage microRNA-150 Promotes Pathological Angiogenesis as seen in Age-Related Macular Degeneration

This chapter is adapted from a manuscript published in *JCI Insight*.

Conceptualization: R.S.A., Jonathan B. Lin, A.S.
Investigation: Jonathan B. Lin, H.V.M., A.S., R.S., P.K., Joseph B. Lin, Z.D., N.B.
Writing – Original Draft: Jonathan B. Lin
Writing – Review & Editing: Jonathan B. Lin, R.S.A., D.S.O., A.S., H.V.M., Joseph B. Lin
Supervision: R.S.A., D.S.O.
Funding Acquisition: R.S.A., D.S.O., Jonathan B. Lin

4.1   Summary

Macrophage aging is pathogenic in diseases of the elderly, including age-related macular degeneration (AMD), a leading cause of blindness in older adults. However, the role of microRNAs, which modulate immune processes, in regulating macrophage dysfunction and thereby promoting age-associated diseases is underexplored. Here, we report that microRNA-150 coordinates transcriptomic changes in aged murine macrophages, especially those associated with aberrant lipid trafficking and metabolism in AMD pathogenesis. Molecular profiling confirmed that aged murine macrophages exhibit dysregulated ceramide and phospholipid profiles compared to young macrophages. Of translational relevance, upregulation of microRNA-150 in human peripheral blood mononuclear cells was also significantly associated with increased odds of AMD, even after controlling for age. Mechanistically, microRNA-150 directly targets stearoyl-CoA desaturase-2, which coordinates macrophage-mediated inflammation and pathologic angiogenesis, as seen in AMD, in a vascular endothelial growth factor (VEGF)-independent manner. Together, our results implicate microRNA-150 as pathogenic in AMD and provide novel molecular insights into diseases of aging.

4.2 Introduction

Macrophages are critical effector cells of the innate immune system. Multiple groups, including our own, have reported that macrophages from aged mice demonstrate a functional drift compared to those isolated from young mice. For example, aged macrophages exhibit epigenomic changes, leading to reduced autophagic capacity (Khalil et al., 2016), and are defective in their ability to fight viral infections due to reduced phagocytic activity (Wong et al., 2017). Moreover, aged macrophages are skewed towards a proangiogenic gene and cytokine expression profile, which leads to dysregulated inflammation and inability to inhibit pathological angiogenesis (Kelly et al., 2007). Aged macrophages also exhibit impaired cholesterol efflux due to decreased *Abca1* expression, leading to intracellular cholesterol accumulation and pathologic vascular proliferation (Sene et al., 2013). Age-associated macrophage dysfunction has been proposed to contribute to the pathogenesis of numerous diseases of aging, including age-related macular degeneration (AMD) and atherosclerosis (Sene and Apte, 2014). In addition, age-associated changes in microglia, the major resident immune cell in the retina with similar phagocytic functions, may also promote AMD (Ma and Wong, 2016).

AMD is a leading cause of blindness in industrialized nations (van Leeuwen et al., 2003) and displays a complex disease course characterized, initially, by accumulation of cholesterol-rich deposits known as drusen underneath the retina (Sene and Apte, 2014; Sene et al., 2015). Though drusen themselves do not typically cause vision loss, they are a risk factor for progression to one of two forms of advanced AMD: advanced neovascular (wet) AMD, characterized by pathologic subretinal angiogenesis, or advanced dry AMD, characterized by geographic atrophy secondary to loss of retinal neurons and underlying cells. Both forms of advanced AMD can cause debilitating blindness, though wet AMD is responsible for a

94

significant portion of the vision loss associated with AMD (Ferris et al., 1984). While anti-vascular endothelial growth factor (VEGF) therapies have revolutionized treatment options for wet AMD, an important subset of patients is un- or under-responsive to these therapies (Sene et al., 2015). Of interest, genome-wide association studies show that polymorphisms in lipid-related genes, including hepatic lipase (LIPC), ATP-binding cassette transporter member 1 (ABCA1), and cholesterol ester transfer protein (CETP), are associated with advanced AMD (Neale et al., 2010), supporting the idea that impaired cholesterol homeostasis contributes to AMD pathogenesis.

Impaired cholesterol homeostasis also contributes to the pathogenesis of atherosclerosis. Atherosclerotic plaque formation begins when circulating monocytes adhere to the vascular endothelium, migrate to the sub-endothelial space, and differentiate into macrophages that take up lipids and become foam cells (Gerrity, 1981; Gerrity et al., 1979). Past studies have demonstrated that the activation/polarization state of macrophages is important for predicting plaque phenotype and stability (Chinetti-Gbaguidi et al., 2015; Peled and Fisher, 2014). For example, in patients with hypercholesterolemia, macrophages polarize to a more proinflammatory state, which could predispose to plaque formation (Fadini et al., 2014). Moreover, macrophage cholesterol efflux capacity in human patients is a clinically relevant predictor of atherosclerotic coronary artery disease (Ishikawa et al., 2015), suggesting that perturbations in cholesterol homeostasis promote disease. Remarkably, atherosclerotic plaques and drusen have similar lipid compositions (Crabb et al., 2002; Curcio et al., 2009; Kramsch et al., 1971; Mullins et al., 2000), unifying the pathogenic pathways underlying these diseases. Based on these similarities, some have proposed that it may be possible to repurpose statins,

95

lipid-lowering drugs used to treat atherosclerosis, for treating AMD (Apte, 2016; Vavvas et al., 2016), although not all studies have yielded the same conclusions (Gehlbach et al., 2016).

Despite these advances in our understanding of the phenotype of aged macrophages and how such changes contribute to age-associated diseases, the molecular mechanisms by which macrophages drift towards the disease-promoting phenotype remain poorly understood. Given the immense spectrum of these changes in aged macrophages, we hypothesized that microRNAs (miRs) may regulate the transcriptome of macrophages and thereby the transition of macrophages to a disease-promoting phenotype. The ability of miRs to target multiple genes makes them strong candidates as molecular regulators that skew macrophages towards a disease-promoting phenotype. Previous studies have examined the miR signatures of AMD by profiling eye fluids, such as human vitreous humor and plasma, providing phenotypic characterization, but have failed to provide mechanistic insights into the underlying disease etiology (Grassmann et al., 2014; Menard et al., 2016). Therefore, further elucidation of the target genes of these miRs, the affected cell types, and the molecular pathways involved is necessary for a more complete understanding of disease pathogenesis.

In this study, we sought to identify one or more miR(s) that regulate the disease-promoting programmatic changes in macrophages that are associated with AMD. Our results demonstrate that miR-150 is highly upregulated both in disease-promoting murine macrophages and in human peripheral blood mononuclear cells from AMD patients. Moreover, we show that miR-150 regulates macrophage-mediated inflammation and pathologic angiogenesis independently from vascular endothelial growth factor (VEGF) by targeting stearoyl-CoA desaturase-2 (*Scd2*), suggesting that it regulates the transition of macrophages from a healthy profile to the AMD-promoting phenotype. Ultimately, these findings provide insight into the

96

mechanisms underlying the pathological programmatic changes in aged macrophages and may lead to the identification of novel therapeutic targets and candidate biomarkers.

4.3   Results

Aged macrophages have distinct cholesterol-responsive microRNA networks

Since miRs can regulate numerous target genes, we hypothesized that miRs may globally regulate the macrophage's response to exogenous cholesterol. We first sought to identify cholesterol-responsive miRs by performing a microarray, comparing untreated macrophages versus macrophages treated with acetylated LDL (acLDL) or oxidized LDL (oxLDL). We previously showed that aged and young macrophages handle cholesterol differently and that aged macrophages demonstrate altered capacity to metabolize cholesterol (Sene et al., 2013). As such, we profiled aged and young macrophages separately to accurately capture the response of these cells to exogenous cholesterol. In young macrophages, ten miRs were similarly downregulated in response to both acLDL and oxLDL **(Figure 4.1A)**. In contrast, in aged macrophages, five miRs were similarly dysregulated in response to both acLDL and oxLDL, three downregulated and two upregulated **(Figure 4.1B)**. These findings suggest that in macrophages, miRs are altered after exposure to cholesterol and may indeed orchestrate the macrophage's response to cholesterol. Furthermore, these findings suggest that the distinct miR responses in aged versus young macrophages may underlie their distinct responses to exogenous cholesterol.

We hypothesized that in addition to these cholesterol-responsive miRs, there may be a separate network of miRs that regulate the broad spectrum of differences between disease-promoting, aged macrophages and young macrophages. Such miRs must not only demonstrate altered expression with aging but also have consistent dysregulation regardless of treatment with

97

cholesterol. Five miRs were upregulated in aged macrophages and maintained the same pattern of dysregulation in aged versus young macrophages after treatment with acLDL or oxLDL **(Figure 4.1C)**. MiR-150 was the strongest candidate for further study given that it had the highest fold change in aged versus young macrophages and since the others did not validate after further characterization.

miR-150 is upregulated in aged macrophages of diverse origins

To validate the microarray data, we performed quantitative real-time PCR (qPCR) with independent samples. Indeed, aged peritoneal macrophages (PMs) had nine-fold increased miR-150 expression at baseline compared to young PMs **(Figure 4.1D)**. To determine whether this phenomenon was lineage-specific, we also measured miR-150 expression in splenic macrophages (SMs) and bone marrow-derived macrophages (BMDMs). Similar to PMs, we found that aged SMs **(Figure 4.1E)** and BMDMs **(Figure 4.1F)** exhibited three-fold higher expression of miR-150 at baseline compared to young SMs and BMDMs. Next, we sought to confirm that miR-150 upregulation in aged macrophages is unaffected by exposure to exogenous cholesterol or lipopolysaccharide (LPS). Indeed, aged PMs treated with acLDL, oxLDL, or LPS exhibited higher miR-150 expression than similarly treated young PMs **(Figure 4.1G)**. Likewise, oxLDL- and LPS-treated aged BMDMs also had higher miR-150 expression compared to similarly treated young BMDMs **(Figure 4.1H)**. Cumulatively, these findings provide strong evidence that miR-150 upregulation may indeed skew macrophages towards the disease-promoting, aged phenotype.

miR-150 overexpression reprograms the macrophage transcriptome

We next sought to determine the mechanism by which miR-150 skews macrophages towards the aged phenotype. To elucidate the cellular processes and pathways regulated by miR-150, we performed RNA-Sequencing (RNA-Seq) to identify the transcriptomic networks dysregulated under conditions of miR-150 overexpression, comparing young macrophages transfected with miR-150 mimic (miR-150^{OE}) to young macrophages transfected with a non-targeting negative control mimic (NC). From RNA-Seq, we obtained an average of 35,607,314 reads per sample (N = 11), and of these, an average of 32,535,035 reads (91.4%) mapped to the mouse genome (Mus_musculus reference build Ensembl_R76). We performed hierarchical clustering, revealing clear differences between the transcriptomes of miR-150^{OE} and NC-transfected peritoneal macrophages **(Figure 4.2A)**.

To determine the subset of these miR-150-regulated genes that are also dysregulated in aged macrophages, we overlaid the RNA-Seq results onto the results of a previous microarray we performed comparing aged versus young macrophages (see Chapter 3). The intersection between these gene lists identifies genes dysregulated in aged murine macrophages that may be regulated by miR-150 upregulation. We identified 160 commonly dysregulated genes with a |fold change| > 1.2 both in miR-150^{OE} versus NC-transfected macrophages and in aged versus young macrophages. To determine whether these genes suggested abnormalities in specific pathways, which may provide insight into the mechanism by which miR-150 upregulation promotes age-associated disease, we performed pathway analysis with MetaCore for enrichment by gene ontology (GO) processes, process networks, and pathway maps **(Figures 4.2B, 4.2C, and 4.2D)**. Numerous diverse GO processes were enriched for, indicating that miR-150 regulates broad cellular pathways in macrophages **(Figure 4.2B)**. Of interest, inflammation and immune

response process networks were five of the nine most enriched process networks **(Figure 4.2C)**. These findings confirm that there is immune dysregulation in aged macrophages associated with miR-150 upregulation. Remarkably, aberrant lipid trafficking and metabolism in AMD was the third most enriched pathway map **(Figure 4.2D)**, validating our hypothesis that miR-150 regulates the transition of macrophages to the AMD-promoting phenotype.

Disease-promoting macrophages have altered phospholipid and ceramide profiles

In AMD, the interaction between dysregulated macrophage cholesterol homeostasis and aging is implicated in the pathophysiology of disease. To better understand this relationship, we performed lipidomics to determine whether aged macrophages have altered lipid profiles as possible consequences of aberrant lipid trafficking and metabolism. We focused on components of the plasma membrane, including ceramides and phospholipids, since the composition and organization of the plasma membrane have been shown to regulate macrophage function (Wei et al., 2016). Aged macrophages contained significantly more long-chain Cer(16:0) than young macrophages but similar levels of very long-chain Cer(22:0) and Cer(24:0) **(Figure 4.3A)**. Consistent with increased Cer(16:0), we observed a significant decrease in both the Cer(22:0)/Cer(16:0) and Cer(24:0)/Cer(16:0) ratios in aged versus young macrophages **(Figure 4.3B)**. These findings indicate that aged macrophages exhibit remodeling of their ceramide composition from very long-chain to long-chain species.

In the phosphatidylglycerol (PG) class, PG-D16:0-18:1 was the only detectable species, and there was no significant difference in content between aged and young macrophages **(Figure 4.3C)**. However, numerous individual species were detected for each of the other phospholipid classes. Overall, aged macrophages contained more total phosphatidylcholine (PC; **Figure 4.3D)**

100

and more total phosphatidylethanolamine (PE; **Figure 4.3E)** than young macrophages but similar total phosphatidylinositol (PI; **Figure 4.3F**) and similar total phosphatidylserine (PS; **Figure 4.3G)**. Further analysis of the individual species within each phospholipid class by 2-way, repeated-measures ANOVA revealed a significant interaction between the main effects of species identity and age for all four phospholipid classes **(Figures 4.3H, 4.3I, 4.3J, and 4.3K)**, indicating that the increased total PC and total PE in aged macrophages were driven by increases in specific species within these phospholipid classes. Post-hoc testing showed that the significantly increased species were generally phospholipids containing fatty acids with multiple double bonds, suggesting a shift toward unsaturated fatty acids **(Figures 4.3H, 4.3I, 4.3J, and 4.3K)**. Based on these findings, we propose that aberrant lipid trafficking and cholesterol metabolism in aged macrophages leads to this disruption in ceramide and phospholipid profiles, which may contribute to macrophage dysfunction in age-associated diseases.

miR-150 upregulation is associated with age-related macular degeneration in humans

To assess the translational relevance of these findings, we recruited human patients with early AMD or advanced neovascular (wet) AMD and non-AMD controls in a case-control study design. Demographic and clinical information of the participants are shown in **Table 4.1**. From these patients, we collected peripheral blood mononuclear cells (PBMCs), which contain monocytes, and quantified miR-150 copy number in these samples. On average, AMD patients had significantly higher PBMC miR-150 levels compared to control subjects **(Figure 4.4A)**. When we subdivided AMD patients into early AMD and wet AMD groups, we observed higher PBMC miR-150 levels in early AMD patients compared to controls and in wet AMD patients compared to controls **(Figure 4.4B)**. There was, however, no significant difference in PBMC

miR-150 levels between early and wet AMD patients **(Figure 4.4B)**. These findings suggest that increased PBMC miR-150 levels are associated with developing AMD but not with disease progression. We next sought to determine whether age affected PBMC miR-150 levels since AMD patients tended to be older than non-AMD controls **(Table 4.1)**. We found that there was no significant correlation between age and PBMC miR-150 levels in AMD patients (r_s = 0.1596, P = 0.3066) or in control subjects (r_s = -0.2002, P = 0.1157) **(Figure 4.4C)**, suggesting there is no significant association between PBMC miR-150 levels and age.

To model the relationship between PBMC miR-150 levels and AMD status and to rigorously control for a possible – albeit unlikely – effect of age, we generated a binary logistic regression model with the predictor variables of age, gender, and $\log_{10}$-transformed PBMC miR-150 levels and the outcome of AMD. The overall model was statistically significant (LR X^2 = 47.4, df = 3, P < 0.001) and had good fit (X^2 = 9.4, df = 8, P = 0.311). As expected, age was a significant predictor of AMD (P < 0.001) with a beta coefficient of 0.082, indicating that each additional year of age was associated with increased odds of having AMD (aOR = 1.086; 95% CI = 1.04 to 1.13). Of significant interest, even after controlling for the effects of age and gender on miR-150 levels, $\log_{10}$-transformed PBMC miR-150 levels were highly associated with AMD (P < 0.001) with a beta coefficient of 3.367, indicating that each additional 10-fold increase in PBMC miR-150 levels was associated with a 29.0-fold increased odds of having AMD (95% CI = 5.9 to 141.5). To determine the efficacy of PBMC miR-150 levels as a potential marker of AMD, we generated a receiver operating characteristic (ROC) curve and found that the area under the ROC curve (AUC) was 0.860 (95% CI = 0.788 to 0.933), indicating good discrimination.

Furthermore, we performed conjunctive analysis to illustrate the relationship between PBMC miR-150 levels, age, and the outcome of AMD. We divided patients into tertiles by PBMC miR-150 levels (cutoffs of 4.5×10^6 and 9.5×10^6 copies/ng RNA) and by age (i.e., above versus below median of 67.47 years), tabulating the AMD prevalence in each conjoined cell **(Table 4.2)**. This analysis demonstrated a clear stepwise increase in prevalence of AMD going from the lowest to the highest tertile of PBMC miR-150 levels in participants both above median age (i.e., from 18.8% to 53.8% to 87.5%) and below median age (i.e., from 15.8% to 17.4% to 45.5%). These findings strongly support the notion that increased PBMC miR-150 levels are associated with AMD. This trend held true both above and below median age, making it highly unlikely that the differences in PBMC miR-150 levels in AMD patients versus non-AMD controls were solely due to the fact that the AMD patients were, on average, older in age.

miR-150 directly targets stearoyl-CoA desaturase-2 and promotes pathologic angiogenesis

To understand the mechanism by which miR-150 promotes macrophage dysfunction, we sought to identify direct miR-150 targets. Since miRs canonically downregulate their gene targets, we filtered for commonly downregulated genes (fold change < -1.2) both in miR-150^{OE} and NC-transfected macrophages and in aged versus young macrophages. This strategy identified 36 initial putative target genes **(Table 4.3)**. We further narrowed this list by eliminating genes that either did not appear in any of six target identification databases or did not contain a seed sequence in their 3′ UTR. We performed qPCR in aged versus young macrophages on the remaining 26 genes. Of these 26 genes, eight showed significant downregulation in aged macrophages **(Figures 4.5A and 4.5B)**. Of interest, two of the eight genes that were significantly downregulated in aged macrophages are known to play key roles in

fatty acid biosynthesis: fatty acid synthase (*Fasn*) and stearoyl-CoA desaturase-2 (*Scd2*). We confirmed that both genes were indeed downregulated in miR-150[OE] macrophages versus NC-transfected macrophages **(Figures 4.5C and 4.5D)**. To determine the functional effect of *Fasn* and *Scd2* deficiency, we performed siRNA knockdown of these gene targets in macrophages and assessed the inflammation status and angiogenic potential of these macrophages by PCR array. We confirmed siRNA knockdown of *Fasn* and *Scd2* by qPCR **(Figures 4.5E and 4.5F)**. *Fasn*-deficient macrophages exhibited upregulation of only *Ptgs2* and *Tnf* **(Figure 4.5G)** and no upregulation of proangiogenic factors **(Figure 4.5H)**. On the other hand, *Scd2*-deficient macrophages were abnormally activated with upregulation of numerous proinflammatory markers **(Figure 4.5I)** and proangiogenic factors **(Figure 4.5J)**. Of interest, *Vegfa* expression was not altered **(Figure 4.5J)**, suggesting that *Scd2*-mediated regulation of macrophage function is independent from vascular endothelial growth factor (VEGF). These results suggest that *Scd2* may be an important direct target of miR-150, providing a mechanism by which miR-150 regulates macrophage function.

Next, we performed dual-reporter assays to confirm that miR-150 can directly regulate *Scd2* expression. The *Scd2* gene contains two canonical miR-150 seed sequence target sites in its 3′ UTR: a 7mer-A1 (UGGGAGA) and an offset 6mer (UUGGGA) **(Figure 4.6A)**. As expected, co-transfection of a plasmid with the *Scd2* 3′ UTR cloned downstream of a secreted Gaussia luciferase (GLuc) and miR-150 mimic led to decreased GLuc activity compared to co-transfection of the same plasmid with a non-targeting mimic **(Figure 4.6B)**. Removing the 7mer-A1 target site (mutant1) significantly reduced the extent to which miR-150 co-transfection reduced GLuc activity **(Figure 4.6C)**. In contrast, removing the offset 6mer target site (mutant2) did not change the negative regulatory effect of miR-150 co-transfection on GLuc activity

104

(Figure 4.6C). These findings suggest that the 7mer-A1 site is the dominant target site to which miR-150 binds to regulate *Scd2* expression, while the offset 6mer site plays a less important role.

To determine whether downregulation of *Scd2* may promote pathological angiogenesis as seen in wet AMD, we measured the extent to which *Scd2*-deficient macrophages inhibited choroidal neovascularization (CNV) in a well-established murine model of injury-induced angiogenesis in the eye. Although host macrophages play an important role in regulating CNV, we have previously demonstrated that intravitreal injection of functional macrophages can augment the anti-angiogenic effect (Apte et al., 2006). Therefore, we performed laser injury to induce CNV and injected *Scd2*-deficient or NC-transfected macrophages intravitreally by adoptive transfer immediately after injury. Adoptively transferred *Scd2*-deficient macrophages were not able to inhibit choroidal neovascularization as effectively as NC-transfected macrophages **(Figures 4.6D and 4.6E)**. This phenomenon was independent of VEGF since VEGF mRNA expression and protein secretion was not increased in *Scd2*-deficient macrophages **(Figures 4.5H and 4.6F)**. To confirm these in vivo results, we also generated mice lacking *Scd2* in myelomonocytic cells, including macrophages, with the Cre-lox system (*Scd2*$^{-m/-m}$). In agreement with our adoptive transfer experiments, *Scd2*$^{-m/-m}$ mice had larger CNV complexes after laser injury compared to floxed controls (*Scd2*$^{f/f}$) **(Figures 4.6G and 4.6H)**. In contrast, mice lacking *Fasn* in myelomonocytic cells (*Fasn*$^{-m/-m}$) and floxed controls (*Fasn*$^{f/f}$) had similar CNV complex sizes after laser injury **(Figures 4.6I and 4.6J)**. These findings confirm that *Scd2* plays an important role in regulating macrophage function in the context of pathological angiogenesis.

Together, these findings indicate that *Scd2* downregulation secondary to miR-150 upregulation in aged macrophages promotes macrophage dysfunction and pathological

angiogenesis, providing a mechanism by which miR-150 can direct macrophages towards an aged, disease-promoting, and proangiogenic phenotype **(Figure 4.7)**. Our human data confirm the translational relevance of these findings in AMD pathogenesis.

4.4   Discussion

In this study, we report that miR-150 is upregulated in aged murine macrophages of diverse origins and directs aged macrophages towards a disease-promoting phenotype characterized by abnormal activation and promotion of pathologic angiogenesis. miR-150 was previously reported to play important roles in controlling B-cell differentiation by targeting the transcription factor c-Myb (Xiao et al., 2007). Moreover, miR-150 has been reported to regulate de novo lipogenesis by targeting *Fasn* and other lipid-related genes in mammary epithelium (Heinz et al., 2016). Here, we uncover a novel role for miR-150 in macrophages to regulate cholesterol metabolism and lipid trafficking genes involved in AMD based on our RNA-Seq results. In agreement, other miRs have been shown to regulate cholesterol homeostasis. For example, miR-33 (Rayner et al., 2011; Sene et al., 2013), miR-302a (Meiler et al., 2015), and miR-19b (Lv et al., 2014) regulate reverse cholesterol transport by modulating *Abca1* expression.

Consistent with their impaired cholesterol metabolism and lipid trafficking, we report that aged macrophages with miR-150 upregulation have associated alterations in ceramide and phospholipid profiles. These results build on our previous finding that aged macrophages have impaired cholesterol efflux (Sene et al., 2013). Specifically, aged macrophages have a reduced ratio of very long-chain to long-chain ceramides. Ceramides are important signaling molecules in macrophages that modulate cellular responses in many pathways, including inflammation (Schilling et al., 2013). Different molecular ceramide species have been shown to be

106

significantly associated with mortality in coronary artery disease patients independently of traditional risk factors (Tarasov et al., 2014), highlighting their importance in disease pathogenesis. Additionally, we demonstrate that aged macrophages have alterations in phospholipid composition in multiple classes. Of interest, both ceramides and phospholipids are important components of the plasma membrane, and the composition and organization of the plasma membrane have been shown to be important for modulating cholesterol-dependent signaling networks involved in inflammation (Wei et al., 2016).

We propose that broad disruptions in plasma membrane lipids secondary to miR-150 upregulation in aged macrophages modulate the inflammatory status of aged macrophages and thereby predispose them toward a disease-promoting, proangiogenic phenotype. Our lipidomic analysis shows that aged macrophages possess a complex profile of altered lipid composition with remodeling toward long-chain ceramides and a shift towards phospholipids containing unsaturated fatty acids. We provide further insight by demonstrating that one molecular mechanism by which miR-150 regulates lipid metabolism in macrophages is by directly targeting *Scd2*. This gene catalyzes the rate-limiting step in the formation of monounsaturated fatty acids and has been shown to be important in lipid synthesis during early skin and liver development (Miyazaki et al., 2005). Our data establish that *Scd2* is also evidently important in macrophage function, as *Scd2*-deficient macrophages exhibit abnormal activation and promote pathological angiogenesis. Although *Scd2* deficiency alone might be expected to cause accumulation of phospholipids containing saturated fatty acids in aged macrophages, we did not observe this pattern in our lipidomic analysis, suggesting that *Scd2* deficiency does not drive alterations in lipid composition alone. We propose instead that the combination of *Scd2* deficiency and changes in other lipid-related genes causes the altered lipid profile of aged macrophages.

Of translational relevance, our study provides strong evidence that miR-150 plays a role in AMD pathogenesis. Specifically, our data indicate not only that AMD patients have higher PBMC miR-150 levels than control participants but also that increased PBMC miR-150 is significantly associated with increased odds of AMD in a gender- and age-adjusted binary logistic regression model. Although miR-150 levels were associated with disease in human PBMCs, there was no clear relationship between miR-150 levels and age, unlike in murine macrophages, highlighting a difference between murine and human macrophages.

Overall, our findings are timely given a recent report that showed that there is an increase in the number of choroidal macrophages in human eyes with AMD (McLeod et al., 2016), strongly implicating a pathogenic role for macrophages in disease. Moreover, our findings may partially explain why activated macrophages derived from neovascular AMD patients have proangiogenic characteristics (Hagbi-Levi et al., 2017; Nakamura et al., 2015). While other groups have suggested endothelial miR-150 may suppress pathologic ocular neovascularization (Liu et al., 2015; Shen et al., 2008), our findings highlight a distinct, macrophage-specific role for miR-150 that, in fact, promotes pathological ocular neovascularization. These differences are not surprising given that miRs can act in a cell-specific manner. Ultimately, these findings open up novel therapeutic vistas for miR-based therapies for AMD. Moreover, understanding the mechanisms that cause macrophage aging and how aging contributes to AMD also has broad applicability to other age-associated diseases by educating us about critical unifying pathways that drive their pathobiology.

4.5 Methods

Animals. We obtained 18-month-old, wild-type C57BL/6J mice from the National Institute on Aging (Bethesda, MD) and compared them to strain-matched, young (i.e., 2- to 3-month-old) wild-type controls. We obtained mice with floxed *Fasn* alleles (*Fasn*^f/f) (Chakravarthy et al., 2005) from Clay Semenkovich (Washington University School of Medicine, St. Louis, MO) and mice with floxed *Scd2* alleles (*Scd2*^f/f) (Lai et al., 2017; Masuda et al., 2015) from Hide Tsukamoto (Keck School of Medicine of the University of Southern California, Los Angeles, CA). We crossed these floxed mice with mice carrying the lysozyme M-Cre (LysMcre) transgene (Clausen et al., 1999) to generate mice with myelomonocytic-specific deletion of *Fasn* (*Fasn*^-m/-m) and *Scd2* (*Scd2*^-m/-m). We harvested PMs, SMs, and BMDMs from female mice at the ages indicated and used equal proportions of male and female mice for laser-injury CNV experiments. Unless otherwise specified, we used mice that were 2-3 months of age for experimentation.

Macrophages. We harvested PMs from mice five days after elicitation with 4% thioglycollate (Sigma, St. Louis, MO). We harvested SMs from mice by mincing spleens with a sharp razor blade, incubating in spleen dissociation medium (Stem Cell Technologies, Vancouver, Canada) for 30 minutes at room temperature and performing magnetic cell separation with the PE selection kit (Stem Cell Technologies) and PE-conjugated F4/80 monoclonal antibody (clone: BM8; eBioscience, Waltham, MA), following manufacturer's instructions. We cultured PMs and SMs in RPMI 1640 medium (Thermo Fisher, Waltham, MA) supplemented with 10% fetal bovine serum (FBS; Atlanta Biologicals, Lawrenceville, GA) and 1% penicillin-streptomycin (Thermo Fisher). Additionally, we generated bone marrow-derived macrophages (BMDM) by

109

culturing bone marrow aspirates from mice in RPMI 1640 medium (Thermo Fisher) supplemented with 20% L929-conditioned medium, 10% FBS (Atlanta Biologicals), 1% GlutaMAX (Thermo Fisher), and 1% penicillin-streptomycin (Thermo Fisher). Monocytes were allowed to differentiate for one week prior to experimentation. When indicated, we treated macrophages with 25 μg/ml oxidized LDL (oxLDL; Intracel, Frederick, MD) for 24 hours, 25 μg/ml acetylated LDL (acLDL; Intracel, Frederick, MD) for 24 hours, or 100 ng/ml lipopolysaccharide (LPS; Sigma, St. Louis, MO) for 24 hours.

MicroRNA microarray. We profiled microRNA (miR) expression of young and aged peritoneal macrophages that 1) were left untreated, 2) treated with 25 μg/ml acLDL for 24 hours, or 3) treated with 25 μg/ml oxLDL for 24 hours (total of 6 groups; 3 treatments × 2 ages). We extracted RNA with the mirVana miRNA isolation kit (Thermo Fisher), determining quantity and quality of the RNA with a 2100 BioAnalyzer and the Total RNA Pico kit (Agilent Technologies, Santa Clara, CA). All samples (N = 24) had RNA Integrity Numbers > 9.5. We labeled each sample with FlashTag^{TM} Biotin HSR RNA Labeling Kits (Affymetrix, Santa Clara, CA) to prepare them for the GeneChip® miRNA 3.0 Array. We processed the array results with Affymetrix Expression Console (v1.3.1.187) at standard settings (RMA background correction, median polish summarization, and quantile normalization) to generate intensity values with a second set of data produced without quantile normalization. We filtered the data by probeset type and by detection call and removed probesets without a 'detected' call in any of the 24 samples; after this filtering, we retained 1,093 of the initial 1,966 probesets for further statistical analysis. To identify potential outliers, we performed principal component analysis (PCA) and hierarchical clustering and assessed quality control (QC) metrics from Expression Console (e.g.,

110

all probeset RLE means > 0.25). This analysis identified 3 outliers, which we omitted from further analysis. We performed statistical analysis with the R package "limma" (Ritchie et al., 2015) to generate lists of miRs differentially expressed in our various groups based on their p-values and false detection rate (FDR)-adjusted p-values (i.e., q-values). The microarray data are available at the Gene Expression Omnibus (GEO) at NCBI under accession number GSE111323.

microRNA expression profiling. For miR expression profiling, we extracted total RNA with the mirVana miRNA isolation kit (Thermo Fisher) and prepared cDNA with the universal cDNA synthesis kit II (Exiqon, Woburn, MA). We then performed qPCR using ExiLENT SYBR® Green master mix (Exiqon) and microRNA LNA[TM] primer sets (Exiqon). To analyze the data, we used the ΔΔCT method, normalizing to U6 expression.

mRNA expression profiling. For mRNA expression profiling, we extracted RNA with the RNeasy kit (Qiagen, Germantown, MD) and prepared cDNA with the high-capacity cDNA reverse transcription kit (Thermo Fisher). We then performed qPCR with TaqMan[TM] fast advanced master mix (Thermo Fisher) and TaqMan[TM] real-time PCR gene expression assays (Thermo Fisher). We also profiled mRNA expression with custom TaqMan[TM] array plates (Thermo Fisher). We used the ΔΔCT method, normalizing to one or more housekeeping gene(s), as appropriate.

RNA-Sequencing. We extracted total RNA from peritoneal macrophages transfected with either synthetic mir-150-5p or negative control (Exiqon) with TRIzol (Thermo Fisher) followed by column purification with the RNeasy Plus mini kit (Qiagen). We determined the quantity and

quality of the RNA samples with a 2100 BioAnalyzer and the Total RNA Pico kit (Agilent Technologies). All samples (N = 12) had RNA Integrity Numbers > 9.6. We analyzed the transcriptomes of peritoneal macrophages after miR-150 overexpression with RNA-Sequencing (RNA-Seq) with an initial input of 600 ng of total RNA per sample before mRNA enrichment with the rRNA Ribo-Zero rRNA removal kit (Illumina, San Diego, CA). We prepared sequencing libraries with standard protocols. Quality control revealed improper fragmentation of one sample, which was omitted from further analysis. The remaining samples (N = 11) were sequenced in two flowcell lanes on a HiSeq 2500 (Illumina) at the Washington University GTAC. We mapped the sequencing reads to the genome with STAR. Next, we performed a standard EdgeR and Sailfish analysis of gene-level features. We defined a significant up- or down-regulation as a |fold-change| > 1.20 with a false-detection rate (FDR) < 0.20. We performed pathway analysis for enrichment in gene ontology (GO) processes, process networks, and pathway maps with MetaCore (Clarivate Analytics, Philadelphia, PA). The RNA-Seq data are available at the Gene Expression Omnibus (GEO) at NCBI under accession number GSE111323.

Lipidomic analysis. We suspended macrophages in PBS at 2.0×10^6 cells/ml and performed protein precipitation from 100 µl of macrophage suspension to extract ceramides, phosphatidylcholines, phosphatidylethanolamines, phosphatidylinositols, phosphatidylglycerols, and phosphatidylserines. Prior to extraction, we added deuterated d_5-Cer (16:0), d_4-Cer (22:0), and d_4-Cer (24:0) as internal standards for ceramides and PC (28:2), PE (32:2), PG (30:0), PI (32:0) and PS (28:0) as internal standards for the other lipid classes. We measured lipids with a Shimadzu 10A HPLC system (Kyoto, Japan) and a Shimadzu SIL-20AC HT auto-sampler

(Kyoto, Japan) coupled to a Thermo Scientific TSQ Quantum Ultra triple quadrupole mass spectrometer operated in SRM mode under ESI(+). We conducted data processing with Xcalibur^{TM} (Thermo Fisher). We prepared quality control (QC) samples by pooling aliquots of the study samples and injected them between every five samples to monitor instrument performance, omitting lipid species with coefficients of variance >15% in QC samples. We performed relative quantification by comparing the peak area ratios of the analytes to the corresponding internal standards.

Human subjects. To isolate peripheral blood mononuclear cells (PBMCs), we performed density gradient centrifugation with BD Vacutainer CPT^{TM} cell preparation tubes (Franklin Lakes, NJ). We stored PBMC pellets at -80°C until further analysis. We classified patients as no AMD, early AMD, or wet AMD based on established clinical criteria (Ferris et al., 2005). Early AMD patients had either moderate drusen (>63 μm) or pigment changes in at least one eye but no CNV or GA in either eye at the time of sample collection. Wet AMD patients had CNV in at least one eye at the time of sample collection. We excluded patients with pattern dystrophy, macular telangiectasia, dominant drusen, or central serous chorioretinopathy.

Absolute microRNA-150 quantification in human PBMCs. We extracted RNA from PBMCs with the mirVana^{TM} miRNA isolation kit (Thermo Fisher) and performed reverse transcription (RT) with the universal cDNA synthesis kit II (Exiqon) by adding 2 μl of RNA to 2 μl of 5× reaction buffer, 1 μl of enzyme mix, and 5 μl of nuclease-free H$_2$O (total volume: 10 μl). We diluted the cDNA to a final volume of 60 μl and performed miRCURY LNA Universal RT microRNA PCR by adding 4 μl of diluted cDNA to 1 μl of the appropriate primer and 5 μl of

113

ExiLENT SYBR Green master mix (total volume: 10 µl). To determine absolute copy number of hsa-miR-150-5p, we prepared standard curves with serial dilutions of synthetic hsa-miR-150-5p (Integrated DNA Technologies, Coralville, IA) ranging from 10^4 copies per 2 µl input to 10^{10} copies per 2 µl input, followed by RT and PCR as above. To account for differences in RNA extraction and RT efficiency performed on separate occasions, we spiked in 20 fmol of synthetic cel-miR-39-3p (Integrated DNA Technologies) into each sample prior to RNA extraction and normalized to the global arithmetic mean. We normalized miR-150 copy number for each patient by dividing by the total RNA used for RT.

miR-150 overexpression. To transiently overexpress miR-150 in peritoneal macrophages, we used commercially available miRCURY LNA™ microRNA mimics (Exiqon), following standard protocols for fast-forward transfection. In short, we plated peritoneal macrophages at 1.0×10^6 cells/well in 6-well plates. Two hours after plating, we prepared transfection complexes by combining miR mimic (20 nM) and HiPerFect transfection reagent (18 µl/well; Qiagen) in RPMI medium supplemented with 10% FBS (Atlanta Biologicals) and 1% penicillin-streptomycin (Thermo Fisher), incubating for 15 minutes at room temperature before adding to the cells. We assessed transfection efficiency with fluorescence microscopy by visualizing FAM-labeled microRNA mimics.

miR-150 target identification. To identify miR-150 targets, we retrieved 3′ UTR sequences from the UCSC Genome Brower (genome.ucsc.edu; Mouse Assembly GRCm38/mm10) and manually searched for the presence of relevant miR-150 seed sequences (8mer site: UUGGGAGA; 7mer-m8 site: UUGGGAG; 7mer-A1 site: UGGGAGA; 6mer site: UGGGAG;

114

offset 6mer site: UUGGGA). Additionally, we used existing miR target identification databases: TargetScanMouse (Release 7.1) (Agarwal et al., 2015), DIANA-microT-CDS (Version 5.0) (Paraskevopoulou et al., 2013), DIANA-TarBase (Version 7.0) (Vlachos et al., 2015), miRDB (Wong and Wang, 2015), RNA22 (Version 2.0) (Miranda et al., 2006), and microRNA.org (August 2010 Release) (Betel et al., 2008).

***Fasn/Scd2* knockdown.** To transiently knock down *Fasn* and *Scd2*, we used commercially available FlexiTube siRNA (Qiagen), following standard protocols for fast-forward transfection. In short, we plated peritoneal macrophages at 1.0×10^6 cells/well in 6-well plates. Two hours after plating, we prepared siRNA transfection complexes by combining siRNA (50 nM) and HiPerFect transfection reagent (18 µl/well; Qiagen) in RPMI medium supplemented with 10% FBS (Atlanta Biologicals) and 1% penicillin-streptomycin (Thermo Fisher), incubating for 15 minutes at room temperature before adding to the cells. We confirmed efficient siRNA knockdown by qPCR. We analyzed macrophage activation and function 48 hours after transfection.

miRNA target dual-reporter assays. We ordered custom miTarget[TM] 3′ UTR miRNA target clones from GeneCopoeia (Rockville, MD) with wild-type or mutated *Scd2* 3′ UTR inserted downstream of a secreted Gaussia luciferase (GLuc) reporter gene driven by the SV40 promoter and a secreted alkaline phosphatase (SEAP) reporter gene driven by a CMV promoter. We co-transfected 293T cells (ATCC, Manassas, VA), cultured routinely in high-glucose DMEM (Thermo Fisher) supplemented with 10% FBS (Atlanta Biologicals), with the target clone and either miR-150 mimic or non-targeting negative control mimic (Exiqon), following

115

manufacturer's instructions. In brief, we plated 293T cells in 96-well plates at 2.0×10^4 cells/well the day before transfection. On the day of transfection, we prepared transfection complexes by combining the target clone (100 ng/well), miR mimic (20 nM), Lipofectamine™ 3000 (0.15 µl/well; Thermo Fisher), and P3000™ reagent (0.20 µl/well) in Opti-MEM™ medium (Thermo Fisher) and incubating for 30 minutes at room temperature before adding to the cells. 48 hours after transfection, we collected the supernatant to measure GLuc activity with the Secrete Pair™ Dual Luminescence assay kit (GeneCopoeia). We normalized for transfection efficiency by measuring SEAP activity. We optimized co-transfection conditions with a positive-control pmaxGFP™ plasmid (Lonza, Basel, Switzerland).

Choroidal neovascularization (CNV) experiments. We performed laser-induced choroidal neovascularization as described previously (Dong et al., 2013). Briefly, we anesthetized mice and placed four laser spots around the optic disc (200 mW, 0.1 s, 100 µm spot size) using a slit-lamp delivery system with a cover glass as a contact lens. Seven days after injury, we perfused the mice with 2,000 µl of 5 mg/ml fluorescein isothiocyanate (FITC)-dextran (M.W. 2,000,000; Sigma) through the left ventricle. We then enucleated the eyes and fixed them in 2% paraformaldehyde (PFA; Alfa Aesar, Haverhill, MA) for 30 minutes. After fixation, we washed the eyes with PBS and flat-mounted the RPE-choroid complex onto a glass slide. We acquired Z-stack images of the CNV spots using an Olympus FV1000 confocal microscope (Waltham, MA) and processed images with ImageJ (NIH, Bethesda, MD) to generate pseudo-volumetric two-dimensional images. After excluding laser spots that resulted in retinal, subretinal, or vitreous hemorrhage, we quantified pixel intensity using MetaMorph (Molecular Devices, Sunnyvale, CA). For immunotherapy experiments, we adoptively transferred 100,000 macrophages into each

116

eye in 2 µl PBS immediately following laser injury via intravitreal injection with a 10 µl Neuros Model 1701 RN syringe (point style 4) and small-hub, 31-gauge needles (Hamilton, Reno, NV).

VEGF measurements. We measured VEGF secretion in supernatants from macrophages with the mouse VEGF Quantikine ELISA kit (R&D Systems, Minneapolis, MN), following manufacturer's instructions.

Statistics. We performed statistical analysis with Prism 5 (Graphpad) or SPSS Statistics (Version 23; IBM, Armonk, NY). We assessed the normality of our data graphically and with the Kolmogorov-Smirnov test, using non-parametric alternatives when appropriate. When comparing a single variable between two groups, we used 2-tailed t-tests or 2-tailed Mann-Whitney U tests. For other analyses, we performed the appropriate statistical test for each type of data. A P-value less than 0.05 was considered significant. Open circles depict individual data points or individual human subjects. Box-and-whisker plots depict medians with boxes outlining the interquartile range and whiskers indicating the minima and maxima.

We performed an a priori power calculation with G*Power 3.1 (Faul et al., 2007) to determine the appropriate sample size for our human studies. To detect a significant difference between AMD patients and control subjects (allocation ratio: 1.0:1.5) at the two-sided $\alpha = 0.05$ level with an estimated effect size d of 0.6 based on pilot experiments and 80% power, we calculated that we needed to recruit 94 subjects total. We exceeded this threshold (N = 106), yielding adequate statistical power to detect our anticipated difference. To model the relationship between PBMC miR-150 levels and AMD, we generated a binary logistic regression model. Our model included the predictor variables of age at the time of sample collection, gender, and $\log_{10}$-

117

transformed PBMC miR-150 levels. We assessed model fit with the Hosmer-Lemeshow lack-of-fit test and performed model diagnostics by examining Cook's distances, leverages, and residual deviances. No cases were omitted upon sensitivity analysis. We checked for collinearity by examining variance inflation factors (VIF). We used an unadjusted alpha of 0.05 for the binary logistic regression.

Study approval. All animal experiments were reviewed and approved by the Institutional Animal Care and Use Committee (IACUC) of Washington University in St. Louis (St. Louis, MO) and performed in accordance with the Washington University School of Medicine Animal Care and Use guidelines. The human study was reviewed and approved by the Human Research Protection Office of Washington University in St. Louis (St. Louis, MO) and adhered to the Declaration of Helsinki. We obtained informed consent from all human subjects prior to blood collection.

4.6   Acknowledgements

118

Figure 4.1. microRNA-150 is upregulated in aged macrophages of diverse origins. (A) In young macrophages, ten microRNAs were downregulated similarly in response to acetylated low-density lipoprotein (acLDL) and oxidized low-density lipoprotein (oxLDL). (B) In aged macrophages, five microRNAs were dysregulated similarly in response to acLDL and oxLDL. (C) In untreated (UT), acLDL-treated, and oxLDL-treated macrophages, five microRNAs were dysregulated similarly in aged and young macrophages under the same treatment conditions. microRNA-150 was upregulated in aged peritoneal macrophages (PM) (D; N=12/group; 2-tailed Mann-Whitney U test), aged splenic macrophages (SM) (E; N=13/group; 2-tailed Mann-Whitney U test), and aged bone marrow-derived macrophages (BMDM) (F; N=10/group; 2-tailed, unpaired Welch's t-test). (G) Upregulation of microRNA-150 in aged PMs was not affected by treatment with acLDL (N=7/group; 2-tailed Mann-Whitney U test), oxLDL (N=7/group; 2-tailed, unpaired Welch's t-test), or lipopolysaccharide (LPS) (N=5/group; 2-tailed Mann-Whitney U test). (H) Upregulation of microRNA-150 in aged BMDMs was not affected by treatment with oxLDL (N=5/group; 2-tailed Mann-Whitney U test) or LPS (N=5/group; 2-tailed Mann-Whitney U test). Open circles depict individual data points; graphs depict mean ± S.E.M. (A-F) (* P < 0.05; ** P < 0.01; **** P < 0.0001).
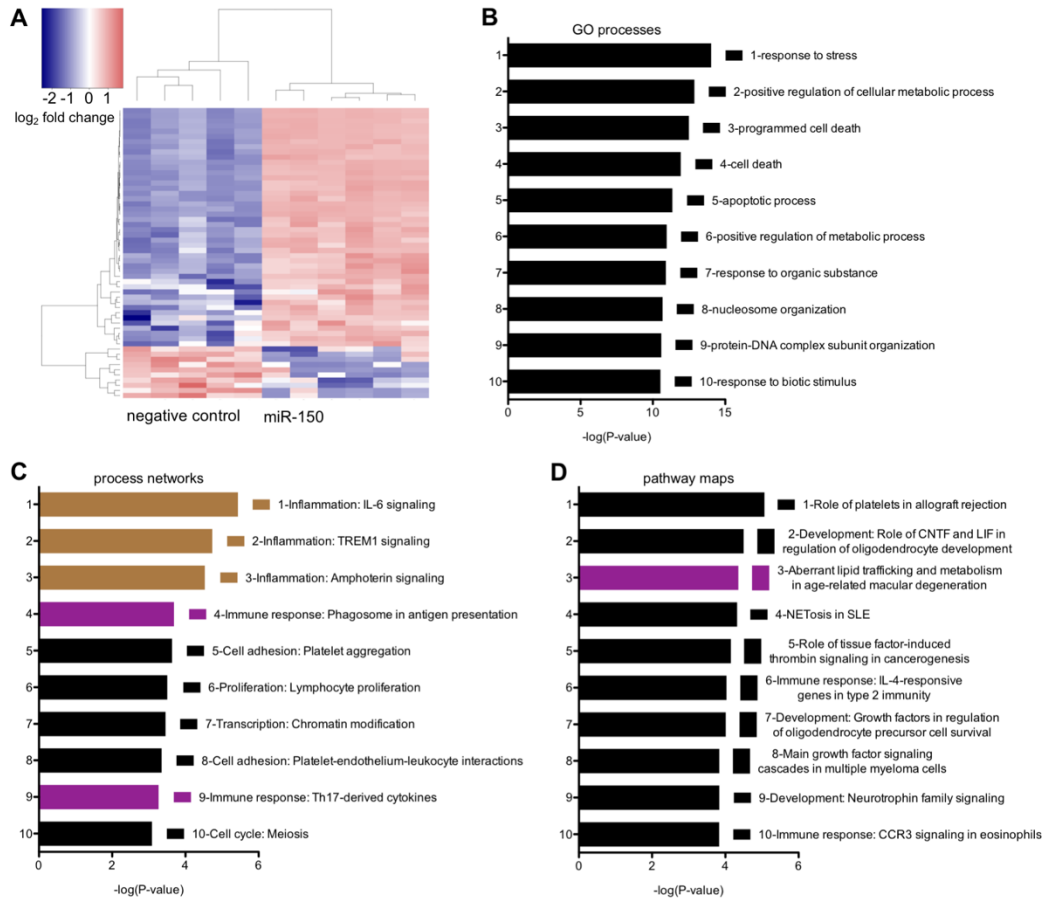
Figure 4.2. microRNA-150 (miR-150) regulates inflammation and lipid metabolism in macrophages. (A) RNA-Sequencing followed by hierarchical clustering revealed clear transcriptomic differences between macrophages transfected with miR-150 mimic versus those transfected with a non-targeting negative control. Pathway analysis of the dysregulated genes in miR-150-overexpressing macrophages that are also dysregulated in aged macrophages (Lin et al., unpublished observations) suggested perturbations in numerous gene ontology (GO) processes (B), process networks (C), and pathway maps (D). The altered transcriptomic profile of miR-150-overexpressing macrophages suggested dysregulation of numerous inflammation and immune response process networks (C; brown and purple, respectively) and aberrant lipid trafficking and metabolism in age-related macular degeneration (D; purple).

121
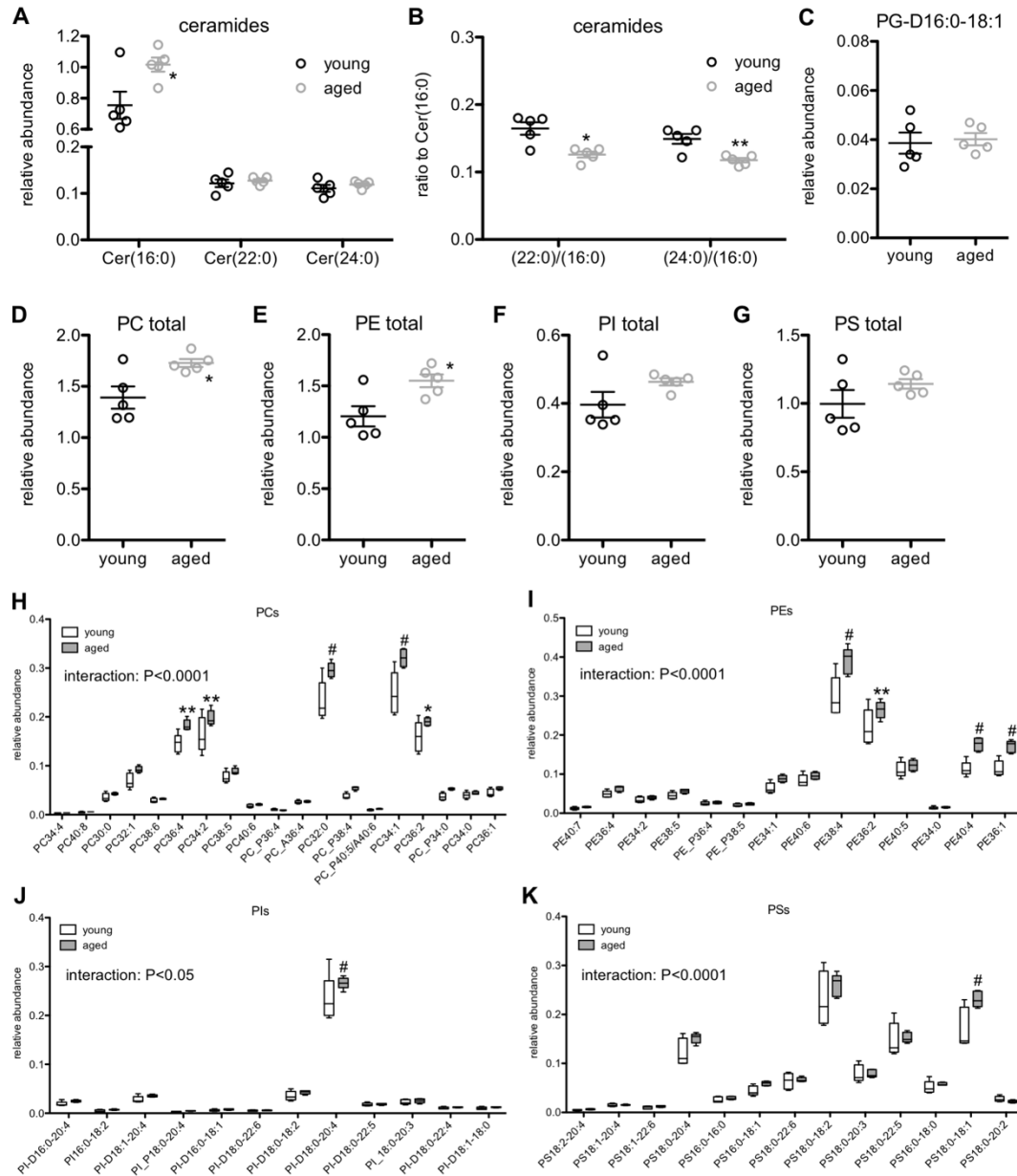
Figure 4.3. Aged macrophages have altered ceramide and phospholipid profiles. (A) Aged macrophages contained significantly more long-chain Cer(16:0) than young macrophages but similar levels of very long-chain Cer(22:0) and Cer(24:0) (N=5/group; 2-tailed, unpaired Welch's t-test), resulting in decreased Cer(22:0)/Cer(16:0) and Cer(24:0)/Cer(16:0) ratios (B; N=5/group; 2-tailed, unpaired Welch's t-test). Young and aged macrophages had similar phosphatidylglycerol (PG)-D16:0-18:1 content (C; N=5/group; 2-tailed, unpaired student's t-test). Aged macrophages had higher total phosphatidylcholine (PC) (D; N=5/group; 2-tailed, unpaired student's t-test) and higher total phosphatidylethanolamine (PE) (E; N=5/group; 2-tailed, unpaired student's t-test) but similar total phosphatidylinositol (PI) (F; N=5/group; 2-tailed, unpaired Welch's t-test) and similar total phosphatidylserine (PS) (G; N=5/group; 2-tailed, unpaired Welch's t-test). Analysis of individual species revealed an interaction between age and species identity with increased levels of certain species but not others within each phospholipid class (H-K; N=5/group; 2-way, repeated-measures ANOVA with Bonferroni post-hoc test). Open circles depict individual data points; graphs depict mean ± S.E.M. (A-G) (* $P < 0.05$; ** $P < 0.01$; # $P < 0.0001$).
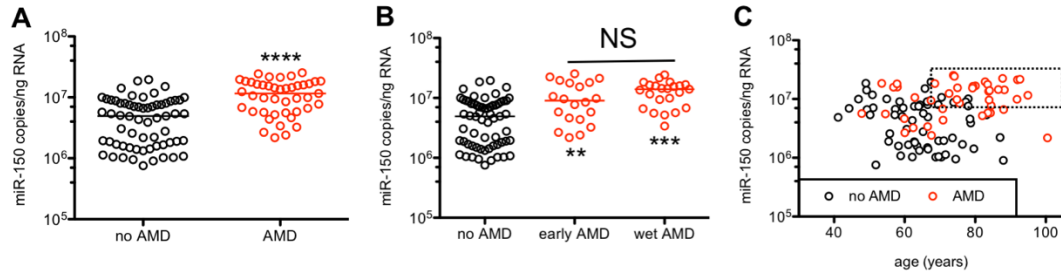
**Figure 4.4.** Upregulation of microRNA-150 in human peripheral blood mononuclear cells (PBMCs) is associated with age-related macular degeneration (AMD). (A) AMD patients (N=43) had higher PBMC microRNA-150 copy numbers compared to controls (N=63; 2-tailed Mann-Whitney U test). (B) Both early AMD (N=20) and wet AMD patients (N=23) had higher PBMC microRNA-150 copy numbers compared to controls (N=63), but there was no significant difference between early and wet AMD patients (Kruskal-Wallis test with Dunn's multiple comparison post-hoc test). (C) There was no correlation between PBMC microRNA-150 copy number and age in AMD patients or controls. Patients in the highest tertile of microRNA-150 copy number and above median age, as indicated by the dashed rectangle, had the highest prevalence of AMD (87.5%). Open circles depict individual human subjects (A-C); horizontal lines depict medians (A-B) (** $P < 0.01$; *** $P < 0.001$; **** $P < 0.0001$; NS: non-significant).
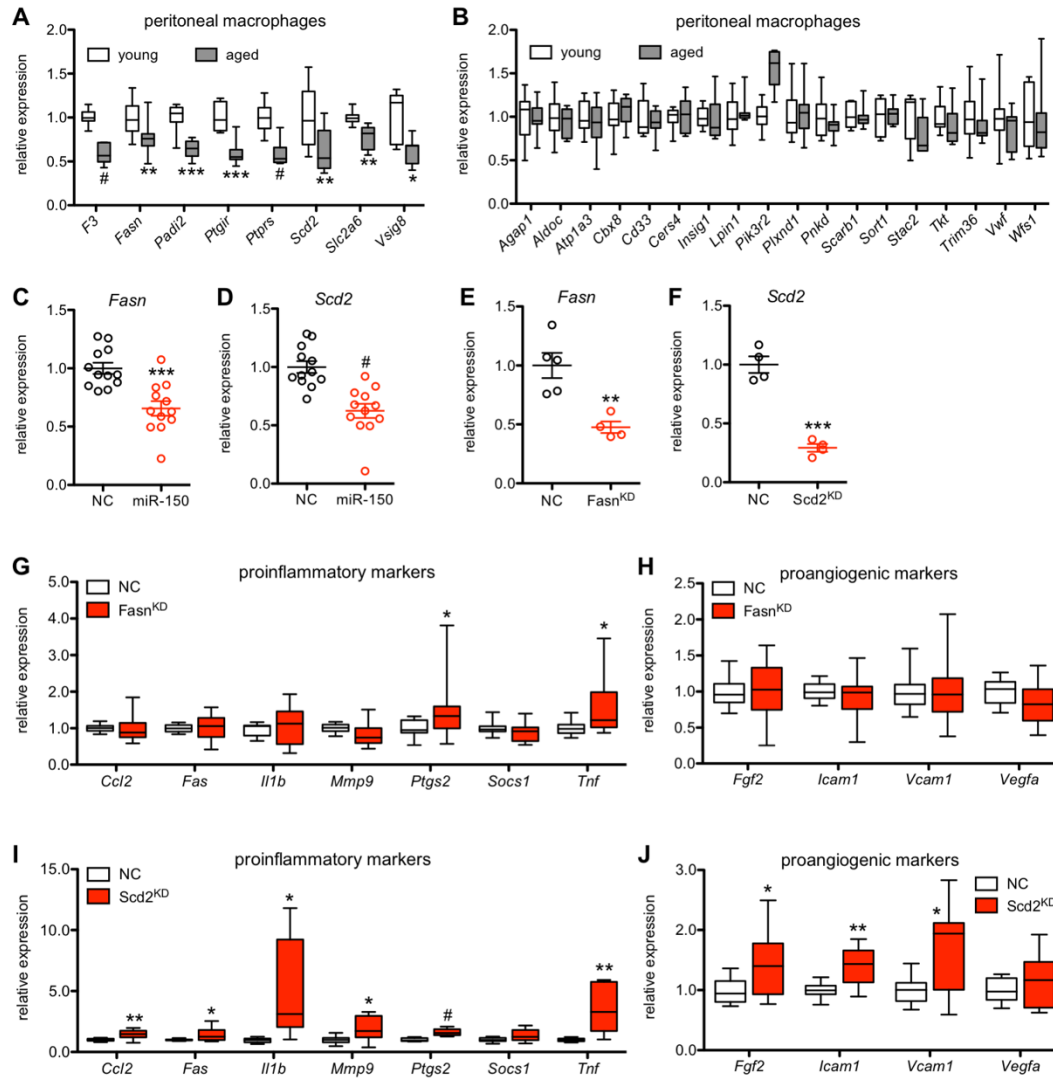
Figure 4.5. microRNA-150 modulates fatty acid synthase (*Fasn*) and stearoyl-CoA desaturase-2 (*Scd2*) expression. (A-B) Eight of the 26 putative microRNA-150 targets had decreased expression in aged macrophages (N=6-12/group; 2-tailed, unpaired Welch's t-test). (C-D) microRNA-150 mimic-transfected macrophages had reduced expression of *Fasn* and *Scd2* compared to non-targeting negative control (NC)-transfected macrophages (N=12/group; 2-tailed, unpaired student's t-test). (E-F) Macrophages transfected with *Fasn*- and *Scd2*-targeting small-interfering RNA (siRNA) had reduced expression of target genes (N=4-5/group; 2-tailed, unpaired student's t-test). (G-H) *Fasn*-deficient (Fasn^KD^) macrophages were somewhat abnormally activated but had normal expression of proangiogenic factors (N=14/group; 2-tailed, unpaired Welch's t-test). (I-J) *Scd2*-deficient (Scd2^KD^) macrophages were abnormally activated and had increased expression of proangiogenic factors (N=10/group; 2-tailed, unpaired Welch's t-test). Open circles depict individual data points; graphs depict mean ± S.E.M. (C-F) (* $P < 0.05$; ** $P < 0.01$; *** $P < 0.001$; # $P < 0.0001$).

124
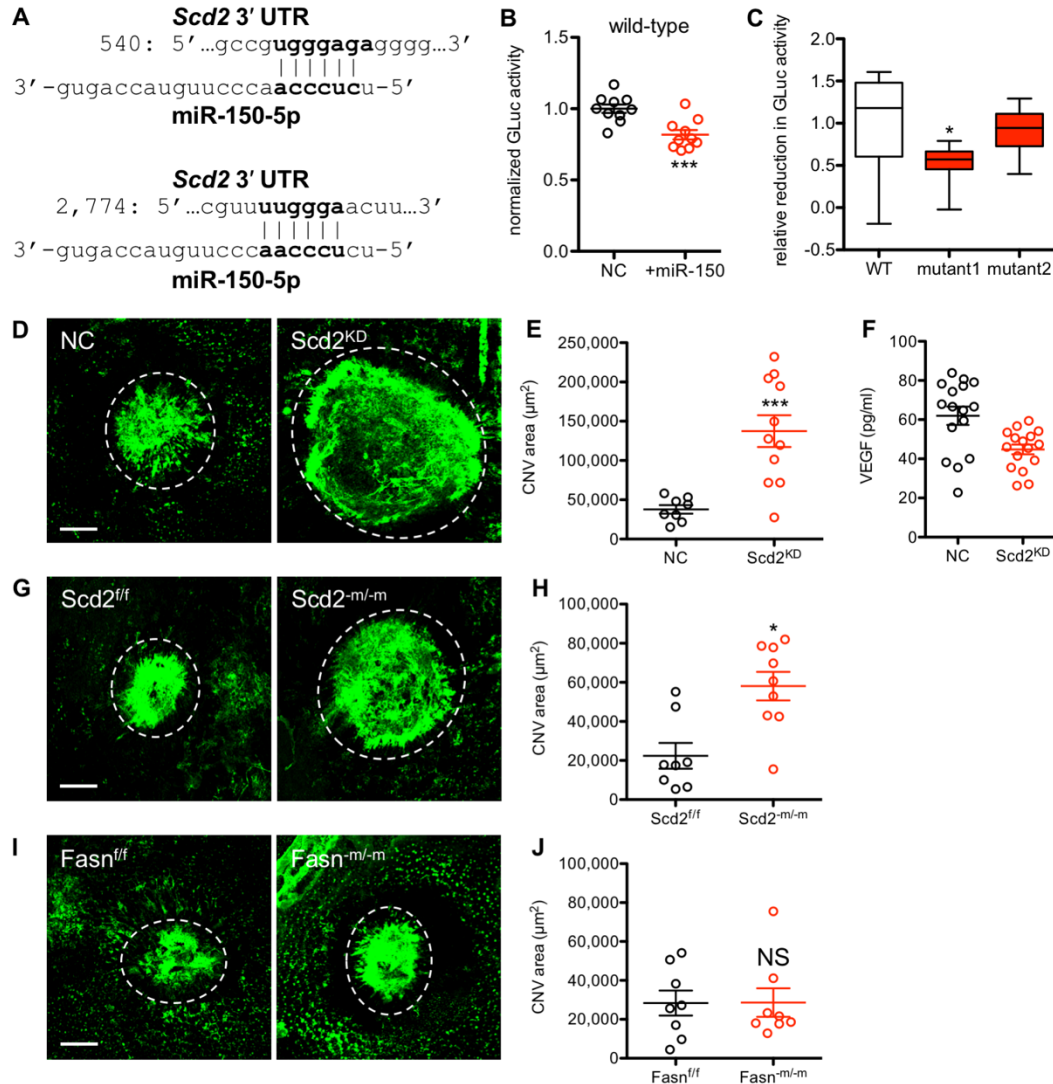
Figure 4.6. microRNA-150 directly targets *Scd2* and thereby promotes pathological angiogenesis. (A) The 3′ untranslated region (UTR) of *Scd2* contains canonical 7mer-A1 and offset 6mer microRNA-150 binding sites. (B) Co-transfection of a dual-reporter plasmid with the *Scd2* 3′ UTR inserted downstream of a secreted Gaussia luciferase (GLuc) reporter gene and microRNA-150 mimic led to reduced GLuc activity compared to co-transfection of the same plasmid with a negative-control (NC) mimic (N=10/group; 2-tailed, unpaired student's t-test). (C) Removing the 7mer-A1 target site (mutant1) but not the offset 6mer target site (mutant2) reduced the extent to which microRNA-150 co-transfection inhibited GLuc activity (N=10/group; Kruskal-Wallis test with Dunn's multiple comparison post-hoc test; WT = wild-type). (D-E) Adoptively transferred *Scd2*-deficient (Scd2^{KD}) macrophages were less able to inhibit laser injury-induced choroidal neovascularization (CNV) compared to NC-transfected macrophages (D: representative images from N=8-11 burns/group; 2-tailed, unpaired Welch's t-test). (F) In vitro VEGF secretion was not significantly increased in *Scd2*-deficient macrophages (N=16/group; 2-tailed, unpaired Welch's t-test). (G-H) *Scd2*$^{-m/-m}$ mice exhibited larger CNV complexes after laser injury compared to *Scd2*$^{f/f}$ mice (G: representative images from N=8-9 burns/group; 2-tailed Mann-Whitney U test). (I-J) *Fasn*$^{-m/-m}$ and *Fasn*$^{f/f}$ mice had similarly sized CNV complexes after laser injury (I: representative images from N=8 burns/group; 2-tailed Mann-Whitney U test). Scale bars represent 100 µm (D, G, I). Open circles depict individual data points; graphs depict mean ± S.E.M. (B, E-F, H, J) (* P < 0.05; *** P < 0.001; NS: non-significant).
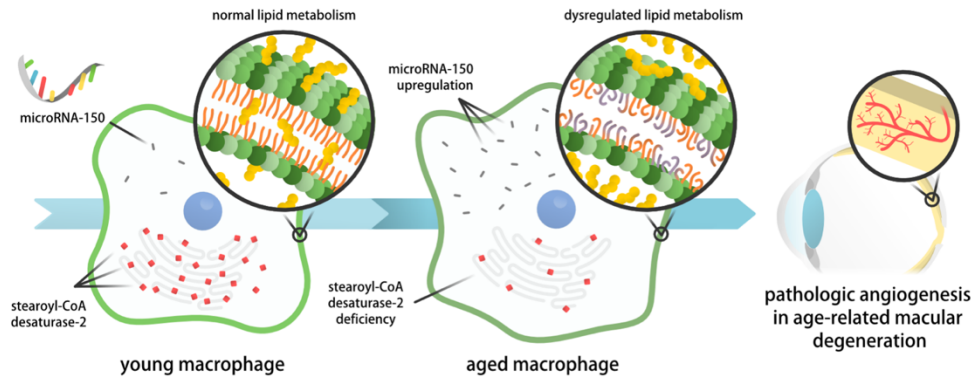
Figure 4.7. Upregulation of miR-150 in aged macrophages causes stearoyl-CoA desaturase-2 deficiency and dysregulated lipid metabolism and thereby promotes pathological angiogenesis, as seen in age-related macular degeneration.

Table 4.1. Demographic and clinical characteristics of human subjects.

Variable	Control	AMD	P-value
Age, mean (standard deviation)	64.57 (10.27)	75.48 (12.77)	<0.001[a]
Sex, N			
Male	36	20	0.282[b]
Female	27	23	
AMD status, N			
No AMD	63	0	N/A
Early AMD	0	20	
Advanced neovascular (wet) AMD	0	23	

[a]Significant by 2-tailed, unpaired Welch's t-test; [b]Non-significant by X^2 test.

127

Table 4.2. Age-related macular degeneration as a function of age and peripheral blood mononuclear cell (PBMC) microRNA-150 (miR-150) levels.

		Age		
		Below median	**Above median**	**Total**
PBMC miR-150	**Lowest tertile**	3/19 (15.8%)	3/16 (18.8%)	6/35 (17.1%)
	Middle tertile	4/23 (17.4%)	7/13 (53.8%)	11/36 (30.6%)
	Highest tertile	5/11 (45.5%)	21/24 (87.5%)	26/35 (74.3%)
	Total	12/53 (22.6%)	31/53 (58.5%)	43/106 (40.6%)

Table 4.3. List of putative microRNA-150 targets.

Gene symbol	Fold change (aged versus young)	Fold change (miR-150^{OE} versus NC)
3110070M22Rik	-1.39	-1.86
Aldoc	-1.85	-1.30
Atp1a3	-1.46	-1.25
Ak8	-1.42	-1.25
Cbx8	-1.28	-1.46
Cd33	-1.48	-1.23
Agap1	-1.33	-1.30
S100a8	-1.21	-1.49
Slc29a1	-1.30	-1.29
Fasn	-1.55	-1.20
Ptgir	-1.82	-1.21
Gsn	-1.26	-1.24
Pygl	-1.21	-1.21
Insig1	-1.62	-1.26
Itgax	-1.84	-1.26
Cers4	-1.24	-1.30
Ldhb	-1.25	-1.28
Lpin1	-1.31	-1.21
Mvd	-1.77	-1.36
Padi2	-1.45	-1.34
Pik3r2	-1.20	-1.22
Pnkd	-1.51	-1.29
Ptprs	-1.34	-1.45
Plxnd1	-1.43	-1.21
Ptgir	-1.82	-1.21
Slc2a6	-1.51	-1.31
Scarb1	-1.35	-1.22
Stac2	-1.34	-1.28
Scd2	-3.65	-1.30
Sort1	-1.56	-1.24
Tkt	-1.25	-1.24
Trim36	-1.61	-1.23
F3	-1.39	-1.30
Vsig8	-1.91	-1.29
Wfs1	-1.36	-1.34
Vwf	-1.32	-1.54

129

Chapter 5:

Conclusions

This chapter is adapted, in part, from an invited review article published in ***Progress in Retinal and Eye Research***.

Lin JB, Apte RS. (2018). NAD$^+$ and sirtuins in retinal degenerative diseases: A look at future therapies. Prog Retin Eye Res, 67:118-129. doi: 10.1016/j.preteyeres.2018.06.002.

5.1 Summary: NAD$^+$ in Retinal Degenerative Diseases

A major cause of blindness is retinal degenerative diseases. Despite their heterogeneity, retinal degenerations typically converge on an endpoint of photoreceptor death, suggesting that they share common pathogenic mechanisms. To date, many studies of inherited retinal degenerations have focused on the genetic defects that cause photoreceptor death and blindness. Rationally, ensuing translational efforts have focused on gene therapy and stem cell approaches. However, these strategies have limitations since gene therapy must be tailored for each causative mutation, a challenging proposition since hundreds of causative gene mutations have been identified for blinding diseases. Moreover, stem cells do not prevent photoreceptor death and have many barriers to their development, such as tumorigenicity.

The long-term goal of the first aim of my thesis research was to identify a unifying molecular mechanism in the pathogenesis of retinal degenerations that may lead to novel therapeutic approaches for preventing photoreceptor death regardless of its etiology. Since photoreceptors are highly metabolically active but have limited mitochondrial reserve, metabolic dysfunction may contribute to photoreceptor demise in diverse retinal diseases. Nicotinamide adenine dinucleotide (NAD$^+$) is known to be important for metabolism both as a cofactor for dehydrogenases and as a cosubstrate for sirtuins that regulate mitochondrial function (e.g., SIRT3). The possibility that NAD$^+$ biosynthesis is important for photoreceptor function is supported by recent studies identifying that Leber congenital amaurosis (LCA), one of the leading causes of childhood blindness, can be caused by mutations in the NAD$^+$ biosynthetic enzyme, nicotinamide mononucleotide adenylyltransferase 1 (NMNAT1).

To complete the first aim of my thesis, I explored the role of NAD$^+$ biosynthesis in photoreceptor survival. Using the Cre-lox system, I generated mice that lacked nicotinamide

131

phosphoribosyltransferase (*Nampt*), the rate-limiting enzyme in the major NAD^+ biosynthetic pathway beginning with nicotinamide, specifically from rod or cone photoreceptors. I found that these mutations caused rapid retinal degeneration, which closely mirrored the clinical course of retinitis pigmentosa. This vision loss could be rescued with the NAD^+ intermediate nicotinamide mononucleotide (NMN). Furthermore, I found that *Nampt* deletion caused NAD^+ deficiency, which led to glycolytic dysfunction, defects in oxidative respiration, and, ultimately, photoreceptor death. I further demonstrated that the NAD^+-dependent mitochondrial deacylases SIRT3 and SIRT5 play important roles in retinal homeostasis and that NAD^+ deficiency also causes SIRT3 dysfunction, further contributing to mitochondrial dysfunction. I also identified that retinal NAD^+ deficiency was an early feature of multiple mouse models of retinal dysfunction, supporting the idea that NAD^+ intermediates may be therapeutic against diverse retinal degenerations. These therapeutic approaches would be highly innovative, as they could facilitate photoreceptor survival independent of the causative mutation and may also be therapeutic for non-inherited, blinding diseases. These findings also have broad implications for other neurodegenerative diseases with associated metabolic dysfunction. Although numerous studies have confirmed the importance of NAD^+ and sirtuins in the retina and in other tissues, more studies are necessary to fully unleash their translational potential.

For example, intracellular NAD^+ partitions into subcellular pools in the nucleus, cytoplasm, and mitochondria. No study to date has determined which subcellular pool(s) of NAD^+ are essential for photoreceptor function. The fact that mutations in NMNAT1, the NMNAT isoform with nuclear function, causes blindness suggests that the nuclear NAD^+ pool is essential for vision. However, this possibility needs to be tested rigorously. Moreover, there may be crosstalk and movement of NAD^+ between these subcellular pools. Indeed, impaired NAD^+

132

trafficking may also play pathogenic roles in disease. Further understanding of the subcellular organization of NAD^+ is particularly important since sirtuins, molecular sensors of NAD^+ availability, also have a distinct pattern of subcellular organization. Therefore, it is possible that restrictions in NAD^+ availability in certain subcellular compartments but not others may cause impaired activity of a specific sirtuin, which are important principles to consider when developing novel therapeutic approaches.

Recent studies suggest that there is also an extracellular source of NAD^+, which may have its own important physiological role. In fact, NAMPT has two forms: intracellular NAMPT (iNAMPT) and extracellular NAMPT (eNAMPT). Whereas iNAMPT localizes intracellularly and likely contributes to NAD^+ pools to be used within the cell, eNAMPT circulates in plasma and in other biofluids and can regulate physiology in a systemic manner. eNAMPT (also known as PBEF or visfatin) was previously thought to be a cytokine or a hormone based on its pleiotropic effects, but further investigation revealed that these effects are caused by its robust NAD^+ biosynthetic function (Revollo et al., 2007). Recent studies have confirmed that eNAMPT's ability to regulate systemic NAD^+ biosynthesis allows it to regulate distant target cells, including pancreatic beta cells (Revollo et al., 2007) and hypothalamic neurons (Yoon et al., 2015). eNAMPT may also regulate retinal physiology.

Finally, numerous studies have tested whether NAD^+ intermediates are therapeutic in animal models of disease (Lin et al., 2016a; Mills et al., 2016; Williams et al., 2017). Human clinical trials have already begun to investigate whether NAD^+ intermediates improve cardiometabolic health (NCT03151239), treat mitochondrial diseases/myopathies (NCT03432871), or improve cognition in patients with mild cognitive impairment (NCT02942888). Many other similar studies are currently underway to evaluate the therapeutic

potential of NAD$^+$ intermediates for diverse human diseases (see clinicaltrials.gov). However, there still remains some uncertainly regarding the in vivo pharmacokinetics of NAD$^+$ intermediates. Although both NR and NMN have been shown to boost intracellular NAD$^+$, how these metabolites enter the cell remains unclear. One possibility is that there is an NMN transporter that allows for rapid uptake of NMN directly into the cell for intracellular conversion into NAD$^+$ (Yoshino et al., 2018). However, this hypothesis was challenged by a recent study that demonstrated that in some, but not all, tissues, extracellular NMN must first be converted to NR by nicotinamide riboside kinase 1 (NRK1) before it can be transported to the intracellular compartment (Ratajczak et al., 2016). Further studies are essential to clarify this discrepancy. Future randomized clinical trials designed to evaluate safety and efficacy of NMN and NR, especially those that compare them head to head, will be particularly informative in clarifying whether one of these NAD$^+$ intermediates has superior bioavailability.

5.2   Summary: Macrophage Aging and AMD

We and others have previously reported that macrophages play pathogenic roles in diverse diseases of aging, including age-related macular degeneration (AMD), a leading cause of blindness in older adults, especially in industrialized countries such as the United States. Aged macrophages tend to drift towards a proangiogenic, M2-like phenotype, permitting pathologic angiogenesis. Although prior studies have explored the functional consequences of macrophage aging, less is known about its cellular basis or what defines the transition from physiologic aging to disease. The long-term goal of the second aim of my thesis research was 1) to distinguish physiologic, 'healthy' changes in aged macrophages from pathogenic age-associated changes

134

that promote disease and 2) to identify one or more microRNA(s) that regulate the process of pathologic macrophage aging.

I first confirmed that, despite their frequent self-renewal, macrophages from old mice exhibited numerous signs of aging, such as impaired oxidative respiration and increased expression of senescence markers. I next performed transcriptomic profiling of aged murine macrophages by microarray to characterize the major changes associated with macrophage aging. Pathway analysis revealed dysregulation of diverse cellular pathways, especially in cholesterol homeostasis, that manifested in altered oxysterol signatures. To assess which of these changes were disease-promoting, I collected human samples from human AMD patients and healthy controls. While certain oxysterols in human peripheral blood mononuclear cells and plasma exhibited age-associated changes, as in the murine samples, others such as plasma 24-hydroxycholesterol were specifically associated with AMD after controlling for age and gender. These findings suggest that oxysterols can discriminate disease from physiologic aging.

I next sought to understand the role of microRNAs, which modulate immune processes, in regulating macrophage dysfunction and thereby promoting age-associated diseases. I began by performing a microRNA microarray to identify putative candidates for microRNAs that regulate macrophage aging. microRNA-150 emerged as the most likely candidate, as it was upregulated by the highest fold change in aged macrophages of diverse origins. Next, I performed RNA-Sequencing to assess the transcriptomic changes associated with microRNA-150 upregulation. Of interest, pathway analysis revealed enrichment for dysregulated genes in lipid trafficking and cholesterol metabolism. Molecular profiling confirmed that, consistent with impaired lipid homeostasis, aged murine macrophages exhibit dysregulated ceramide and phospholipid profiles compared to young macrophages. Of translational relevance, upregulation of microRNA-150 in

135

human peripheral blood mononuclear cells was also significantly associated with increased odds of AMD, even after controlling for age and gender. I generated novel insights into human disease by showing that microRNA-150 directly targets stearoyl-CoA desaturase-2 (*Scd2*), which coordinates macrophage-mediated inflammation and pathologic angiogenesis, as seen in AMD, in a vascular endothelial growth factor (VEGF)-independent manner.

Future studies will examine the molecular mechanism by which *Scd2* regulates macrophage inflammation. These are the topics of ongoing experimentation in the Apte Lab. Finally, although our human data significantly strengthen the translational relevance of our findings, additional studies are necessary to validate our results and should incorporate and control for other covariates, including but not limited to known risk factors of AMD. In particular, the collection of longitudinal data may provide further insight into whether oxysterols and/or microRNA-150 may predict risk of AMD progression. These findings would be highly valuable to guide clinical decision-making and improve the care clinicians can offer to patients.

5.3   Conclusions

Retinal degenerative diseases are a major cause of morbidity in the modern world. Visual impairment significantly diminishes the quality of life of patients. A significant challenge in preventing blindness caused by retinal diseases is the genetic and phenotypic heterogeneity of the diseases and a variable understanding of disease pathogenesis. This limited understanding has led to either the widespread use of drugs that treat disease manifestations in relatively late phases of the natural history rather than the underlying cause or, in many instances, a complete lack of treatment options altogether. Indeed, more research is necessary to identify novel therapeutics for early and targeted intervention. My thesis work advances our understanding of

136

the pathophysiology underlying photoreceptor neurodegeneration in diverse retinal degenerative diseases and cellular pathways that contribute to the transition from early AMD to wet AMD. Ultimately, these findings may lead to new therapeutic approaches for these diverse diseases and, perhaps, to the development of biomarkers that can be used to monitor disease progression.

References

Agarwal, V., Bell, G.W., Nam, J.W., and Bartel, D.P. (2015). Predicting effective microRNA target sites in mammalian mRNAs. eLife *4*.

Age-Related Eye Disease Study Research, G. (2001). A Randomized, Placebo-Controlled, Clinical Trial of High-Dose Supplementation With Vitamins C and E, Beta Carotene, and Zinc for Age-Related Macular Degeneration and Vision Loss: AREDS Report No. 8. Archives of ophthalmology *119*, 1417-1436.

Ait-Ali, N., Fridlich, R., Millet-Puel, G., Clerin, E., Delalande, F., Jaillard, C., Blond, F., Perrocheau, L., Reichman, S., Byrne, L.C.*, et al.* (2015). Rod-derived cone viability factor promotes cone survival by stimulating aerobic glycolysis. Cell *161*, 817-832.

Alano, C.C., Garnier, P., Ying, W., Higashi, Y., Kauppinen, T.M., and Swanson, R.A. (2010). NAD+ depletion is necessary and sufficient for poly(ADP-ribose) polymerase-1-mediated neuronal death. The Journal of neuroscience : the official journal of the Society for Neuroscience *30*, 2967-2978.

Ames, A., 3rd, Li, Y.Y., Heher, E.C., and Kimble, C.R. (1992). Energy metabolism of rabbit retina as related to function: high cost of Na+ transport. The Journal of neuroscience : the official journal of the Society for Neuroscience *12*, 840-853.

Apte, R.S. (2010). Regulation of angiogenesis by macrophages. Adv Exp Med Biol *664*, 15-19.

Apte, R.S. (2016). Targeting Tissue Lipids in Age-related Macular Degeneration. EBioMedicine *5*, 26-27.

Apte, R.S., Richter, J., Herndon, J., and Ferguson, T.A. (2006). Macrophages inhibit neovascularization in a murine model of age-related macular degeneration. PLoS medicine *3*, e310.

Astuti, G.D., Bertelsen, M., Preising, M.N., Ajmal, M., Lorenz, B., Faradz, S.M., Qamar, R., Collin, R.W., Rosenberg, T., and Cremers, F.P. (2015). Comprehensive genotyping reveals RPE65 as the most frequently mutated gene in Leber congenital amaurosis in Denmark. European journal of human genetics : EJHG.

Bai, S., and Sheline, C.T. (2013). NAD(+) maintenance attenuates light induced photoreceptor degeneration. Experimental eye research *108*, 76-83.

Bakondi, B., Lv, W., Lu, B., Jones, M.K., Tsai, Y., Kim, K.J., Levy, R., Akhtar, A.A., Breunig, J.J., Svendsen, C.N.*, et al.* (2016). In Vivo CRISPR/Cas9 Gene Editing Corrects Retinal Dystrophy in the S334ter-3 Rat Model of Autosomal Dominant Retinitis Pigmentosa. Molecular therapy : the journal of the American Society of Gene Therapy *24*, 556-563.

Betel, D., Wilson, M., Gabow, A., Marks, D.S., and Sander, C. (2008). The microRNA.org resource: targets and expression. Nucleic acids research *36*, D149-153.

Bhisitkul, R.B., Mendes, T.S., Rofagha, S., Enanoria, W., Boyer, D.S., Sadda, S.R., and Zhang, K. (2015). Macular atrophy progression and 7-year vision outcomes in subjects from the ANCHOR, MARINA, and HORIZON studies: the SEVEN-UP study. American journal of ophthalmology *159*, 915-924.e912.

Brown, K.D., Maqsood, S., Huang, J.Y., Pan, Y., Harkcom, W., Li, W., Sauve, A., Verdin, E., and Jaffrey, S.R. (2014). Activation of SIRT3 by the NAD(+) precursor nicotinamide riboside protects from noise-induced hearing loss. Cell metabolism *20*, 1059-1068.

Burgess, S., and Davey Smith, G. (2017). Mendelian Randomization Implicates High-Density Lipoprotein Cholesterol-Associated Mechanisms in Etiology of Age-Related Macular Degeneration. Ophthalmology.

Burnight, E.R., Gupta, M., Wiley, L.A., Anfinson, K.R., Tran, A., Triboulet, R., Hoffmann, J.M., Klaahsen, D.L., Andorf, J.L., Jiao, C.*, et al.* (2017). Using CRISPR-Cas9 to Generate Gene-Corrected Autologous iPSCs for the Treatment of Inherited Retinal Degeneration. Molecular therapy : the journal of the American Society of Gene Therapy *25*, 1999-2013.

Canto, C., Houtkooper, R.H., Pirinen, E., Youn, D.Y., Oosterveer, M.H., Cen, Y., Fernandez-Marcos, P.J., Yamamoto, H., Andreux, P.A., Cettour-Rose, P.*, et al.* (2012). The NAD(+) precursor nicotinamide riboside enhances oxidative metabolism and protects against high-fat diet-induced obesity. Cell metabolism *15*, 838-847.

Chakravarthy, M.V., Pan, Z., Zhu, Y., Tordjman, K., Schneider, J.G., Coleman, T., Turk, J., and Semenkovich, C.F. (2005). "New" hepatic fat activates PPARalpha to maintain glucose, lipid, and cholesterol homeostasis. Cell metabolism *1*, 309-322.

Chang, R.C., Shi, L., Huang, C.C., Kim, A.J., Ko, M.L., Zhou, B., and Ko, G.Y. (2015). High-Fat Diet-Induced Retinal Dysfunction. Investigative ophthalmology & visual science *56*, 2367-2380.

Chaumet-Riffaud, A.E., Chaumet-Riffaud, P., Cariou, A., Devisme, C., Audo, I., Sahel, J.A., and Mohand-Said, S. (2017). Impact of Retinitis Pigmentosa on Quality of Life, Mental Health, and Employment Among Young Adults. American journal of ophthalmology *177*, 169-174.

Chiang, P.W., Wang, J., Chen, Y., Fu, Q., Zhong, J., Yi, X., Wu, R., Gan, H., Shi, Y., Barnett, C.*, et al.* (2012). Exome sequencing identifies NMNAT1 mutations as a cause of Leber congenital amaurosis. Nat Genet *44*, 972-974.

Chinetti-Gbaguidi, G., Colin, S., and Staels, B. (2015). Macrophage subsets in atherosclerosis. Nature reviews Cardiology *12*, 10-17.

Clausen, B.E., Burkhardt, C., Reith, W., Renkawitz, R., and Forster, I. (1999). Conditional gene targeting in macrophages and granulocytes using LysMcre mice. Transgenic research *8*, 265-277.

Clemons, T.E., Milton, R.C., Klein, R., Seddon, J.M., and Ferris, F.L., 3rd (2005). Risk factors for the incidence of Advanced Age-Related Macular Degeneration in the Age-Related Eye Disease Study (AREDS) AREDS report no. 19. Ophthalmology *112*, 533-539.

Coupland, S.G. (1987). A comparison of oscillatory potential and pattern electroretinogram measures in diabetic retinopathy. Documenta ophthalmologica Advances in ophthalmology *66*, 207-218.

Crabb, J.W., Miyagi, M., Gu, X., Shadrach, K., West, K.A., Sakaguchi, H., Kamei, M., Hasan, A., Yan, L., Rayborn, M.E.*, et al.* (2002). Drusen proteome analysis: an approach to the etiology of age-related macular degeneration. Proceedings of the National Academy of Sciences of the United States of America *99*, 14682-14687.

Curcio, C.A., Johnson, M., Huang, J.D., and Rudolf, M. (2009). Aging, age-related macular degeneration, and the response-to-retention of apolipoprotein B-containing lipoproteins. Progress in retinal and eye research *28*, 393-422.

Curcio, C.A., Medeiros, N.E., and Millican, C.L. (1996). Photoreceptor loss in age-related macular degeneration. Investigative ophthalmology & visual science *37*, 1236-1249.

Datta, S., Cano, M., Ebrahimi, K., Wang, L., and Handa, J.T. (2017). The impact of oxidative stress and inflammation on RPE degeneration in non-neovascular AMD. Progress in retinal and eye research.

Dong, Z., Noda, K., Kanda, A., Fukuhara, J., Ando, R., Murata, M., Saito, W., Hagiwara, M., and Ishida, S. (2013). Specific inhibition of serine/arginine-rich protein kinase attenuates choroidal neovascularization. Molecular vision *19*, 536-543.

Du, J., Zhou, Y., Su, X., Yu, J.J., Khan, S., Jiang, H., Kim, J., Woo, J., Kim, J.H., Choi, B.H.*, et al.* (2011). Sirt5 is a NAD-dependent protein lysine demalonylase and desuccinylase. Science *334*, 806-809.

Du, Y., Veenstra, A., Palczewski, K., and Kern, T.S. (2013). Photoreceptor cells are major contributors to diabetes-induced oxidative stress and local inflammation in the retina. Proceedings of the National Academy of Sciences of the United States of America *110*, 16586-16591.

Espinosa-Heidmann, D.G., Suner, I.J., Hernandez, E.P., Monroy, D., Csaky, K.G., and Cousins, S.W. (2003). Macrophage depletion diminishes lesion size and severity in experimental choroidal neovascularization. Investigative ophthalmology & visual science *44*, 3586-3592.

Fadini, G.P., Simoni, F., Cappellari, R., Vitturi, N., Galasso, S., Vigili de Kreutzenberg, S., Previato, L., and Avogaro, A. (2014). Pro-inflammatory monocyte-macrophage polarization imbalance in human hypercholesterolemia and atherosclerosis. Atherosclerosis *237*, 805-808.

Falk, M.J., Zhang, Q., Nakamaru-Ogiso, E., Kannabiran, C., Fonseca-Kelly, Z., Chakarova, C., Audo, I., Mackay, D.S., Zeitz, C., Borman, A.D.*, et al.* (2012). NMNAT1 mutations cause Leber congenital amaurosis. Nature genetics *44*, 1040-1045.

Faul, F., Erdfelder, E., Lang, A.G., and Buchner, A. (2007). G*Power 3: a flexible statistical power analysis program for the social, behavioral, and biomedical sciences. Behavior research methods *39*, 175-191.

Fenwick, E.K., Ong, P.G., Man, R.E., Cheng, C.Y., Sabanayagam, C., Wong, T.Y., and Lamoureux, E.L. (2016). Association of Vision Impairment and Major Eye Diseases With Mobility and Independence in a Chinese Population. JAMA ophthalmology *134*, 1087-1093.

Ferris, F.L., 3rd, Fine, S.L., and Hyman, L. (1984). Age-related macular degeneration and blindness due to neovascular maculopathy. Archives of ophthalmology (Chicago, Ill : 1960) *102*, 1640-1642.

Ferris, F.L., Davis, M.D., Clemons, T.E., Lee, L.Y., Chew, E.Y., Lindblad, A.S., Milton, R.C., Bressler, S.B., and Klein, R. (2005). A simplified severity scale for age-related macular degeneration: AREDS Report No. 18. Archives of ophthalmology (Chicago, Ill : 1960) *123*, 1570-1574.

Frezza, C., Cipolat, S., and Scorrano, L. (2007). Organelle isolation: functional mitochondria from mouse liver, muscle and cultured fibroblasts. Nature protocols *2*, 287-295.

Fu, Y., and Yau, K.W. (2007). Phototransduction in mouse rods and cones. Pflugers Arch *454*, 805-819.

Garten, A., Petzold, S., Korner, A., Imai, S., and Kiess, W. (2009). Nampt: linking NAD biology, metabolism and cancer. Trends in endocrinology and metabolism: TEM *20*, 130-138.

141

Gehlbach, P., Li, T., and Hatef, E. (2016). Statins for age-related macular degeneration. The Cochrane database of systematic reviews, Cd006927.

Gerdts, J., Brace, E.J., Sasaki, Y., DiAntonio, A., and Milbrandt, J. (2015). SARM1 activation triggers axon degeneration locally via NAD(+) destruction. Science (New York, NY) *348*, 453-457.

Gerrity, R.G. (1981). The role of the monocyte in atherogenesis: I. Transition of blood-borne monocytes into foam cells in fatty lesions. The American journal of pathology *103*, 181-190.

Gerrity, R.G., Naito, H.K., Richardson, M., and Schwartz, C.J. (1979). Dietary induced atherogenesis in swine. Morphology of the intima in prelesion stages. The American journal of pathology *95*, 775-792.

Grassmann, F., Schoenberger, P.G., Brandl, C., Schick, T., Hasler, D., Meister, G., Fleckenstein, M., Lindner, M., Helbig, H., Fauser, S.*, et al.* (2014). A circulating microrna profile is associated with late-stage neovascular age-related macular degeneration. PloS one *9*, e107461.

Grimm, C., and Reme, C.E. (2013). Light damage as a model of retinal degeneration. Methods Mol Biol *935*, 87-97.

Grunin, M., Hagbi-Levi, S., Rinsky, B., Smith, Y., and Chowers, I. (2016). Transcriptome Analysis on Monocytes from Patients with Neovascular Age-Related Macular Degeneration. Scientific reports *6*, 29046.

Hagbi-Levi, S., Grunin, M., Jaouni, T., Tiosano, L., Rinsky, B., Elbaz-Hayoun, S., Peled, A., and Chowers, I. (2017). Proangiogenic characteristics of activated macrophages from patients with age-related macular degeneration. Neurobiology of aging *51*, 71-82.

Hageman, G.S., Anderson, D.H., Johnson, L.V., Hancox, L.S., Taiber, A.J., Hardisty, L.I., Hageman, J.L., Stockman, H.A., Borchardt, J.D., Gehrs, K.M.*, et al.* (2005). A common haplotype in the complement regulatory gene factor H (HF1/CFH) predisposes individuals to age-related macular degeneration. Proceedings of the National Academy of Sciences of the United States of America *102*, 7227-7232.

Hall, N.F., Gale, C.R., Syddall, H., Phillips, D.I., and Martyn, C.N. (2001). Risk of macular degeneration in users of statins: cross sectional study. BMJ (Clinical research ed) *323*, 375-376.

Haller, J.A. (2013). Current anti-vascular endothelial growth factor dosing regimens: benefits and burden. Ophthalmology *120*, S3-7.

Harrison, W.W., Bearse, M.A., Jr., Ng, J.S., Jewell, N.P., Barez, S., Burger, D., Schneck, M.E., and Adams, A.J. (2011). Multifocal electroretinograms predict onset of diabetic retinopathy in adult patients with diabetes. Investigative ophthalmology & visual science *52*, 772-777.

Hartong, D.T., Berson, E.L., and Dryja, T.P. (2006). Retinitis pigmentosa. Lancet *368*, 1795-1809.

Hartong, D.T., Dange, M., McGee, T.L., Berson, E.L., Dryja, T.P., and Colman, R.F. (2008). Insights from retinitis pigmentosa into the roles of isocitrate dehydrogenases in the Krebs cycle. Nature genetics *40*, 1230-1234.

Hashimoto, D., Chow, A., Noizat, C., Teo, P., Beasley, M.B., Leboeuf, M., Becker, C.D., See, P., Price, J., Lucas, D.*, et al.* (2013). Tissue-resident macrophages self-maintain locally throughout adult life with minimal contribution from circulating monocytes. Immunity *38*, 792-804.

Hebert, A.S., Dittenhafer-Reed, K.E., Yu, W., Bailey, D.J., Selen, E.S., Boersma, M.D., Carson, J.J., Tonelli, M., Balloon, A.J., Higbee, A.J.*, et al.* (2013). Calorie restriction and SIRT3 trigger global reprogramming of the mitochondrial protein acetylome. Molecular cell *49*, 186-199.

Heesterbeek, T.J., van der Aa, H.P.A., van Rens, G., Twisk, J.W.R., and van Nispen, R.M.A. (2017). The incidence and predictors of depressive and anxiety symptoms in older adults with vision impairment: a longitudinal prospective cohort study. Ophthalmic & physiological optics : the journal of the British College of Ophthalmic Opticians (Optometrists) *37*, 385-398.

Heinz, R.E., Rudolph, M.C., Ramanathan, P., Spoelstra, N.S., Butterfield, K.T., Webb, P.G., Babbs, B.L., Gao, H., Chen, S., Gordon, M.A.*, et al.* (2016). Constitutive expression of microRNA-150 in mammary epithelium suppresses secretory activation and impairs de novo lipogenesis. Development (Cambridge, England) *143*, 4236-4248.

Hennig, A.K., Peng, G.H., and Chen, S. (2013). Transcription coactivators p300 and CBP are necessary for photoreceptor-specific chromatin organization and gene expression. PLoS One *8*, e69721.

Hirschey, M.D., Shimazu, T., Jing, E., Grueter, C.A., Collins, A.M., Aouizerat, B., Stancakova, A., Goetzman, E., Lam, M.M., Schwer, B.*, et al.* (2011). SIRT3 deficiency and mitochondrial protein hyperacetylation accelerate the development of the metabolic syndrome. Molecular cell *44*, 177-190.

Huang, S.C., Everts, B., Ivanova, Y., O'Sullivan, D., Nascimento, M., Smith, A.M., Beatty, W., Love-Gregory, L., Lam, W.Y., O'Neill, C.M.*, et al.* (2014). Cell-intrinsic lysosomal lipolysis is essential for alternative activation of macrophages. Nature immunology *15*, 846-855.

143

Imai, S., and Yoshino, J. (2013). The importance of NAMPT/NAD/SIRT1 in the systemic regulation of metabolism and ageing. Diabetes, obesity & metabolism *15 Suppl 3*, 26-33.

Imai, S.I., and Guarente, L. (2014). NAD and sirtuins in aging and disease. Trends Cell Biol.

Indaram, M., Ma, W., Zhao, L., Fariss, R.N., Rodriguez, I.R., and Wong, W.T. (2015). 7-Ketocholesterol increases retinal microglial migration, activation, and angiogenicity: a potential pathogenic mechanism underlying age-related macular degeneration. Scientific reports *5*, 9144.

Inoue, M., Yamane, S., Sato, S., Sakamaki, K., Arakawa, A., and Kadonosono, K. (2016). Comparison of Time to Retreatment and Visual Function Between Ranibizumab and Aflibercept in Age-Related Macular Degeneration. American journal of ophthalmology *169*, 95-103.

Ishikawa, T., Ayaori, M., Uto-Kondo, H., Nakajima, T., Mutoh, M., and Ikewaki, K. (2015). High-density lipoprotein cholesterol efflux capacity as a relevant predictor of atherosclerotic coronary disease. Atherosclerosis *242*, 318-322.

Jaliffa, C., Ameqrane, I., Dansault, A., Leemput, J., Vieira, V., Lacassagne, E., Provost, A., Bigot, K., Masson, C., Menasche, M.*, et al.* (2009). Sirt1 involvement in rd10 mouse retinal degeneration. Investigative ophthalmology & visual science *50*, 3562-3572.

Jiang, X., Sidhu, R., Mydock-McGrane, L., Hsu, F.F., Covey, D.F., Scherrer, D.E., Earley, B., Gale, S.E., Farhat, N.Y., Porter, F.D.*, et al.* (2016). Development of a bile acid-based newborn screen for Niemann-Pick disease type C. Science translational medicine *8*, 337ra363.

Jiang, X., Sidhu, R., Porter, F.D., Yanjanin, N.M., Speak, A.O., te Vruchte, D.T., Platt, F.M., Fujiwara, H., Scherrer, D.E., Zhang, J.*, et al.* (2011). A sensitive and specific LC-MS/MS method for rapid diagnosis of Niemann-Pick C1 disease from human plasma. Journal of lipid research *52*, 1435-1445.

Kelly, J., Ali Khan, A., Yin, J., Ferguson, T.A., and Apte, R.S. (2007). Senescence regulates macrophage activation and angiogenic fate at sites of tissue injury in mice. J Clin Invest *117*, 3421-3426.

Khalil, H., Tazi, M., Caution, K., Ahmed, A., Kanneganti, A., Assani, K., Kopp, B., Marsh, C., Dakhlallah, D., and Amer, A.O. (2016). Aging is associated with hypermethylation of autophagy genes in macrophages. Epigenetics *11*, 381-388.

Kim, J.H., Lee, D.W., Chang, Y.S., Kim, J.W., and Kim, C.G. (2016). Twelve-month outcomes of treatment using ranibizumab or aflibercept for neovascular age-related macular degeneration: a comparative study. Graefe's archive for clinical and experimental ophthalmology = Albrecht von Graefes Archiv fur klinische und experimentelle Ophthalmologie *254*, 2101-2109.

Klein, R., Peto, T., Bird, A., and Vannewkirk, M.R. (2004). The epidemiology of age-related macular degeneration. American journal of ophthalmology *137*, 486-495.

Koenekoop, R.K., Wang, H., Majewski, J., Wang, X., Lopez, I., Ren, H., Chen, Y., Li, Y., Fishman, G.A., Genead, M.*, et al.* (2012). Mutations in NMNAT1 cause Leber congenital amaurosis and identify a new disease pathway for retinal degeneration. Nature genetics *44*, 1035-1039.

Kolesnikov, A.V., Fan, J., Crouch, R.K., and Kefalov, V.J. (2010). Age-related deterioration of rod vision in mice. The Journal of neuroscience : the official journal of the Society for Neuroscience *30*, 11222-11231.

Kolesnikov, A.V., Tang, P.H., Parker, R.O., Crouch, R.K., and Kefalov, V.J. (2011). The mammalian cone visual cycle promotes rapid M/L-cone pigment regeneration independently of the interphotoreceptor retinoid-binding protein. The Journal of neuroscience : the official journal of the Society for Neuroscience *31*, 7900-7909.

Kooragayala, K., Gotoh, N., Cogliati, T., Nellissery, J., Kaden, T.R., French, S., Balaban, R., Li, W., Covian, R., and Swaroop, A. (2015). Quantification of Oxygen Consumption in Retina Ex Vivo Demonstrates Limited Reserve Capacity of Photoreceptor Mitochondria. Investigative ophthalmology & visual science *56*, 8428-8436.

Kramsch, D.M., Franzblau, C., and Hollander, W. (1971). The protein and lipid composition of arterial elastin and its relationship to lipid accumulation in the atherosclerotic plaque. The Journal of clinical investigation *50*, 1666-1677.

Krishnamurthy, J., Torrice, C., Ramsey, M.R., Kovalev, G.I., Al-Regaiey, K., Su, L., and Sharpless, N.E. (2004). Ink4a/Arf expression is a biomarker of aging. The Journal of clinical investigation *114*, 1299-1307.

Lai, K.K.Y., Kweon, S.M., Chi, F., Hwang, E., Kabe, Y., Higashiyama, R., Qin, L., Yan, R., Wu, R.P., Lai, K.*, et al.* (2017). Stearoyl-CoA Desaturase Promotes Liver Fibrosis and Tumor Development in Mice via a Wnt Positive-Signaling Loop by Stabilization of Low-Density Lipoprotein-Receptor-Related Proteins 5 and 6. Gastroenterology *152*, 1477-1491.

Laurent, G., German, N.J., Saha, A.K., de Boer, V.C., Davies, M., Koves, T.R., Dephoure, N., Fischer, F., Boanca, G., Vaitheesvaran, B.*, et al.* (2013). SIRT4 coordinates the balance between lipid synthesis and catabolism by repressing malonyl CoA decarboxylase. Molecular cell *50*, 686-698.

Le, Y.Z., Ash, J.D., Al-Ubaidi, M.R., Chen, Y., Ma, J.X., and Anderson, R.E. (2004). Targeted expression of Cre recombinase to cone photoreceptors in transgenic mice. Mol Vis *10*, 1011-1018.

Li, S., Chen, D., Sauve, Y., McCandless, J., Chen, Y.J., and Chen, C.K. (2005). Rhodopsin-iCre transgenic mouse line for Cre-mediated rod-specific gene targeting. Genesis *41*, 73-80.

Lin, J.B., Kubota, S., Ban, N., Yoshida, M., Santeford, A., Sene, A., Nakamura, R., Zapata, N., Kubota, M., Tsubota, K.*, et al.* (2016a). NAMPT-Mediated NAD(+) Biosynthesis Is Essential for Vision In Mice. Cell reports *17*, 69-85.

Lin, J.B., Tsubota, K., and Apte, R.S. (2016b). A glimpse at the aging eye. Npj Aging And Mechanisms Of Disease *2*, 16003.

Liu, C.H., Sun, Y., Li, J., Gong, Y., Tian, K.T., Evans, L.P., Morss, P.C., Fredrick, T.W., Saba, N.J., and Chen, J. (2015). Endothelial microRNA-150 is an intrinsic suppressor of pathologic ocular neovascularization. Proceedings of the National Academy of Sciences of the United States of America *112*, 12163-12168.

Lombard, D.B., Alt, F.W., Cheng, H.L., Bunkenborg, J., Streeper, R.S., Mostoslavsky, R., Kim, J., Yancopoulos, G., Valenzuela, D., Murphy, A.*, et al.* (2007). Mammalian Sir2 homolog SIRT3 regulates global mitochondrial lysine acetylation. Molecular and cellular biology *27*, 8807-8814.

Lopez-Otin, C., Blasco, M.A., Partridge, L., Serrano, M., and Kroemer, G. (2013). The hallmarks of aging. Cell *153*, 1194-1217.

Lv, Y.C., Tang, Y.Y., Peng, J., Zhao, G.J., Yang, J., Yao, F., Ouyang, X.P., He, P.P., Xie, W., Tan, Y.L.*, et al.* (2014). MicroRNA-19b promotes macrophage cholesterol accumulation and aortic atherosclerosis by targeting ATP-binding cassette transporter A1. Atherosclerosis *236*, 215-226.

Ma, W., and Wong, W.T. (2016). Aging Changes in Retinal Microglia and their Relevance to Age-related Retinal Disease. Advances in experimental medicine and biology *854*, 73-78.

MacLaren, R.E., Pearson, R.A., MacNeil, A., Douglas, R.H., Salt, T.E., Akimoto, M., Swaroop, A., Sowden, J.C., and Ali, R.R. (2006). Retinal repair by transplantation of photoreceptor precursors. Nature *444*, 203-207.

Malek, G., Johnson, L.V., Mace, B.E., Saloupis, P., Schmechel, D.E., Rickman, D.W., Toth, C.A., Sullivan, P.M., and Bowes Rickman, C. (2005). Apolipoprotein E allele-dependent pathogenesis: a model for age-related retinal degeneration. Proceedings of the National Academy of Sciences of the United States of America *102*, 11900-11905.

146

Mandai, M., Watanabe, A., Kurimoto, Y., Hirami, Y., Morinaga, C., Daimon, T., Fujihara, M., Akimaru, H., Sakai, N., Shibata, Y*., et al.* (2017). Autologous Induced Stem-Cell-Derived Retinal Cells for Macular Degeneration. The New England journal of medicine *376*, 1038-1046.

Masuda, M., Miyazaki-Anzai, S., Keenan, A.L., Okamura, K., Kendrick, J., Chonchol, M., Offermanns, S., Ntambi, J.M., Kuro, O.M., and Miyazaki, M. (2015). Saturated phosphatidic acids mediate saturated fatty acid-induced vascular calcification and lipotoxicity. The Journal of clinical investigation *125*, 4544-4558.

McLeod, D.S., Bhutto, I., Edwards, M.M., Silver, R.E., Seddon, J.M., and Lutty, G.A. (2016). Distribution and Quantification of Choroidal Macrophages in Human Eyes With Age-Related Macular Degeneration. Investigative ophthalmology & visual science *57*, 5843-5855.

Meiler, S., Baumer, Y., Toulmin, E., Seng, K., and Boisvert, W.A. (2015). MicroRNA 302a is a novel modulator of cholesterol homeostasis and atherosclerosis. Arteriosclerosis, thrombosis, and vascular biology *35*, 323-331.

Menard, C., Rezende, F.A., Miloudi, K., Wilson, A., Tetreault, N., Hardy, P., SanGiovanni, J.P., De Guire, V., and Sapieha, P. (2016). MicroRNA signatures in vitreous humour and plasma of patients with exudative AMD. Oncotarget *7*, 19171-19184.

Mills, K.F., Yoshida, S., Stein, L.R., Grozio, A., Kubota, S., Sasaki, Y., Redpath, P., Migaud, M.E., Apte, R.S., Uchida, K*., et al.* (2016). Long-Term Administration of Nicotinamide Mononucleotide Mitigates Age-Associated Physiological Decline in Mice. Cell metabolism *24*, 795-806.

Miranda, K.C., Huynh, T., Tay, Y., Ang, Y.S., Tam, W.L., Thomson, A.M., Lim, B., and Rigoutsos, I. (2006). A pattern-based method for the identification of MicroRNA binding sites and their corresponding heteroduplexes. Cell *126*, 1203-1217.

Miyazaki, M., Dobrzyn, A., Elias, P.M., and Ntambi, J.M. (2005). Stearoyl-CoA desaturase-2 gene expression is required for lipid synthesis during early skin and liver development. Proceedings of the National Academy of Sciences of the United States of America *102*, 12501-12506.

Mosser, D.M., and Edwards, J.P. (2008). Exploring the full spectrum of macrophage activation. Nature reviews Immunology *8*, 958-969.

Mouchiroud, L., Houtkooper, R.H., Moullan, N., Katsyuba, E., Ryu, D., Canto, C., Mottis, A., Jo, Y.S., Viswanathan, M., Schoonjans, K*., et al.* (2013). The NAD(+)/Sirtuin Pathway Modulates Longevity through Activation of Mitochondrial UPR and FOXO Signaling. Cell *154*, 430-441.

Mullins, R.F., Russell, S.R., Anderson, D.H., and Hageman, G.S. (2000). Drusen associated with aging and age-related macular degeneration contain proteins common to extracellular deposits associated with atherosclerosis, elastosis, amyloidosis, and dense deposit disease. FASEB journal : official publication of the Federation of American Societies for Experimental Biology *14*, 835-846.

Murray, P.J., Allen, J.E., Biswas, S.K., Fisher, E.A., Gilroy, D.W., Goerdt, S., Gordon, S., Hamilton, J.A., Ivashkiv, L.B., Lawrence, T.*, et al.* (2014). Macrophage activation and polarization: nomenclature and experimental guidelines. Immunity *41*, 14-20.

Nakahata, Y., Sahar, S., Astarita, G., Kaluzova, M., and Sassone-Corsi, P. (2009). Circadian control of the NAD+ salvage pathway by CLOCK-SIRT1. Science (New York, NY) *324*, 654-657.

Nakamura, R., Sene, A., Santeford, A., Gdoura, A., Kubota, S., Zapata, N., and Apte, R.S. (2015). IL10-driven STAT3 signalling in senescent macrophages promotes pathological eye angiogenesis. Nature communications *6*, 7847.

Neale, B.M., Fagerness, J., Reynolds, R., Sobrin, L., Parker, M., Raychaudhuri, S., Tan, P.L., Oh, E.C., Merriam, J.E., Souied, E.*, et al.* (2010). Genome-wide association study of advanced age-related macular degeneration identifies a role of the hepatic lipase gene (LIPC). Proceedings of the National Academy of Sciences of the United States of America *107*, 7395-7400.

Nielsen, G.P., Stemmer-Rachamimov, A.O., Shaw, J., Roy, J.E., Koh, J., and Louis, D.N. (1999). Immunohistochemical survey of p16INK4A expression in normal human adult and infant tissues. Laboratory investigation; a journal of technical methods and pathology *79*, 1137-1143.

Nishida, Y., Rardin, M.J., Carrico, C., He, W., Sahu, A.K., Gut, P., Najjar, R., Fitch, M., Hellerstein, M., Gibson, B.W.*, et al.* (2015). SIRT5 Regulates both Cytosolic and Mitochondrial Protein Malonylation with Glycolysis as a Major Target. Molecular cell *59*, 321-332.

Okawa, H., Sampath, A.P., Laughlin, S.B., and Fain, G.L. (2008). ATP consumption by mammalian rod photoreceptors in darkness and in light. Current biology : CB *18*, 1917-1921.

Papanicolaou, K.N., O'Rourke, B., and Foster, D.B. (2014). Metabolism leaves its mark on the powerhouse: recent progress in post-translational modifications of lysine in mitochondria. Front Physiol *5*, 301.

Paraskevopoulou, M.D., Georgakilas, G., Kostoulas, N., Vlachos, I.S., Vergoulis, T., Reczko, M., Filippidis, C., Dalamagas, T., and Hatzigeorgiou, A.G. (2013). DIANA-microT web server v5.0: service integration into miRNA functional analysis workflows. Nucleic acids research *41*, W169-173.

Parihar, P., Solanki, I., Mansuri, M.L., and Parihar, M.S. (2015). Mitochondrial sirtuins: emerging roles in metabolic regulations, energy homeostasis and diseases. Experimental gerontology *61*, 130-141.

Park, J., Chen, Y., Tishkoff, D.X., Peng, C., Tan, M., Dai, L., Xie, Z., Zhang, Y., Zwaans, B.M., Skinner, M.E*., et al.* (2013). SIRT5-mediated lysine desuccinylation impacts diverse metabolic pathways. Molecular cell *50*, 919-930.

Pearson, R.A., Barber, A.C., Rizzi, M., Hippert, C., Xue, T., West, E.L., Duran, Y., Smith, A.J., Chuang, J.Z., Azam, S.A*., et al.* (2012). Restoration of vision after transplantation of photoreceptors. Nature *485*, 99-103.

Pearson, R.A., Gonzalez-Cordero, A., West, E.L., Ribeiro, J.R., Aghaizu, N., Goh, D., Sampson, R.D., Georgiadis, A., Waldron, P.V., Duran, Y*., et al.* (2016). Donor and host photoreceptors engage in material transfer following transplantation of post-mitotic photoreceptor precursors. Nature communications *7*, 13029.

Peled, M., and Fisher, E.A. (2014). Dynamic Aspects of Macrophage Polarization during Atherosclerosis Progression and Regression. Frontiers in immunology *5*, 579.

Perrault, I., Hanein, S., Zanlonghi, X., Serre, V., Nicouleau, M., Defoort-Delhemmes, S., Delphin, N., Fares-Taie, L., Gerber, S., Xerri, O*., et al.* (2012). Mutations in NMNAT1 cause Leber congenital amaurosis with early-onset severe macular and optic atrophy. Nat Genet *44*, 975-977.

Perron, N.R., Beeson, C., and Rohrer, B. (2013). Early alterations in mitochondrial reserve capacity; a means to predict subsequent photoreceptor cell death. Journal of bioenergetics and biomembranes *45*, 101-109.

Poli, G., Biasi, F., and Leonarduzzi, G. (2013). Oxysterols in the pathogenesis of major chronic diseases. Redox biology *1*, 125-130.

Porter, F.D., Scherrer, D.E., Lanier, M.H., Langmade, S.J., Molugu, V., Gale, S.E., Olzeski, D., Sidhu, R., Dietzen, D.J., Fu, R*., et al.* (2010). Cholesterol oxidation products are sensitive and specific blood-based biomarkers for Niemann-Pick C1 disease. Science translational medicine *2*, 56ra81.

Rajagopal, R., Bligard, G.W., Zhang, S., Yin, L., Lukasiewicz, P., and Semenkovich, C.F. (2016). Functional Deficits Precede Structural Lesions in Mice With High-Fat Diet-Induced Diabetic Retinopathy. Diabetes *65*, 1072-1084.

149

Ramsey, K.M., Mills, K.F., Satoh, A., and Imai, S. (2008). Age-associated loss of Sirt1-mediated enhancement of glucose-stimulated insulin secretion in beta cell-specific Sirt1-overexpressing (BESTO) mice. Aging cell *7*, 78-88.

Ramsey, K.M., Yoshino, J., Brace, C.S., Abrassart, D., Kobayashi, Y., Marcheva, B., Hong, H.K., Chong, J.L., Buhr, E.D., Lee, C.*, et al.* (2009). Circadian clock feedback cycle through NAMPT-mediated NAD+ biosynthesis. Science (New York, NY) *324*, 651-654.

Randle, D.H., Zindy, F., Sherr, C.J., and Roussel, M.F. (2001). Differential effects of p19Arf and p16Ink4a loss on senescence of murine bone marrow-derived preB cells and macrophages. Proceedings of the National Academy of Sciences *98*, 9654-9659.

Rardin, M.J., He, W., Nishida, Y., Newman, J.C., Carrico, C., Danielson, S.R., Guo, A., Gut, P., Sahu, A.K., Li, B.*, et al.* (2013a). SIRT5 regulates the mitochondrial lysine succinylome and metabolic networks. Cell metabolism *18*, 920-933.

Rardin, M.J., Newman, J.C., Held, J.M., Cusack, M.P., Sorensen, D.J., Li, B., Schilling, B., Mooney, S.D., Kahn, C.R., Verdin, E.*, et al.* (2013b). Label-free quantitative proteomics of the lysine acetylome in mitochondria identifies substrates of SIRT3 in metabolic pathways. Proceedings of the National Academy of Sciences of the United States of America *110*, 6601-6606.

Ratajczak, J., Joffraud, M., Trammell, S.A., Ras, R., Canela, N., Boutant, M., Kulkarni, S.S., Rodrigues, M., Redpath, P., Migaud, M.E.*, et al.* (2016). NRK1 controls nicotinamide mononucleotide and nicotinamide riboside metabolism in mammalian cells. Nature communications *7*, 13103.

Rayner, K.J., Sheedy, F.J., Esau, C.C., Hussain, F.N., Temel, R.E., Parathath, S., van Gils, J.M., Rayner, A.J., Chang, A.N., Suarez, Y.*, et al.* (2011). Antagonism of miR-33 in mice promotes reverse cholesterol transport and regression of atherosclerosis. The Journal of clinical investigation *121*, 2921-2931.

Revollo, J.R., Korner, A., Mills, K.F., Satoh, A., Wang, T., Garten, A., Dasgupta, B., Sasaki, Y., Wolberger, C., Townsend, R.R.*, et al.* (2007). Nampt/PBEF/Visfatin regulates insulin secretion in beta cells as a systemic NAD biosynthetic enzyme. Cell metabolism *6*, 363-375.

Ritchie, M.E., Phipson, B., Wu, D., Hu, Y., Law, C.W., Shi, W., and Smyth, G.K. (2015). limma powers differential expression analyses for RNA-sequencing and microarray studies. Nucleic acids research *43*, e47.

Rongvaux, A., Galli, M., Denanglaire, S., Van Gool, F., Dreze, P.L., Szpirer, C., Bureau, F., Andris, F., and Leo, O. (2008). Nicotinamide phosphoribosyl transferase/pre-B cell colony-

enhancing factor/visfatin is required for lymphocyte development and cellular resistance to genotoxic stress. J Immunol *181*, 4685-4695.

Russell, S., Bennett, J., Wellman, J.A., Chung, D.C., Yu, Z.F., Tillman, A., Wittes, J., Pappas, J., Elci, O., McCague, S*., et al.* (2017). Efficacy and safety of voretigene neparvovec (AAV2-hRPE65v2) in patients with RPE65-mediated inherited retinal dystrophy: a randomised, controlled, open-label, phase 3 trial. Lancet (London, England) *390*, 849-860.

Sakurai, E., Anand, A., Ambati, B.K., van Rooijen, N., and Ambati, J. (2003). Macrophage depletion inhibits experimental choroidal neovascularization. Investigative ophthalmology *&* visual science *44*, 3578-3585.

Samuels, I.S., Bell, B.A., Pereira, A., Saxon, J., and Peachey, N.S. (2015). Early retinal pigment epithelium dysfunction is concomitant with hyperglycemia in mouse models of type 1 and type 2 diabetes. Journal of neurophysiology *113*, 1085-1099.

Santos-Ferreira, T., Postel, K., Stutzki, H., Kurth, T., Zeck, G., and Ader, M. (2015). Daylight vision repair by cell transplantation. Stem cells (Dayton, Ohio) *33*, 79-90.

Sarwar, S., Clearfield, E., Soliman, M.K., Sadiq, M.A., Baldwin, A.J., Hanout, M., Agarwal, A., Sepah, Y.J., Do, D.V., and Nguyen, Q.D. (2016). Aflibercept for neovascular age-related macular degeneration. The Cochrane database of systematic reviews *2*, Cd011346.

Sasaki, Y., Margolin, Z., Borgo, B., Havranek, J.J., and Milbrandt, J. (2015). Characterization of Leber Congenital Amaurosis-associated NMNAT1 Mutants. The Journal of biological chemistry *290*, 17228-17238.

Satoh, A., and Imai, S. (2014). Systemic regulation of mammalian ageing and longevity by brain sirtuins. Nat Commun *5*, 4211.

Satoh, S., Iijima, H., Imai, M., Abe, K., and Shibuya, T. (1994). Photopic electroretinogram implicit time in diabetic retinopathy. Japanese journal of ophthalmology *38*, 178-184.

Schilling, J.D., Machkovech, H.M., He, L., Sidhu, R., Fujiwara, H., Weber, K., Ory, D.S., and Schaffer, J.E. (2013). Palmitate and lipopolysaccharide trigger synergistic ceramide production in primary macrophages. The Journal of biological chemistry *288*, 2923-2932.

Schimel, A.M., Abraham, L., Cox, D., Sene, A., Kraus, C., Dace, D.S., Ercal, N., and Apte, R.S. (2011). N-acetylcysteine amide (NACA) prevents retinal degeneration by up-regulating reduced glutathione production and reversing lipid peroxidation. The American journal of pathology *178*, 2032-2043.

151

Schwartz, S.D., Regillo, C.D., Lam, B.L., Eliott, D., Rosenfeld, P.J., Gregori, N.Z., Hubschman, J.P., Davis, J.L., Heilwell, G., Spirn, M*., et al.* (2015). Human embryonic stem cell-derived retinal pigment epithelium in patients with age-related macular degeneration and Stargardt's macular dystrophy: follow-up of two open-label phase 1/2 studies. Lancet (London, England) *385*, 509-516.

Schwartz, S.D., Tan, G., Hosseini, H., and Nagiel, A. (2016). Subretinal Transplantation of Embryonic Stem Cell-Derived Retinal Pigment Epithelium for the Treatment of Macular Degeneration: An Assessment at 4 Years. Investigative ophthalmology & visual science *57*, ORSFc1-9.

Schwer, B., Eckersdorff, M., Li, Y., Silva, J.C., Fermin, D., Kurtev, M.V., Giallourakis, C., Comb, M.J., Alt, F.W., and Lombard, D.B. (2009). Calorie restriction alters mitochondrial protein acetylation. Aging cell *8*, 604-606.

Sene, A., and Apte, R.S. (2014). Eyeballing cholesterol efflux and macrophage function in disease pathogenesis. Trends Endocrinol Metab *25*, 107-114.

Sene, A., Chin-Yee, D., and Apte, R.S. (2015). Seeing through VEGF: innate and adaptive immunity in pathological angiogenesis in the eye. Trends in molecular medicine *21*, 43-51.

Sene, A., Khan, A.A., Cox, D., Nakamura, R.E., Santeford, A., Kim, B.M., Sidhu, R., Onken, M.D., Harbour, J.W., Hagbi-Levi, S*., et al.* (2013). Impaired cholesterol efflux in senescent macrophages promotes age-related macular degeneration. Cell metabolism *17*, 549-561.

Shen, J., Yang, X., Xie, B., Chen, Y., Swaim, M., Hackett, S.F., and Campochiaro, P.A. (2008). MicroRNAs regulate ocular neovascularization. Molecular therapy : the journal of the American Society of Gene Therapy *16*, 1208-1216.

Sica, A., and Mantovani, A. (2012). Macrophage plasticity and polarization: in vivo veritas. The Journal of clinical investigation *122*, 787-795.

Silberman, D.M., Ross, K., Sande, P.H., Kubota, S., Ramaswamy, S., Apte, R.S., and Mostoslavsky, R. (2014). SIRT6 is required for normal retinal function. PloS one *9*, e98831.

Sol, E.M., Wagner, S.A., Weinert, B.T., Kumar, A., Kim, H.S., Deng, C.X., and Choudhary, C. (2012). Proteomic investigations of lysine acetylation identify diverse substrates of mitochondrial deacetylase sirt3. PLoS One *7*, e50545.

Spann, N.J., and Glass, C.K. (2013). Sterols and oxysterols in immune cell function. Nature immunology *14*, 893-900.

Stein, L.R., and Imai, S. (2014). Specific ablation of Nampt in adult neural stem cells recapitulates their functional defects during aging. The EMBO journal *33*, 1321-1340.

Stein, L.R., Wozniak, D.F., Dearborn, J.T., Kubota, S., Apte, R.S., Izumi, Y., Zorumski, C.F., and Imai, S. (2014). Expression of Nampt in hippocampal and cortical excitatory neurons is critical for cognitive function. The Journal of neuroscience : the official journal of the Society for Neuroscience *34*, 5800-5815.

Still, A.J., Floyd, B.J., Hebert, A.S., Bingman, C.A., Carson, J.J., Gunderson, D.R., Dolan, B.K., Grimsrud, P.A., Dittenhafer-Reed, K.E., Stapleton, D.S.*, et al.* (2013). Quantification of mitochondrial acetylation dynamics highlights prominent sites of metabolic regulation. The Journal of biological chemistry *288*, 26209-26219.

Tan, E., Ding, X.Q., Saadi, A., Agarwal, N., Naash, M.I., and Al-Ubaidi, M.R. (2004). Expression of cone-photoreceptor-specific antigens in a cell line derived from retinal tumors in transgenic mice. Investigative ophthalmology & visual science *45*, 764-768.

Tan, M., Peng, C., Anderson, K.A., Chhoy, P., Xie, Z., Dai, L., Park, J., Chen, Y., Huang, H., Zhang, Y.*, et al.* (2014). Lysine glutarylation is a protein posttranslational modification regulated by SIRT5. Cell metabolism *19*, 605-617.

Tarasov, K., Ekroos, K., Suoniemi, M., Kauhanen, D., Sylvänne, T., Hurme, R., Gouni-Berthold, I., Berthold, H.K., Kleber, M.E., Laaksonen, R.*, et al.* (2014). Molecular Lipids Identify Cardiovascular Risk and Are Efficiently Lowered by Simvastatin and PCSK9 Deficiency. The Journal of Clinical Endocrinology and Metabolism *99*, E45-E52.

Tavakoli, S., Zamora, D., Ullevig, S., and Asmis, R. (2013). Bioenergetic profiles diverge during macrophage polarization: implications for the interpretation of 18F-FDG PET imaging of atherosclerosis. Journal of nuclear medicine : official publication, Society of Nuclear Medicine *54*, 1661-1667.

Tomany, S.C., Wang, J.J., Van Leeuwen, R., Klein, R., Mitchell, P., Vingerling, J.R., Klein, B.E., Smith, W., and De Jong, P.T. (2004). Risk factors for incident age-related macular degeneration: pooled findings from 3 continents. Ophthalmology *111*, 1280-1287.

Toomey, C.B., Kelly, U., Saban, D.R., and Bowes Rickman, C. (2015). Regulation of age-related macular degeneration-like pathology by complement factor H. Proceedings of the National Academy of Sciences of the United States of America *112*, E3040-3049.

Umetani, M., Ghosh, P., Ishikawa, T., Umetani, J., Ahmed, M., Mineo, C., and Shaul, P.W. (2014). The cholesterol metabolite 27-hydroxycholesterol promotes atherosclerosis via proinflammatory processes mediated by estrogen receptor alpha. Cell metabolism *20*, 172-182.

153

Umino, Y., Solessio, E., and Barlow, R.B. (2008). Speed, spatial, and temporal tuning of rod and cone vision in mouse. The Journal of neuroscience : the official journal of the Society for Neuroscience *28*, 189-198.

van Leeuwen, R., Klaver, C.C., Vingerling, J.R., Hofman, A., and de Jong, P.T. (2003). Epidemiology of age-related maculopathy: a review. European journal of epidemiology *18*, 845-854.

Vats, D., Mukundan, L., Odegaard, J.I., Zhang, L., Smith, K.L., Morel, C.R., Wagner, R.A., Greaves, D.R., Murray, P.J., and Chawla, A. (2006). Oxidative metabolism and PGC-1beta attenuate macrophage-mediated inflammation. Cell metabolism *4*, 13-24.

Vavvas, D.G., Daniels, A.B., Kapsala, Z.G., Goldfarb, J.W., Ganotakis, E., Loewenstein, J.I., Young, L.H., Gragoudas, E.S., Eliott, D., Kim, I.K.*, et al.* (2016). Regression of Some High-risk Features of Age-related Macular Degeneration (AMD) in Patients Receiving Intensive Statin Treatment. EBioMedicine *5*, 198-203.

Vlachos, I.S., Paraskevopoulou, M.D., Karagkouni, D., Georgakilas, G., Vergoulis, T., Kanellos, I., Anastasopoulos, I.L., Maniou, S., Karathanou, K., Kalfakakou, D.*, et al.* (2015). DIANA-TarBase v7.0: indexing more than half a million experimentally supported miRNA:mRNA interactions. Nucleic acids research *43*, D153-159.

Waldron, P.V., Di Marco, F., Kruczek, K., Ribeiro, J., Graca, A.B., Hippert, C., Aghaizu, N.D., Kalargyrou, A.A., Barber, A.C., Grimaldi, G.*, et al.* (2018). Transplanted Donor- or Stem Cell-Derived Cone Photoreceptors Can Both Integrate and Undergo Material Transfer in an Environment-Dependent Manner. Stem cell reports *10*, 406-421.

Wei, X., Song, H., Yin, L., Rizzo, M.G., Sidhu, R., Covey, D.F., Ory, D.S., and Semenkovich, C.F. (2016). Fatty acid synthesis configures the plasma membrane for inflammation in diabetes. Nature *539*, 294-298.

Wenzel, A., Reme, C.E., Williams, T.P., Hafezi, F., and Grimm, C. (2001). The Rpe65 Leu450Met variation increases retinal resistance against light-induced degeneration by slowing rhodopsin regeneration. The Journal of neuroscience : the official journal of the Society for Neuroscience *21*, 53-58.

Williams, P.A., Harder, J.M., Foxworth, N.E., Cochran, K.E., Philip, V.M., Porciatti, V., Smithies, O., and John, S.W. (2017). Vitamin B3 modulates mitochondrial vulnerability and prevents glaucoma in aged mice. Science (New York, NY) *355*, 756-760.

Wong, C.K., Smith, C.A., Sakamoto, K., Kaminski, N., Koff, J.L., and Goldstein, D.R. (2017). Aging Impairs Alveolar Macrophage Phagocytosis and Increases Influenza-Induced Mortality in Mice. Journal of immunology (Baltimore, Md : 1950) *199*, 1060-1068.

Wong, F., and Kwok, S.Y. (2016). The Survival of Cone Photoreceptors in Retinitis Pigmentosa. JAMA ophthalmology, 1-2.

Wong, N., and Wang, X. (2015). miRDB: an online resource for microRNA target prediction and functional annotations. Nucleic acids research *43*, D146-152.

Wong, W.L., Su, X., Li, X., Cheung, C.M., Klein, R., Cheng, C.Y., and Wong, T.Y. (2014). Global prevalence of age-related macular degeneration and disease burden projection for 2020 and 2040: a systematic review and meta-analysis. The Lancet Global health *2*, e106-116.

Wright, A.F., Chakarova, C.F., Abd El-Aziz, M.M., and Bhattacharya, S.S. (2010). Photoreceptor degeneration: genetic and mechanistic dissection of a complex trait. Nature reviews Genetics *11*, 273-284.

Wu, W.H., Tsai, Y.T., Justus, S., Lee, T.T., Zhang, L., Lin, C.S., Bassuk, A.G., Mahajan, V.B., and Tsang, S.H. (2016). CRISPR Repair Reveals Causative Mutation in a Preclinical Model of Retinitis Pigmentosa. Molecular therapy : the journal of the American Society of Gene Therapy *24*, 1388-1394.

Xia, J., Sinelnikov, I.V., Han, B., and Wishart, D.S. (2015). MetaboAnalyst 3.0--making metabolomics more meaningful. Nucleic acids research *43*, W251-257.

Xiao, C., Calado, D.P., Galler, G., Thai, T.H., Patterson, H.C., Wang, J., Rajewsky, N., Bender, T.P., and Rajewsky, K. (2007). MiR-150 controls B cell differentiation by targeting the transcription factor c-Myb. Cell *131*, 146-159.

Yang, H., Yang, T., Baur, J.A., Perez, E., Matsui, T., Carmona, J.J., Lamming, D.W., Souza-Pinto, N.C., Bohr, V.A., Rosenzweig, A.*, et al.* (2007). Nutrient-sensitive mitochondrial NAD+ levels dictate cell survival. Cell *130*, 1095-1107.

Yau, K.W., and Hardie, R.C. (2009). Phototransduction motifs and variations. Cell *139*, 246-264.

Ying, W. (2006). NAD+ and NADH in cellular functions and cell death. Frontiers in bioscience : a journal and virtual library *11*, 3129-3148.

Yip, J.L., Khawaja, A.P., Chan, M.P., Broadway, D.C., Peto, T., Tufail, A., Luben, R., Hayat, S., Bhaniani, A., Wareham, N.J.*, et al.* (2015). Cross Sectional and Longitudinal Associations

between Cardiovascular Risk Factors and Age Related Macular Degeneration in the EPIC-Norfolk Eye Study. PloS one *10*, e0132565.

Yoon, M.J., Yoshida, M., Johnson, S., Takikawa, A., Usui, I., Tobe, K., Nakagawa, T., Yoshino, J., and Imai, S. (2015). SIRT1-Mediated eNAMPT Secretion from Adipose Tissue Regulates Hypothalamic NAD+ and Function in Mice. Cell metabolism *21*, 706-717.

Yoshino, J., Baur, J.A., and Imai, S.I. (2018). NAD(+) Intermediates: The Biology and Therapeutic Potential of NMN and NR. Cell metabolism *27*, 513-528.

Yoshino, J., and Imai, S. (2013). Accurate measurement of nicotinamide adenine dinucleotide (NAD(+)) with high-performance liquid chromatography. Methods Mol Biol *1077*, 203-215.

Yoshino, J., Mills, K.F., Yoon, M.J., and Imai, S. (2011). Nicotinamide mononucleotide, a key NAD(+) intermediate, treats the pathophysiology of diet- and age-induced diabetes in mice. Cell metabolism *14*, 528-536.

Yu, J., Sadhukhan, S., Noriega, L.G., Moullan, N., He, B., Weiss, R.S., Lin, H., Schoonjans, K., and Auwerx, J. (2013). Metabolic characterization of a Sirt5 deficient mouse model. Scientific reports *3*, 2806.

Zhang, Y., Bharathi, S.S., Rardin, M.J., Uppala, R., Verdin, E., Gibson, B.W., and Goetzman, E.S. (2015). SIRT3 and SIRT5 regulate the enzyme activity and cardiolipin binding of very long-chain acyl-CoA dehydrogenase. PLoS One *10*, e0122297.

Zhou, M., Ottenberg, G., Sferrazza, G.F., Hubbs, C., Fallahi, M., Rumbaugh, G., Brantley, A.F., and Lasmezas, C.I. (2015). Neuronal death induced by misfolded prion protein is due to NAD+ depletion and can be relieved in vitro and in vivo by NAD+ replenishment. Brain : a journal of neurology *138*, 992-1008.

Zindy, F., Quelle, D.E., Roussel, M.F., and Sherr, C.J. (1997). Expression of the p16INK4a tumor suppressor versus other INK4 family members during mouse development and aging. Oncogene *15*, 203-211.

Zinkernagel, M.S., Schorno, P., Ebneter, A., and Wolf, S. (2015). Scleral thinning after repeated intravitreal injections of antivascular endothelial growth factor agents in the same quadrant. Investigative ophthalmology & visual science *56*, 1894-1900.